The Independent Steering and Driving Vehicle: Design, Energy Efficiency and Parking Analysis

QIAN, Huihuan

A Thesis Submitted in Partial Fulfilment
of the Requirements for the Degree of
Doctor of Philosophy
in
Automation and Computer-Aided Engineering

The Chinese University of Hong Kong
September 2010

Thesis /Assessment Committee

Professor Ruxu Du (Chair)

Professor Yangsheng Xu (Thesis Supervisor)

Professor Changling Wang (Committee Member)

Professor Lilong Cai (External Examiner)

Abstract

Throughout the history of human civilization, vehicles have played a significant role by connecting people in various locations. They have thus boosted the progress of civilization and made our lives more convenient. However, as the number of vehicles on the road has increased, the convenience, which vehicles provide, has gradually turned into inconvenience in three respects: 1) the energy consumed by vehicles accounts for a large proportion of total energy consumption, which is in an ever-increasing trend; 2) more parking space is needed, a significant proportion of which is not for parking itself but for enabling the vehicle to be navigated to its final parking slot; 3) the effort required to park a car is also troublesome, causing the driver to spend much more time in a crowded parking lot.

To alleviate these three problems, I develop a methodology to design an independent steering and driving vehicle (ISDV). It brings together the robotic technologies of steer-by-wire, drive-by-wire, four-wheel-independent-steering, and four-wheel-independent-driving. All four wheels of the ISDV can be steered independently, so that vehicle rotation and translation can be decoupled from each other. Omni-directional motions such as zero radius turning (ZRT) and lateral parking (LP) are realized, thereby enhancing the agility of the vehicle. In contrast with omni-directional wheeled mobile robots, this vehicle is targeted at serving as a human carrier or even as a vehicle carrier in the future.

After describing the development of the ISDV, this thesis studies the energy management which can improve the energy efficiency. It is shown that the traditional electric vehicle (EV) is not capable of managing the energy required for one driving cycle because it has only a single traction motor. This thesis proposes and examines a new way to manage electrical energy in which torque is distributed among different in-wheel motors to achieve a higher level of overall energy efficiency, which has been enhanced and demonstrated in various driving cycles.

Thereafter, the thesis studies two aspects of benefits the ISDV can bring to parking. One is in space efficiency, defined as the ratio of the total space occupied by the vehicle in its final parked state over the whole area covered by the parking lot. Comparison of the ISDV and traditional vehicles in parking proves that the ISDV afford a higher level of space efficiency. The other aspect is the parking time. It is tested experimentally in the hardware-in-loop (HIL) system, and the motions of traditional vehicles, the zero radius turning motion, and the free motion of the ISDV are compared. The less time for parking demonstrates the easiness to steer the ISDV.

論文摘要

在人類文明的發展進程中，車輛發揮了極其重要的作用。它將不同地域的人聯結起來，使得文明得以傳播，並使我們的生活日益方便。然而，隨著近來車輛數目與日俱增，這種方便與優勢正慢慢地趨於其反面，主要呈現在三個方面。1)俱增的車輛在消耗著大量的能源，這種增加趨勢從未停止。2)從空間來看，日益增加的車輛需要佔據大量的停靠空間，該情況在擁擠的城市環境中尤其嚴重。3)要將車輛順利停入對很多司機來說仍是一件非常具有挑戰的任務。許多司機將很多時間花在擁擠環境中的泊車。

在本文中，我將線控轉向、線控驅動、四輪獨立轉向、四輪獨立驅動等多項機器人技術集成入汽車，設計並研發了一代暫新的獨立轉向驅動汽車（ISDV）。獨立轉向的四個輪組能夠使得車體的旋轉和平移相互解耦。全方位模式的實現，如零半徑轉彎、平行移動，極大地提高了車輛的靈活性。與一般的全方位移動機器人相比，該車輛是在載人、甚至載車的重載機器人方向的探索。

在能源方面，傳統的電動車輛只有一個驅動電機，因而無法對工況進行能量管理與分配。這種全方位轉向車輛是通過四個獨立的輪轂電機進行驅動。利用這種四輪獨立驅動的結構，本論文對於這種新穎的能量管理方式進行了研究，提出了通過優化力矩分配的方式來提高能量的利用效率，並在多種工況中加以驗證。

此后，論文從空間與時間兩個方面對ISDV在泊車中的改善進行了分

析。空間效率定義爲車體在停泊時占用的面積與停車場的總面積的比率。通過對ISDV和傳統前輪轉向車輛的比較，得出ISDV具有更高空間效率的結論。在泊車時間方面，通過硬件再環仿真的方法，對前輪轉向、原地轉向、自由模式進行了比較，ISDV具有更短的泊車時間，因而更易操作。

Acknowledgement

I would like to take this opportunity to show my most sincere gratitude to many special people. It was only with their support that this thesis was made possible.

First, I would like to thank my supervisor, Prof. Yangsheng Xu, for his constant supervision and advice throughout the six years of my academic life in Hong Kong. He has provided me with an excellent opportunity to receive academic training and has helped me to learn research skills and methodology efficiently. Under his instruction, my ability to make insights, my presentation skills, and my other related skills have been improved.

I would also like to thank the members of my thesis committee - Prof. Ruxu Du, Prof. Charlie Wang, and Prof. Lilong Cai - for taking the time to evaluate my thesis. Prof. Du and Prof. Wang have provided me with much constructive advice during my oral qualifying examinations and yearly presentations. I am also grateful to Prof. Cai for the effort he has made to back me up.

I would like to thank Dr. Yongsheng Ou and Dr. Xinyu Wu, with whom I worked together to gain initial research experience; Dr. Xi Shi and Dr. Bufu Huang, from whom I have learnt much about software and hardware design and development; Dr. Zhancheng Wang, Dr. Weimin Li, Mr. Tin Lun Lam, Mr. Chenggang Xia, and Mr. Tiande Mo, with whose assistance I came to realize the omnidirectional vehicle; Dr. Weizhong Ye, Dr. Zhi Zhong, Dr. Zhijiang Zhao, Mr. Jingyu Yan, Mr. Kai Wing Hou, Mr. Yongquan Chen, Mr. Ning Ding, Mr. Xin Shi, Mr. Wing Kwong Chung, Mr. Maxwell Chow, Mr. Hoi Wut Yip, Mr. Yun Tung Wong, Mr. Yin Fan Huen, and Ms. Meng Chen for their support in various projects; Mr. Tong, Allan, Philip, Karina, Thomas, and Ms. Chan for their technical support; and Edith, Ms. Kan, Maggie, Joyce, and Winnie for their support in much of my other work. I have also received a great deal of assistance from many other people who have helped me indirectly in my research.

Finally, with the greatest love and respect, I acknowledge the long-term and everlasting support, love, and encouragement of my family - my parents, my parents-in-law, my wife, and my son. I especially thank my wife Kathy, whose strong support, love, and concern have enabled me to focus on my thesis in this key period. These are the constant sources of inspiration in my research and will continue to be so over the course of my future career.

Contents

4 Parking Analysis of the Independent Steering and Driving Vehicle 75

List of Figures

List of Tables

Chapter 1

Introduction

1.1 Motivation

Throughout the history of human civilization, the need to connect with others has been the major driving force behind the invention of vehicles and subsequent innovations. The progress made in this field of human endeavor has boosted human civilization by connecting people in different nations of the world and making our lives more convenient.

Nevertheless, the tremendous increase in the number of vehicles on the road in recent years has gradually resulted in some of the convenience vehicles provide being lost due to the large amount of resources they consume.

Energy:

An external source of energy is required to drive a vehicle. Animal-driven energy sources are now outdated due to their low levels of power and continuity and the short distances over which they are effective. Non-renewable sources of energy such as petrol and natural gas have been the main resources powering vehicles for more than a century now.

People have recently realized the danger of the excessive exploitation of such energy resources due to the tremendous increase in the number of vehicles, and have launched a global renewable energy campaign in which electrical energy plays the main role. However, one question that remains unanswered is how efficiently electricity is utilized.

Space:

Every vehicle occupies a physical space. Although little attention is paid to this fact when a vehicle is driven due to the low level of road traffic density, it becomes troublesome when a large number of vehicles are concentrated in a single area-such as a car park-where people need to leave their vehicle to engage in other activities. Crowded car parks not only have to provide space for vehicle docking, but must give vehicles the room they require to move through them.

Figure 1.1 shows a very crowded car park. The demand for spatial resources will rise significantly as the demand for vehicles increases during the globalization process.

All other means of transport such as ships, airplanes, or even lunar vehicles in the future need space when not in use. Constructing spaces such as ferry berths, aircraft hangars, or even space stations is expensive and consumes resources. Such spaces will be more cost-effective if they are minimized.

Time:

An important factor to consider other than spatial resources is time. In

Figure 1.1: Crowded car park

the urban driving environment, much time is actually spent searching for a vacant parking slot near the driver's destination. Moreover, when the target parking slot is identified, time and effort are also consumed in parking the vehicle safely. The situation is similar when one retrieves a vehicle from a crowded parking structure. Apparently, the time will be substantially longer to retrieve on vehicle in Figure 1.1.

In the parking scenario, space and time are a pair of conflicting variables that will reach a point of balance. That is to say, when the efficiency of space decreases, i.e. when more space is taken up by a parked vehicle, the time required to park the car will fall and time efficiency will rise, and vice versa.

In this thesis, I propose, design and develop an independent steering and driving vehicle (ISDV) to alleviate the three aforementioned problems. The robotic technologies of four-wheel independent steering, four-wheel independent driving, steer by wire, and drive by wire are incorporated into a vehicle to realize omni-directional motions. The thesis shows that energy efficiency can be improved. Moreover, the parking can be easier, because the space efficiency can be increased and parking time can be reduced.

1.2 Related Work

1.2.1 Vehicle Structure

Ever since the birth of the first modern automobile in 1885 (as shown in Figure 1.2), the configuration of the vehicle steering mechanism has remained almost unchanged[1]. The configuration employed in early vehicles was similar to that used in the four-wheel automobiles developed thereafter, as illustrated in Figure 1.3. The translation of the vehicle's center is highly dependent on rotation of the vehicle attitude, and vice versa. Hence, it is difficult to achieve omnidirectional motion, which refers to the ability of the vehicle to translate in an arbitrary direction while the vehicle is oriented in another arbitrary direction.

One of important obstacles to overcome in making a vehicle omnidirectional is the difficulty of decoupling rotation from translation. Doing so successfully involves realizing their mutual independence by eliminating both the side effect of translation when the vehicle is in rotation and the side effect of rotation when the vehicle is in translation in an arbitrary direction.

A minimal turning radius is regarded as an important parameter of omnidirectionality because the smaller it is, the smaller the side effect of transla-

---

[1] Although the first vehicle had three wheels, the two rear wheels were conventional fixed wheels and the front wheel was a conventional center-oriented wheel

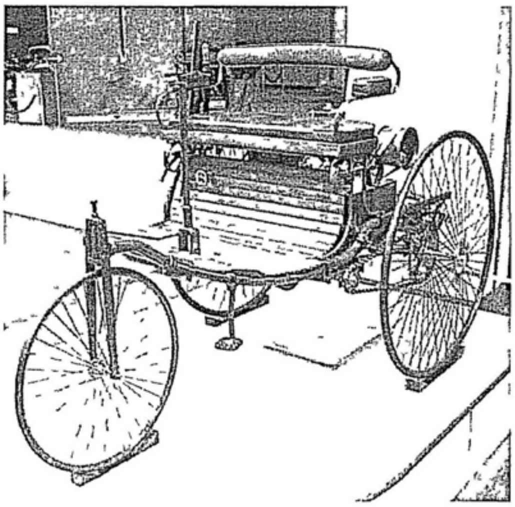

Figure 1.2: First automotive invented by Karl Benz in 1885

tion on steering manipulation. The ideal turning radius is 0, in which case translation will not occur while steering. However, the steering angles of the front wheels of a traditional vehicle are confined to an arc from about -35 degrees to +35 degrees [4] due to the existence of the steering tie rod. This rod represents an obstacle to expansion of the turning radius. As a result, it is necessary to steer the vehicle in a large semi-circle to turn the vehicle in the opposite direction.

Participants in the vehicle industry have endeavored to enhance the steerability of vehicles by means of four-wheel steering (4WS) systems that reduce the turning radius. The first 4WS vehicle appeared in 1938 and was manufactured by Mercedes-Benz. Its rear wheels were steered in the opposite direction to the front wheels to shorten the turning radius. Honda started manufacturing the Prelude 4WS vehicle in 1987. Its distinguishing feature was that the steering angle of the rear wheels depended on that of the front wheels. When the steering wheel was turned slightly, the rear wheels were

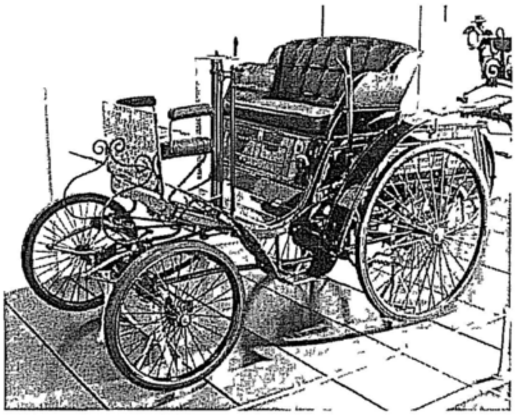

Figure 1.3: Karl Benz's "Velo" model (1894)

steered in the same direction as the front wheels to improve stability during a high-speed turn or when changing lane. When the steering wheel was turned at a large angle, the rear wheels were steered in the opposite direction to the front wheels to shorten the turning radius. However, the existence of a steering tie rod continued to block any further steerability enhancement; moreover, coupling of the front wheels and rear wheels meant they were not independent of each other, which would have allowed for better steerability.

One of the most recent developments in the vehicle industry is the release of the Jeep Hurricane designed by the Chrysler Group. It is capable of zero radius turning (ZRT) by steering the four wheels until their rotational axes point to the center of the vehicle. Its design incorporates four-wheel drive (4WD) to realize ZRT. However, the power origins of the four wheels are coupled into two engines. As a result, a complicated device must be used to control the direction of each wheel because the four wheels have to be driven in different directions according to whether the vehicle is in traditional front-wheel steering (FWS) or ZRT mode. Mechanical complexity makes it impossible to integrate a greater range of omnidirectional motions into the system. Moreover, although the vehicle's steering system is independent of translation, it does not allow for translation in arbitrary directions.

In the field of robotics, there has been a significant volume of research on wheeled mobile robots (WMR). Although they are capable of omnidirectional motions [6] [7] [8] [9] [10], they have not been developed as human carriers.

In research on intelligent omnidirectional hybrid electric vehicles (IO-HEV) at the Chinese University of Hong Kong, unlike the engine driving principle used in traditional vehicles, the engine is disconnected from the transmission and is instead connected to a generator that charges a battery package. The whole transmission is replaced by four in-wheel motors powered by the battery package to create propelling force. This drive-by-wire technology therefore significantly reduces the complexity associated with mechanical differentials such as the one seen in the Hurricane. The steering tie rod is also replaced by four sets of novel steering mechanisms enabling each wheel to be steered independently in the -35 to +90 degree range, which is large enough not only for ZRT, but also for lateral parking (LP) in which translation is independent of steering. The vehicle's innovative wheel configuration also alleviates the problem of parking.

1.2.2 Car-like Mobile Robot Motion

To enhance space and time efficiency, researchers in robotics have devoted much effort to motion planning for automatic navigation.

Dubins [50] was the first to address the problem of finding the shortest path between two car-like robot configurations without considering obstacles.

He provided a sufficient set of optimal paths for a robot moving forward only. Thereafter, Reeds and Shepps [1] showed that a family (RS family) of 48 different paths contains all the path segments required to realize a point-to-point path. They extended the number of directions in which the robot moves to two: forward and backward.

Moutarlier [46] defined the shortest feasible path (SFP) from a car-like robot to an object manifold in the configuration space. Mirtich [47] numerically computed the skeleton-a set of points that are maximally clear from the obstacles-that functions as the reference point for path planning. Souères [48] provided geometric reasoning for selecting optimal paths in the RS family. Giordano [49] used optimal control theory to develop an analytic solution for finding the shortest path to a manifold.

All of these recent studies have focused on the problem of how to select an optimal trajectory to navigate a car-like robot within a given scenario with obstacles. This thesis adopts an alternative perspective in attempting to show how to set the parking slot dimensions in a scenario in which the obstacles are parked vehicles to increase both parking capacity and space efficiency.

1.3 Thesis Overview

This thesis describes the design and development of an independent steering and driving vehicle (ISDV) that can act as a human carrier and incorporates the omnidirectional structure of a robot. This structure offers a new direction to improve the energy management in the electric vehicle. It will also improve the performance in parking in the aspects of space and time. The remainder of this thesis is arranged as follows.

Chapter 2 elaborates on the design of the ISDV. The technologies of steer-by-wire, drive-by-wire, four-wheel-independent-steering (4WIS), and four-wheel-independent-driving (4WID) are integrated into the vehicle structure to realize omnidirectional motion. The chapter also addresses the control system and software developed to coordinate the eight steer-drive actuators. Two human-vehicle steering interfaces are designed and developed to utilize the omni-directionality by means of discrete mode switching and continuous ICR allocation.

Chapter 3 shows that the new vehicle with its four-wheel independent driving structure can take advantage of the redundancy of its driving motors to manage the power (torque) among them and attain the maximum overall level of energy efficiency of the driving system. Different driving cycles are tested to support this optimal torque distribution methodology.

Chapter 4 analyzes the improvement that the omni-directionality can bring to parking. I model the contours of front-wheel steering vehicles in vertical parking scenarios, and develop a numeric method to compute the highest space efficiency in front-wheel-steering vehicles. The space efficiency of the ISDV is also analyzed. In the aspect of time analysis, human-in-loop experiment is designed to test the better performance of the ISDV.

Chapter 5 outlines the contributions this thesis makes.

Chapter 2

Design and Development of the Independent Steering and Driving Vehicle

2.1 Introduction

The structure of the automobile is inherited from the horse drawn carriage invented by German carriage builder Lankensperger in 1817 and patented in England by his agent Rudolph Ackermann in 1818.

The so-called Ackerman steering geometry shown in Figure 2.1, basically guarantees that the four wheels of the vehicle roll smoothly. The fundamental principle underlying Ackerman steering geometry is the geometric rule that all the axes of the four wheels should either point to the same point called

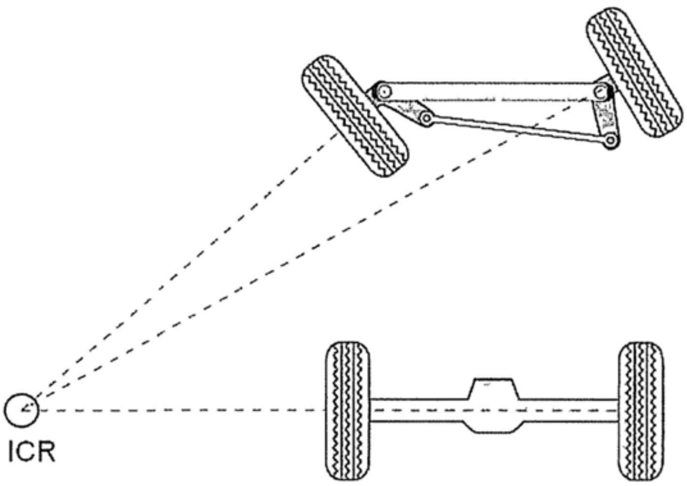

Figure 2.1: Ackerman steering geometry

the instantaneous center of rotation (ICR) or be completely parallel to each other (i.e. none of them intercept any of the others).

Ever since the invention of the automobile, all vehicles have inherited this steering structure in which the two front wheels are coupled by one steering rod, as shown in Figure 2.2 below. The steering action is delivered from the steering wheel (1) through the steering tie rod (2), the steering knuckle (3), and the steering knuckle arm (4), before finally reaching the front wheel (6).

In most cases, especially where the vehicle is driven at high speed, front-wheel steering is adequate for manipulating the vehicle's direction. A single-track model has been developed to facilitate the kinematic and dynamic analysis of vehicles [5]. In traditional vehicles, the two front wheels are steered as a coupled pair, and the two rear wheels are either parallel to each other or are also steered as a couple in a 4WS vehicle. As a result, a single-track model can simplify the four-wheel vehicle model such that the two front

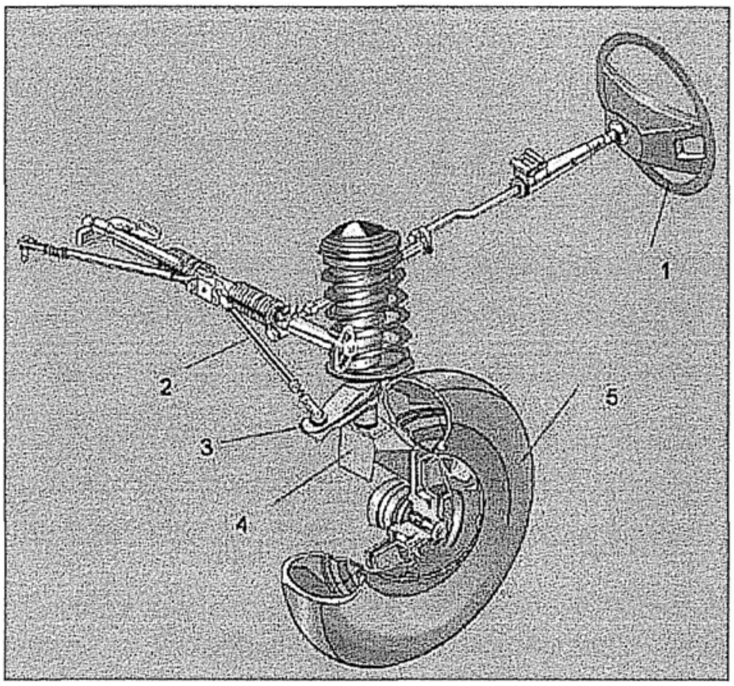

Figure 2.2: Steering mechanism in a traditional vehicle

wheels and the two rear wheels are combined into one virtual front wheel and one virtual rear wheel, respectively.

Most traditional vehicles adopt the single-track model combining the pairs of wheels at the front and rear of the car, respectively, into two virtual wheels, i.e. the front virtual wheel is in the center of the front axis and the rear virtual wheel is in the center of the rear axis.

The Figure 2.3 below illustrates the single-track model as shown by the two grey wheels. The vehicle configuration space is represented as a 4D vector, $(x_c, y_c, \theta, \phi)^T$, where (x_c, y_c) is the Cartesian coordinate of the center of the rear virtual wheel, θ is the angle from the vector $\overrightarrow{OX}$ to the central line of the vehicle $\overrightarrow{O_bX_b}$, and ϕ is the angle of the virtual front wheel. L and W are the vehicle body length and width, respectively. a and b are the front and rear overhang. c is the distance from the vehicle body to the center of the left or right wheel.

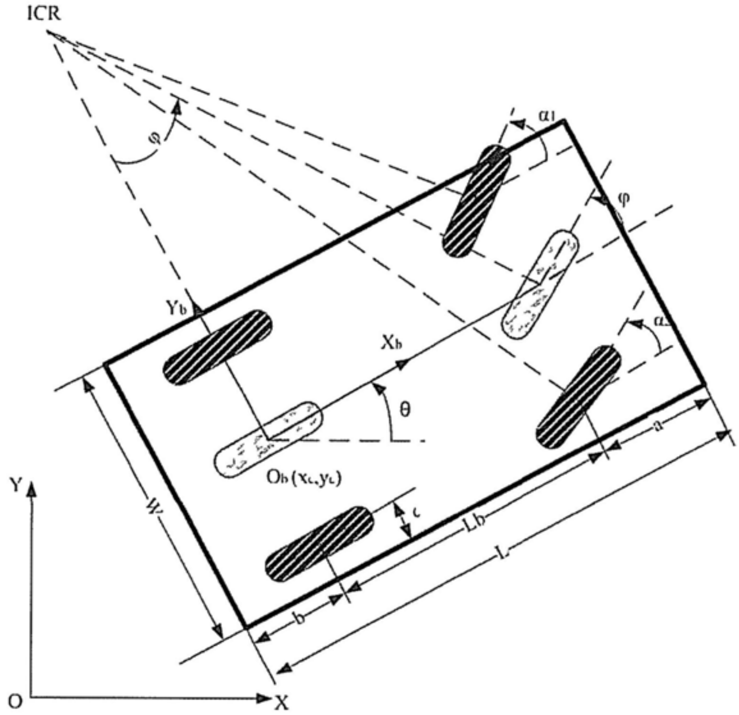

Figure 2.3: Single track model

The state space equation for the system is

$$\begin{bmatrix} \frac{dx_c}{dt} \\ \frac{dy_c}{dt} \\ \frac{d\theta}{dt} \\ \frac{d\phi}{dt} \end{bmatrix} = \begin{bmatrix} \cos(\theta) \\ \sin(\theta) \\ \frac{1}{L_b}\tan(\phi) \\ 0 \end{bmatrix} v(t) + \begin{bmatrix} 0 \\ 0 \\ 0 \\ 1 \end{bmatrix} \omega(t) \tag{2.1}$$

where L_b is the wheelbase, $v(t)$ is the speed at the center of the rear virtual wheel, and $\omega(t)$ is the angular velocity at which the virtual front wheel is turned.

In turning manipulation, to map the steering angle of the steering wheel into the two front wheels, Ackerman steering geometry can be approximated such that the angle of the inner front wheel is directly proportional to the angle of the steering wheel input, $\alpha_{innerfront} = K\phi_{steeringwheel}$. In traditional vehicles, due to the existence of mechanical components such as knuckle arms, a front wheel can be maximally steered to 35 degrees [4] and the steering wheel has a maximal turning range of 1080 degrees. Hence, the gain K can be identified by $K = \frac{35}{540}\phi_{steeringwheel}$.

The steering angle of the outer front wheel satisfies Ackerman steering geometry and thus $\alpha_{outerfront} = \arctan(\frac{L_b}{W-2c+L_b/\tan\phi})$, where W is the width of the vehicle body, and c is the distance from the center of wheel to the side edge of the vehicle body.

2.2 Modeling of the Independent Steering and Driving Vehicle

I now describe the design and implementation of the independent steering and driving vehicle (ISDV) at the Chinese University of Hong Kong. The ISDV departs from the traditional steering/driving mechanism and allows for omnidirectional motions such as zero-radius turning (ZRT) and lateral parking (LP).

2.2.1 Steering Modeling

The Ackerman steering geometry employed in traditional front-wheel steering vehicles prevents them from being more agile. However, when the vehicle is operated in a small and limited zone, there is a far greater need for steerability.

To realize a higher degree of steerability, Ackerman steering geometry is extended so the ICR can be localized at any position in the 2D plane.

Figure 2.4 shows the extended Ackerman steering geometry whereby the vehicle turns about an arbitrary ICR denoted as (x_{ICR_b}, y_{ICR_b}). OXY and $O_bX_bY_b$ are a global coordinate frame and a local coordinate frame fixed onto the vehicle, respectively. The configuration of the vehicle can be expressed by (x_v, y_v, θ). $(x_{ib}, y_{ib}), i = 1, 2, 3, 4$ are 2D coordinates of the centers of the 4 wheels in the local coordinate frame in the sequence left front, left rear, right rear, right front. The outer part of each wheel is shown in black to identify its direction, as explained in the next subsection. $\alpha_i, i = 1, 2, 3, 4$ are the steering angles from the original position. $\vec{v}_i, i = 1, 2, 3, 4$ are the velocity vectors in the global coordinate frame.

In this extended Ackerman steering geometry, all the axes of the wheels must intersect at the ICR to permit motion. Thus, the steering angles of the wheels are constrained by the following equations.

$$(\cos(\alpha_i), \sin(\alpha_i)) \cdot \left((x_{1_b}, y_{1_b})^T - (x_{ICR_b} y_{ICR_b})^T\right) = 0 \quad (i = 1, 2, 3, 4) \tag{2.2}$$

In the ISDV, two motions are important for enhanced steerability: zero

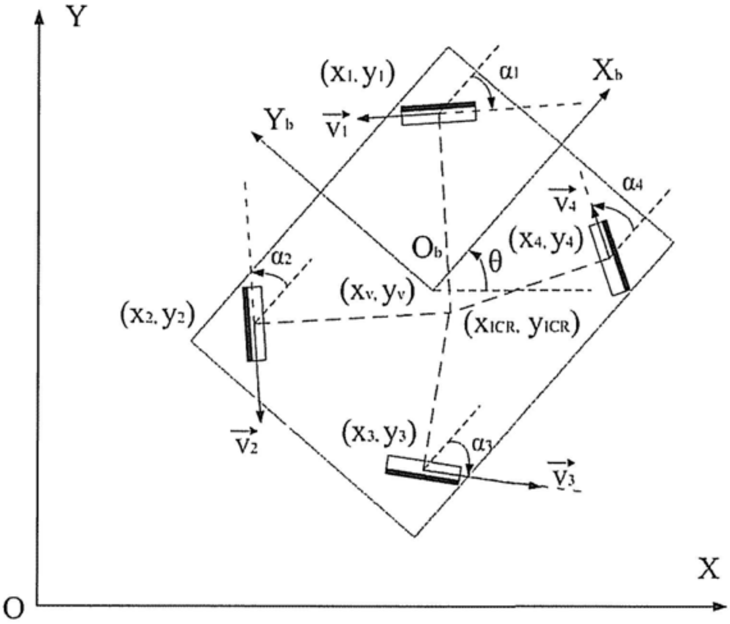

Figure 2.4: Kinematics of rotation about an arbitrary ICR

radius turning (ZRT) and lateral parking (LP). These are two special cases of the extended Ackerman steering geometry with an arbitrary ICR.

Zero Radius Turning (ZRT)

In traditional vehicles, the two front wheels are steered to change the attitude of the vehicle. A change in the position of the center is a side effect of rotation. However, in a narrow space, the driver does not want the vehicle to be subject to this side effect. The ideal solution is therefore to rotate the vehicle without translation, which can be realized by ZRT.

Figure 2.5 illustrates the kinematics of ZRT. The right front and left rear wheels are steered to the same positive angle $\alpha = \arctan(\frac{L_b}{W-2c})$ and the other two wheels are steered to the same negative angle $-\alpha$.

In the ZRT mode, all the wheel speeds are numerically the same.

Lateral Parking (LP)

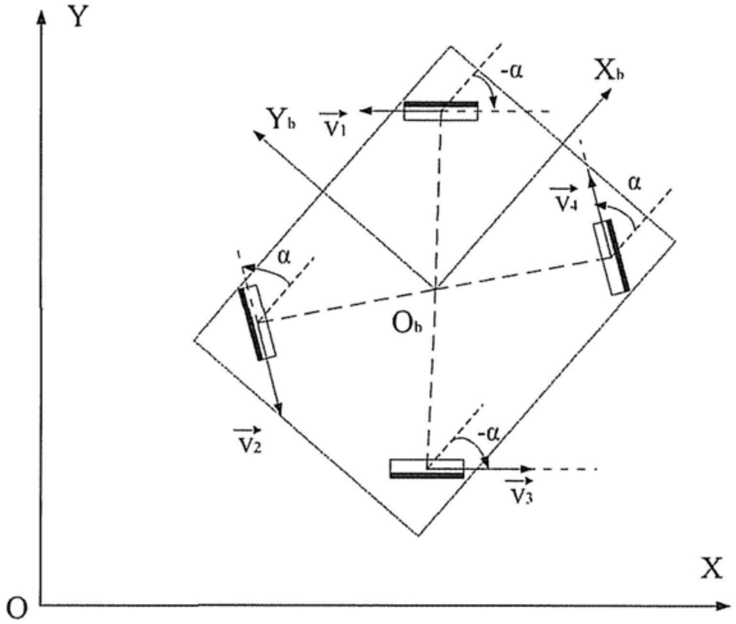

Figure 2.5: Kinematics of zero radius turning

Apart from rotation, lateral translation can also be exerted directly and independently. For pure translation, i.e., motion without a change in attitude, all four wheels ought to be steered to an identical angle. This can be represented by way of extended Ackerman geometry whereby the ICR intersects at an infinite point. In LP, the ICR is placed at the infinite point in the front or rear direction.

To simplify manipulation of the vehicle, LP is the most important function because the parking slot is parallel to and only 1 or 2 meters from the current vehicle position in most parking scenarios.

Figure 2.6 shows the kinematical constraints of the LP mode.

The left front and right rear wheels are steered to -90 degrees and the other two wheels are steered to +90 degrees. The four velocity vectors are parallel to each other and have the same length under the skid-free assumption.

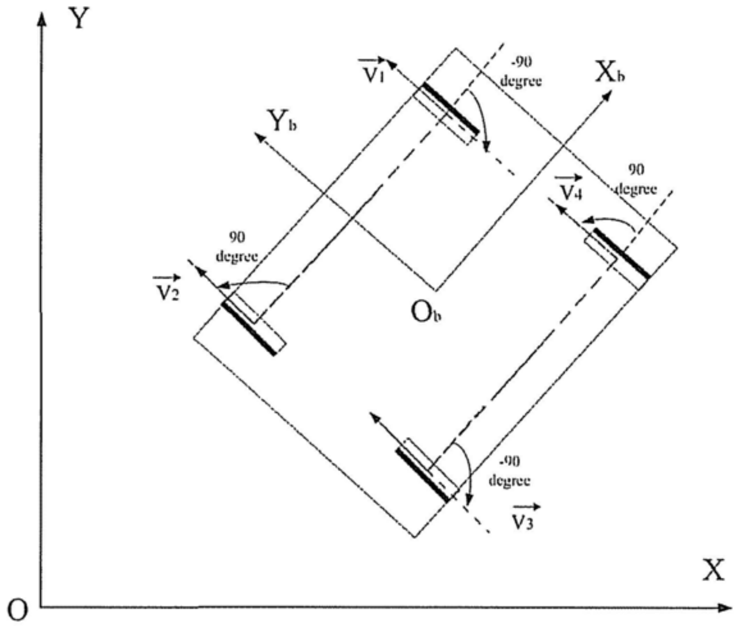

Figure 2.6: Kinematics of lateral parking

2.2.2 Driving Modeling

In traditional front-wheel steering vehicles, the engine output shaft is the input of the transmission, which transfers torque to the two driving wheels through the differential. When all the wheels become steerable over a large range, the traditional engine driving mode will lead to a complex mechanism and a low level of power efficiency. I thus designed the ISDV using in-wheel motors for driving.

To select appropriate in-wheel motors, I first considered the power demand of the vehicle. The following prior assumptions were made on the parameters of the vehicle. Let the maximum speed of the vehicle $v_{max} = 30km/h \doteq 8.4m/s$. The radius of the wheel is $r = 0.15m$. Maximum friction and dragging force is $f_{max} = \mu_f mg + \frac{1}{2}C_D A\rho v_{max}^2 \doteq 147Nm$, where

$\mu_f = 0.018$ (rotational friction coefficient)

$m = 600kg$ (total mass of the vehicle)

$g = 10m/s^2$ (gravitational acceleration)

$C_D = 0.3$ (constant between 0.25 and 0.4)

$A = 3m^2$ (wind contact area)

$\rho = 1.2258Ns^2m^{-4}$ (wind friction constant)

$v_{max} = 8.4m/s$ (maximum speed).

The maximum total power demand for driving is $P_{totalmax} = f_{max}v_{max} = 147 \times 8.4 \doteq 1300W = 1.3kW$. The maximum power required for each wheel is therefore about 325 watts. Six hundred watt in-wheel motors for electric motorcycles can thus be selected as the driving motors.

2.3 Chassis System

One novel feature of the design of the ISDV in comparison with that of traditional vehicles lies in the drive-by-wire and steer-by-wire chassis system employed. To achieve omnidirectional motion functionality, it is necessary for the system to include four-wheel independent driving (4WID) and 4-wheel independent steering (4WIS) capabilities.

The omnidirectional chassis consists of four independent steering-driving mechanisms and a chassis frame, as illustrated in Figure 2.7.

In the steering operation, a group of components including an in-wheel motor, its outer frame, a brake disk, a brake fork, an upper arm, a lower arm, and two dampers for suspension is steered about the rotational shaft, which is driven in the upper end by the output shaft of the speed-reduction

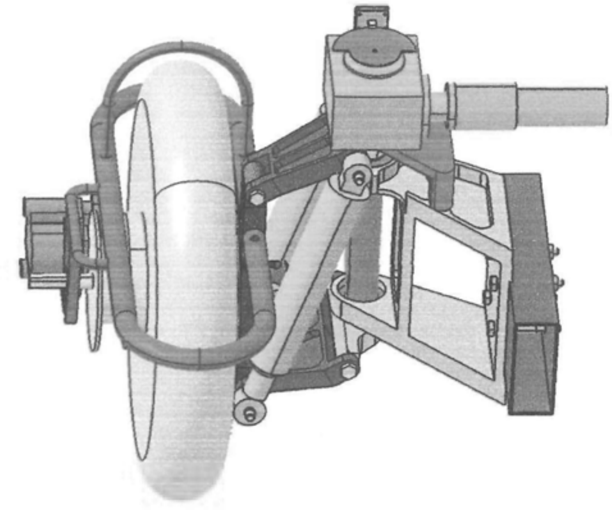

(a) Steering mechanism

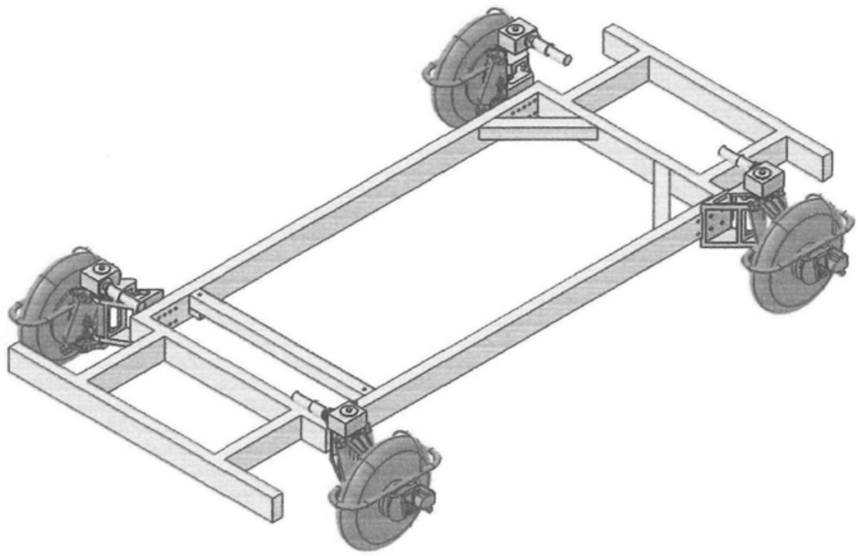

(b) Chassis frame

Figure 2.7: Chassis and steering mechanism

gearbox. The gearbox input is a Maxon granite brush DC motor. The in-wheel motor used for driving is a brushless DC motor originally used for electric motorcycles that is controlled by a voltage signal from the accelerator pedal. As the ISDV is a platform for an on-road vehicle, a suspension system is retained to absorb vertical shock.

There are four such independent steering mechanisms, one for each driving wheel.

The chassis frame is made of stainless steel and is supported by the four independent steering mechanisms.

The figure below illustrates the 4WIS-4WID structure. The steering motor 11 is mounted onto the worm gear box 10 using screws. The gear box 10 is connected to the rotational shaft 90 by a key so that the output shaft of the gear box and the rotational shaft are concentric. The upper end of the damper 70, the upper end of the rotational shaft 90, and the right end of the upper bar 50 are connected by a screw. The lower end of the rotational shaft 90 and the right end of the lower bar are also connected by a screw. The rotational shaft and the vehicle body 12 are mounted using bearings, with 90 being allowed to rotate in the body of the vehicle. The left end of the upper bar 50 and the left end of the lower bar 60 are connected to the frame 99 by screws. The brake 31 is screwed onto the frame 99 and the frame is mounted onto the axis of the motor 40 using nuts to allow for the rotation of 40 and to prevent 40 from moving along the direction of its axis. The brake disk is screwed onto the rotational part of the motor 40. The wheel 111 supports the vehicle and the motor 40 drives the vehicle. The brakes 30 and 31 reduce the velocity of the vehicle. The frame 99 prevents the wheel

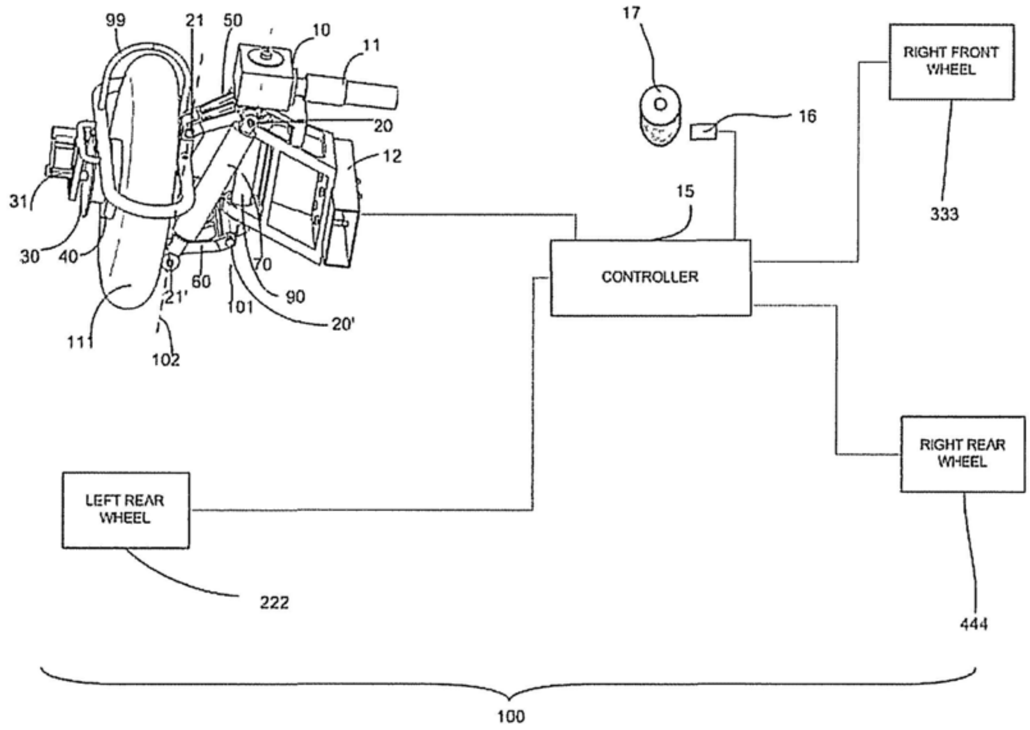

Figure 2.8: 4WIS-4WID mechanism

111 from moving in the direction of its axis. The steering motor 11 steers the rotational shaft as the speed is reduced by 10. The rotation of the shaft 90 is then transmitted to the frame 99 through the upper and lower bars 50 and 60. The dampers 70 absorb shock from the wheels 111.

Due to the existence of the braking components, the in-wheel motor for an electric motorcycle is not symmetric with respect to the central circular plane. Due to space limitations, Figure 2.3 shows all faces of the motor with braking components pointing toward the outside of the vehicle. Hence, the direction of each in-wheel motor should also be considered in determining the direction of motor velocity in Figure 2.4.

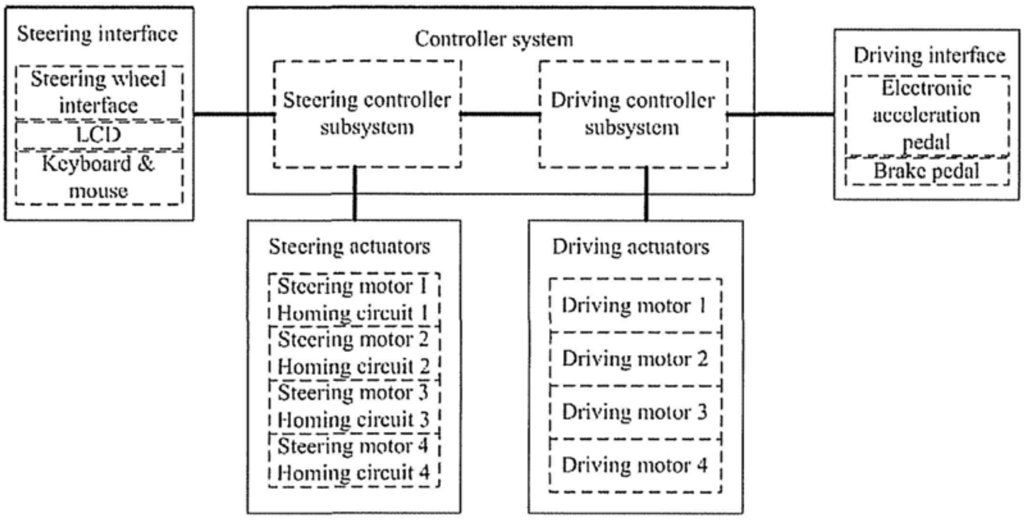

Figure 2.9: Controller system

2.4 Control System

Figure 2.9 outlines the control system of the ISDV. The system comprises five parts: the controller system, the steering interface, the driving interface, the steering actuators, and the driving actuators.

The controller system consists of two subsystems, one for steering control and the other for driving control. They are interconnected to allow them to communicate with each other.

Inside the steering interface there is a Logitec Momo racing steering wheel with a shift bar and six buttons for direction and mode selection. An LCD, a keyboard, and a mouse are also included for debugging and testing.

The driving interface is composed of two pedals, one an electronic acceleration pedal and the other a brake pedal for the hydraulic brake system.

The steering actuators include four Maxon granite brush DC motors with an encoder for relative position. The driving actuators consist of four driving

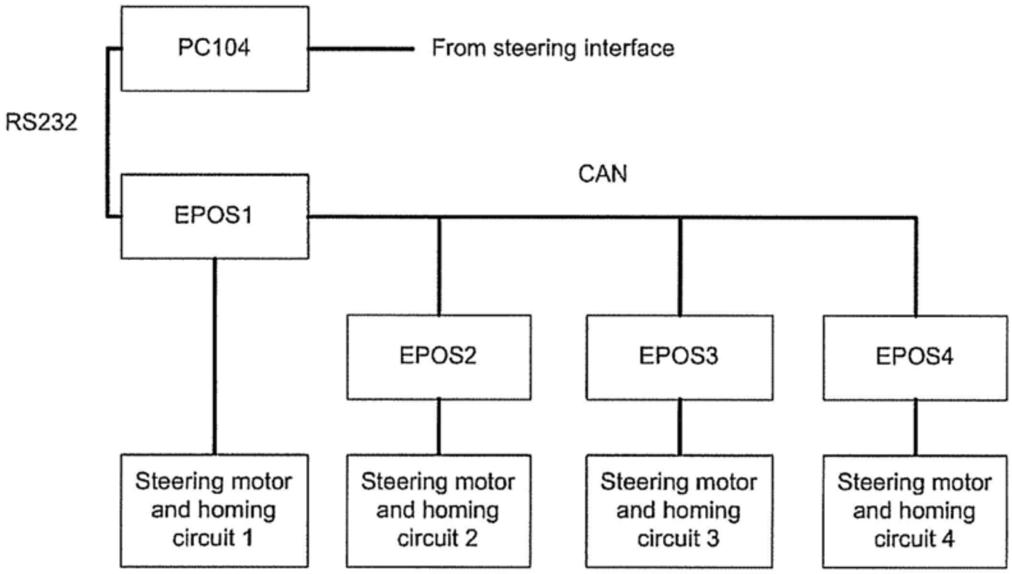

Figure 2.10: Steering controller subsystem

motors, all of which are brushless DC in-wheel motors.

2.4.1 Steering Control Subsystem

The steering controller subsystem is illustrated in Figure 2.10. A PC104 (PCM3380, Figure 2.11) with an onboard Intel Pentium M 1.1GHz, 1 GB DDR RAM and a 1 GB CF card as a hard disk acts as the kernel controller in the steering controller subsystem. Linux DSL 2.4 is adopted as the operating system for the PC104 because steering wheel data can be conveniently obtained from the USB port through the shell function.

In terms of input, the steering wheel provides data on steering angles, shift bar status, and button status. However, they are processed in different ways. As the steering angle is only needed to calculate the target position of each steering motor, it is processed by the PC104; because the shift bar message is related to the directions of the driving motors, it is transmitted to

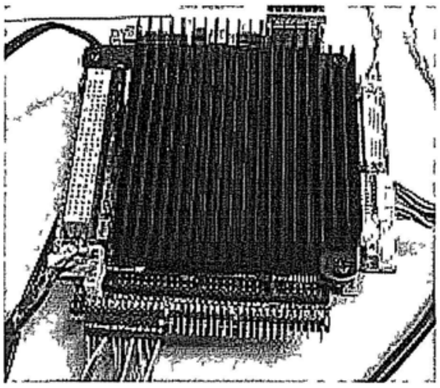

Figure 2.11: Outlook of the PC104

the digital signal processor (DSP); because the mode information is shared by the two subsystems, the PC104 reacts to this input and transmits it to the DSP as well.

In terms of output, the PC104 sends commands directly to the steering motor controllers and each command is given an ID. Maxon EPOS is a power controller for position control of the steering motor. It is equipped with either a CAN bus or RS232 for communication. The ISDV utilizes the configuration of the RS232-CAN gate connection. That is, EPOS1 functions as the gate and receives all commands from the PC104 via the RS232 port; thereafter, it executes the command with ID1 and transmits the other commands to the CAN bus.

2.4.2 Driving Control Subsystem

The driving control subsystem (Figure 2.12) includes a DSP (TMS320F2812, Figure 2.13) that serves as the kernel controller and four modified brushless DC motor controllers normally used for electric motorcycles.

The DSP obtains the voltage signal from the electronic acceleration pedal

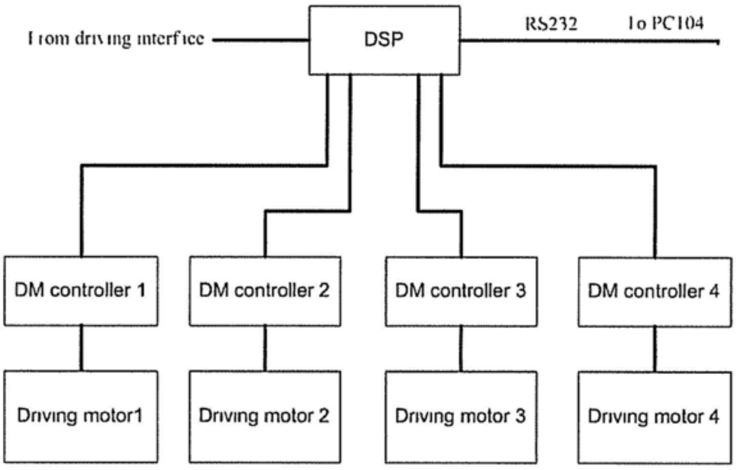

Figure 2.12· Driving controller subsystem

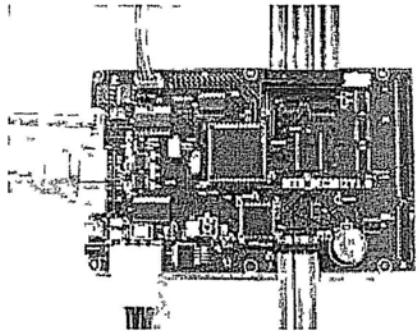

Figure 2 13· Outlook of the DSP

and sends it to the four driving motor controllers The complexity found in the differential part of a traditional vehicle is greatly reduced in this drive-by-wire subsystem. Table 2 1 shows that the directions of the four driving motors are different for each of the six patterns (three modes and two directions for each mode)

'B' and 'F' denote backward and forward, respectively

As discussed in the software subsection, the DSP mode and the shift status are updated via communication between the PC104 and the DSP

Table 2.1: Directions of driving motors

	Forward (♯1 ♯2 ♯3 ♯4)	Backward (♯1 ♯2 ♯3 ♯4)
front-wheel-steering	(B B F F)	(F F B B)
ZRT	(F F F F)	(B B B B)
LP	(F B B F)	(B F F B)

2.4.3 Peripherals

In designing a steering subsystem, the absolute position of the steering angle for each steering mechanism is a significant issue because although Maxon found it easy to integrate an encoder into the steering motor, it is effective only as a relative position sensor and calibration is required for each power-on step.

Although McKerrow [11] has studied the calibration of steering angles, the complicated calibration method proposed has to be conducted for every power-on step.

In the ISDV, I utilize an optical sensor as a homing sensor for each steering motor to alleviate the calibration problem. Figure 2.14 illustrates this concept. A blocking piece in the shape of a semi-circular edge is cut off a circle plate and fixed to the upper end of the output shaft of the speed-reduction gearbox. Within one turn of the output shaft, the optical sensor is blocked for 180 degrees and a voltage difference is consequently generated. Hence, employing the edge of the voltage change is an ideal absolute position calibration method.

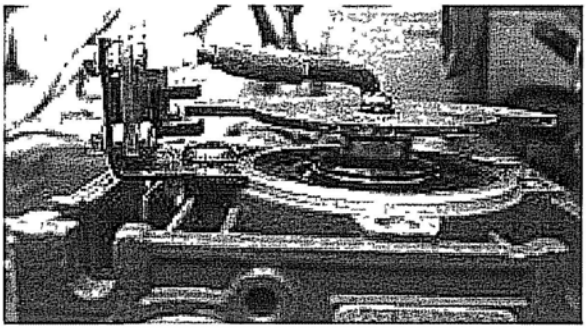

Figure 2.14: Homing device

2.4.4 Software

Because of the large quantity of controllers and ports-two kernel controllers, eight peripheral controllers, two RS232 ports, and one USB port-much attention has to be paid to synchronization to prevent conflict.

Between the two kernel controllers, the PC104 is the master and the DSP works as a slave.

PC104 Program

The PC104 algorithm includes two structural variables. The first is called VehicleState and is used for the storage of mode, shift, steering wheel angle, and velocity. The other is TempVehicleState and stores mode and shift as temporary inputs from the steering wheel. For real time performance, three threads work simultaneously: ThreadSWRead, ThreadUpdateState, and ThreadEPOSControl. Their functions are as follows:

1. ThreadSWRead: reads messages from the steering wheel and updates VehicleState.angle if any change in the steering angle occurs. If there is any change in the mode button or the shift bar, TempVehicleState.mode

or TempVehicleState.shift will be updated only if VehicleState.velocity $= 0$, i.e. the vehicle is not in motion.

2. ThreadUpdateState: This thread idles until TempVehicleState.mode $\neq$ VehicleState.mode or TempVehicleState.shift $\neq$ VehicleState.shift. If there is difference in mode, it first interrupts the usage of the EPOS RS232 port from ThreadEPOSControl to prevent conflict. Thereafter, it sends a command to each EPOS for initialization to the new mode. When successful, it then starts communicating with the DSP to change its mode state. If the entire flow is successful, it ultimately sets the new mode to VehicleState.mode. If there is a difference in shift, it transmits the relevant information to the DSP, and with a successful acknowledgement, it then updates VehicleState.shift.

3. ThreadEPOSControl: In this thread, the algorithm calculates the four steering angles according to VehicleState.mode and sets these angles to the target angles for the four EPOS controllers. However, if there is any signal from ThreadUpdateState to release possession of the EPOS RS232 port, it will pause in its communication with EPOS and start idling.

Figures 2.15 2.16 and 2.17 show flowcharts for the control algorithms.

DSP Program

The DSP supports a single thread and has the functions listed below:

1. Obtains the vehicle's velocity by timing the duration between two rising

Figure 2.15: Flowchart of ThreadSWRead

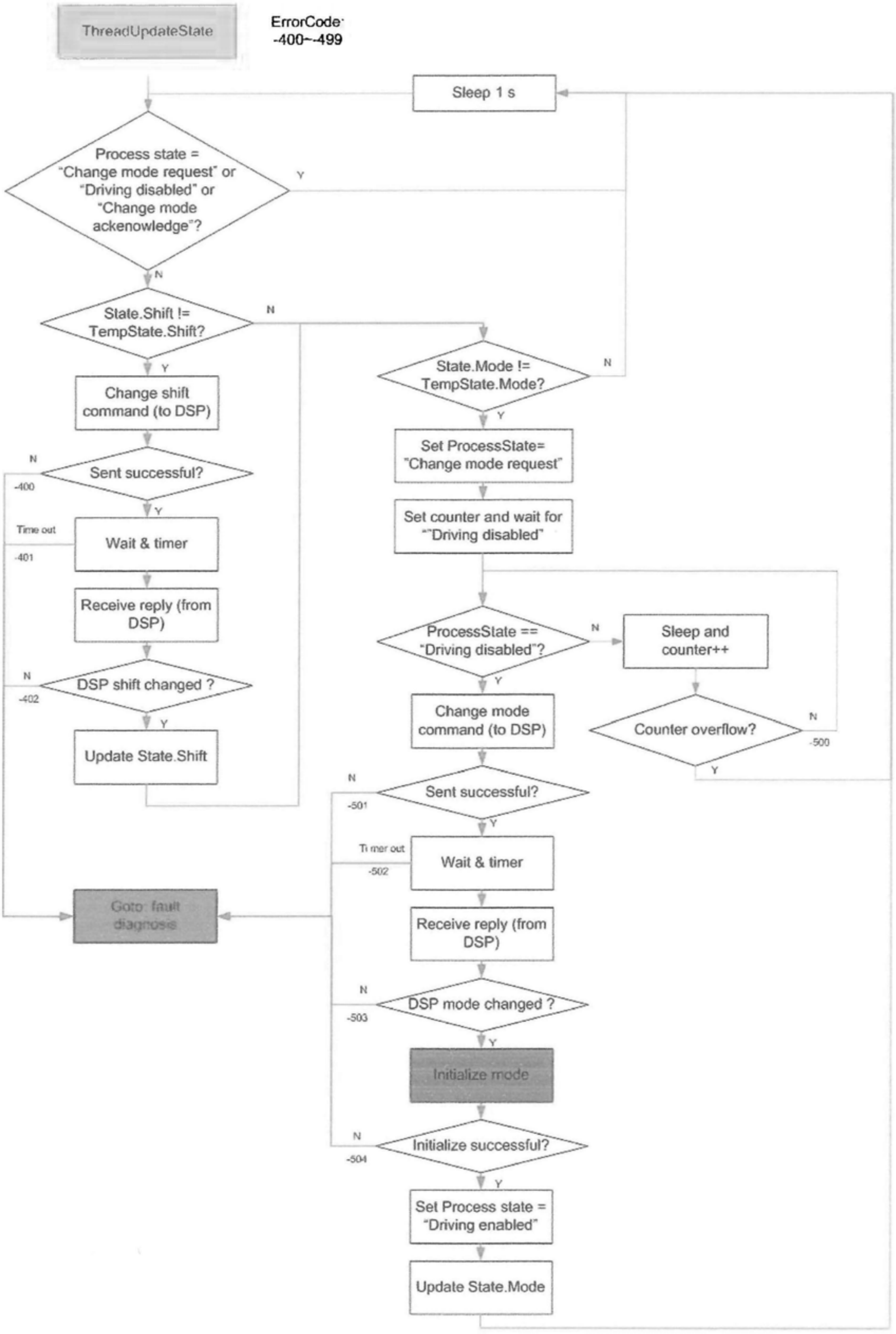

Figure 2.16: Flowchart of ThreadUpdateState

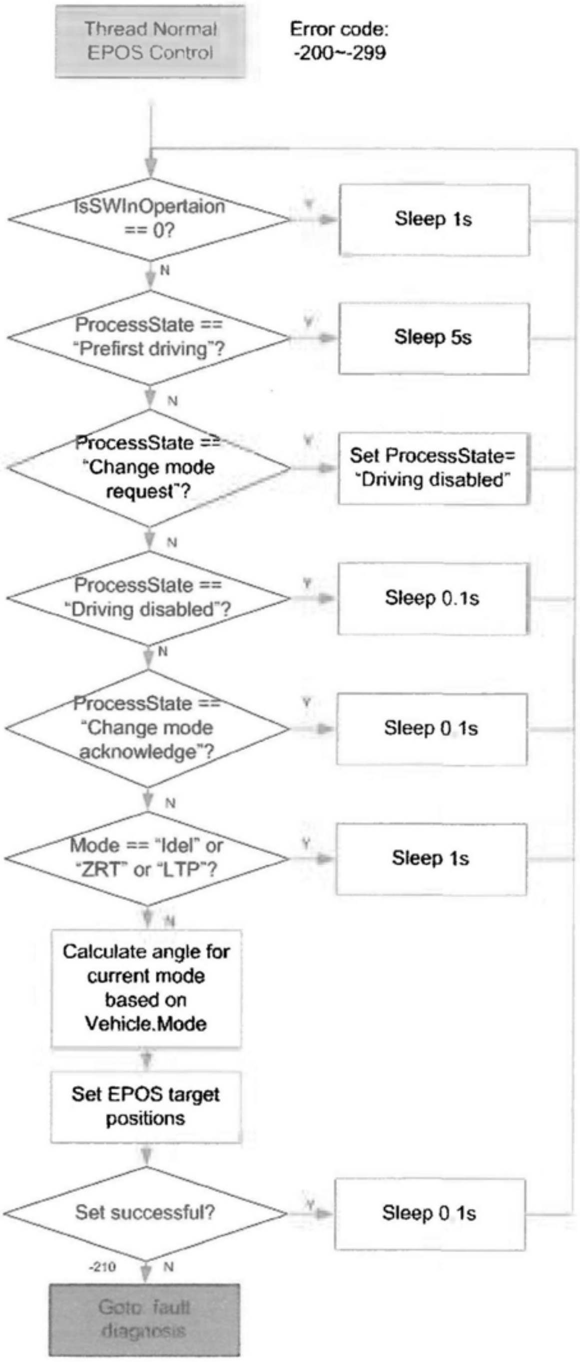

Figure 2.17: Flowchart of ThreadEPOSControl

edges of one hall channel in the left front in-wheel motor. The velocity is sent to the PC104 via the RS232 port.

2. Digitizes the voltage signal of the electronic acceleration pedal by A/D, calculates acceleration voltage signals for the four driving motor controllers, and outputs them.
3. If there is any mode/shift change demand from the PC104, it will change the mode/shift state in the DSP and reply if successful.

PC104-DSP Protocol

In communication between the PC104 and the DSP, for the avoidance of conflict, the PC104 is the master that initiates communication and the DSP is the slave. The PC104 sends two types of frames to the DSP: command frames and data frames. The command frames code mode change commands or shift change commands and the data frames include the current angles of the four wheels. In contrast, the DSP acknowledges and replies through messages indicating whether the mode/shift change has been successful and including velocity and acceleration information. To ensure accurate communication, 16-bit CRC coding is attached to each frame.

2.5 Human-vehicle Steering Interface

Because the new vehicle has the omni-directionality, the traditional human-vehicle interface, including a steering, a shift lever, an acceleration pedal and a braking pedal, can not support all the omni-directional motions. As a result, the human-vehicle interface should be re-designed.

In my research, I have considered controlling the vehicle through two types of methods. The first approach switches among front-wheel-steering, zero-radius-turning and lateral-parking discretely, through mode buttons. This can switch between the practical modes and the most frequent mode is still front-wheel-steering, so the driver does not need to change driving habit too much. The other approach change ICR continuously. This will make the vehicle motion more flexible.

2.5.1 Steering Interface with Discrete Mode Change

Figure 2.18 illustrates the interface with discrete mode change. I adopt Logitec Momo as the steering wheel. Of the six buttons on the steering wheel panel, I select four for mode changes to "idle operation", "front-wheel steering, "zero radius turning", and "lateral parking". The shift bar is also integrated into the steering wheel device.

The switch panel on the top right includes power switches for cooling fans, the PC104, the DSP, and peripheral controllers. The LCD, the keyboard, and the mouse function as standard I/O PC104 apparatus for debugging and testing.

The electronic accelerator pedal and the brake pedal are located in the same position as in traditional vehicles.

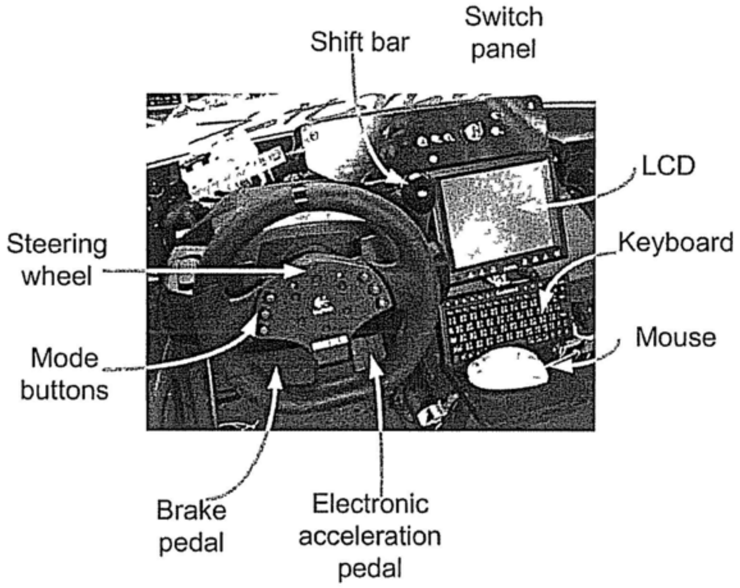

Figure 2.18: User interface

2.5.2 Steering Interface with Continuous ICR Allocation

The steering interface utilizes buttons enabling the driver to switch among different steering modes such as front-wheel steering, zero radius turning, and lateral parking. However, the shortcoming of this system is that the vehicle must have come to a complete stop before the driver can switch to another mode. In addition, the driver may not be able to steer the vehicle at the desired ICR due to the steering mode restriction. This does not allow for the omnidirectional maneuverability of the 4WIS vehicle to be utilized.

The conventional steering interface provides only one steering input (rotation of the steering wheel) that is inadequate for defining all ICRs in the horizontal plane. There is therefore a need to extend the steering interface for the ISDV. Given the application of steer-by-wire technology, the extended steering interface is mainly aimed at defining the target ICR and passing it to the steering motor controller. The extended steering interface is designed to provide a user-friendly interface enabling the driver to locate the desired ICR without having to switch mode.

Interface Design

The concept underlying the proposed steering interface is shown in Figure 2.19. The interface can be treated as an extension of a conventional steering interface. A sliding rail is attached to a conventional steering wheel to give the steering wheel two DOFs: rotation and translation. In addition, a sliding button is added beside the steering wheel. The symbols $\Phi 1$, $\Phi 2$, and $\Phi 3$ represent the steering inputs. All ICRs can be defined by a combination of steering inputs. The extended steering interface is operated intuitively and conventional steering behavior is reserved. Turning the steering wheel corresponds to a turning motion, whereas sliding the steering wheel corresponds to a pure translation motion. The joints can also be controlled simultaneously to represent a combined turning and translation motion.

Defining Target Instantaneous Center of Rotation

Figure 2.20 illustrates the relationship among the ICR, the ICR axis, and the steering inputs. An abbreviated single-track model is employed to illustrate the concept underlying the interface. In the figure, $(x_F, 0)$, $(x_R, 0)$, and $(\Phi 3, 0)$ are the coordinates of the oriented center of the front wheels, the oriented center of the rear wheels, and the origin of the ICR axis, respectively. The origin of the ICR axis is the point at which the ICR axis and the x-axis

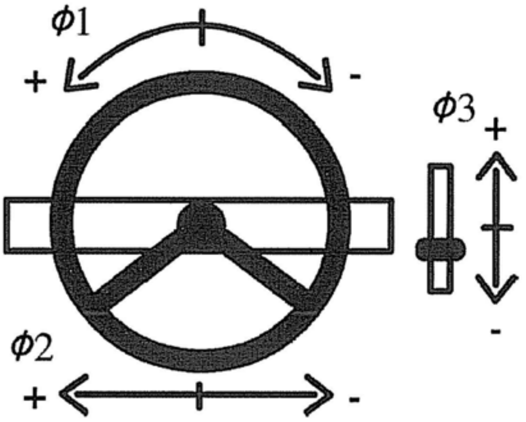

Figure 2.19: Extended steering interface

intersect. The origin of the coordinate system is located at the geometric center of the vehicle.

In the figure, $\cot(\Phi 1)$ defines the distance between the ICR and the origin of the ICR axis, $\cot(\Phi 1) > 0$ represents a left turning motion (turning anti-clockwise about the ICR), while $\cot(\Phi 1) < 0$ represents a right turning motion (turning clockwise about the ICR). The steering result is equivalent to that realized through a conventional 2WS steering system when $\Phi 2 = 0$ and $\Phi 3 = x_R$. To make the handling more intuitive, the left turning motion is performed only when the steering wheel is turned in an anti-clockwise direction and the right turning motion is performed only when the steering wheel is turned in a clockwise direction. As a result, the value of $\Phi 1 = 0$ is restricted to the range of $-\pi/2 \leq \Phi 1 \leq \pi/2$. This restriction limits the continuous motion of the ICR and prevents it from passing through the origin of the ICR.

The symbol $\Phi 2$ defines the angle between the ICR axis and the y-axis.

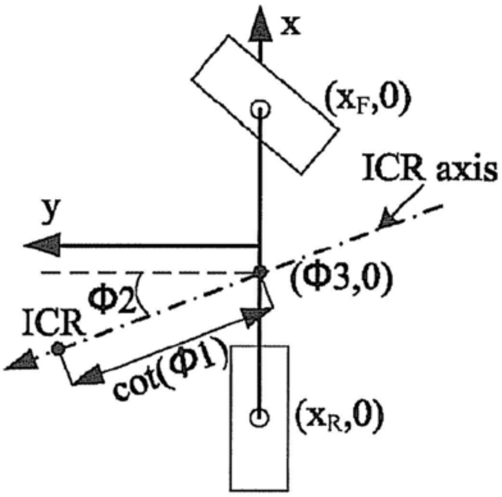

Figure 2.20: Relationships among ICR, ICR axis, and steering inputs

When $\Phi1 = 0$, changing the value of $\Phi2$ makes the vehicle perform a pure translation motion in different directions, as shown in Figure 2.21(d). To make the handling more intuitive, the left translation motion is performed only when the steering wheel is slid to the left and the right translation motion is performed only when the steering wheel is slid to the right. As a result, the value of $\Phi2$ is restricted to the range of $-\pi/2 \leq \Phi2 \leq \pi/2$.

The symbol $\Phi3$ defines the position of the origin of the ICR axis. Theoretically, $\Phi1$ and $\Phi2$ in themselves are sufficient to define the location of the ICR in the 2D plane. The additional steering input $\Phi3$ is introduced to allow for several forms of conventional steering behavior that make steering more intuitive to be emulated. For instance, when $\Phi2 = 0$ and $\Phi3 = x_R$, the vehicle performs as a typical front 2WS vehicle as shown in Figure 2.21(a); when $\Phi3 = (x_F + x_R)/2$, the vehicle performs as a typical 4WS vehicle as shown in Figure 2.21(b); when $\Phi3 = x_F$, the vehicle performs as a typical two rear

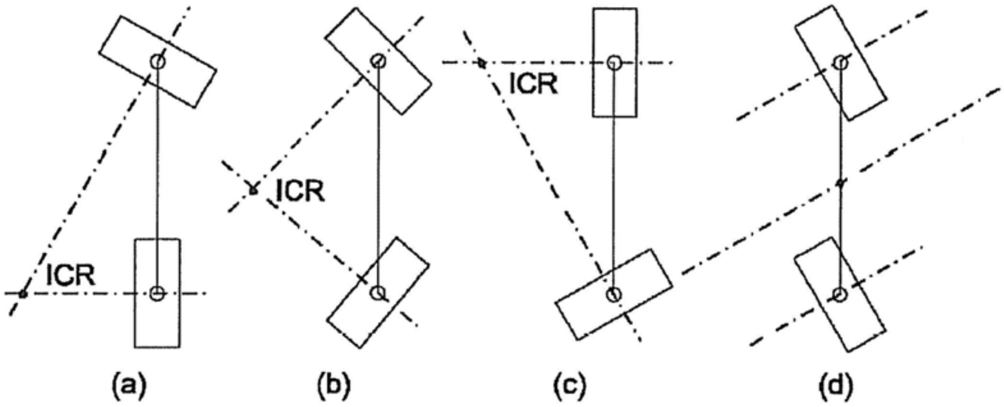

Figure 2.21: Examples of steering results

wheel steering (2RWS) vehicle as shown in Figure 2.21(c). The coordinates of the target ICR (x^T_{ICR}, y^T_{ICR} can be defined by following equation:

$$\begin{bmatrix} x^T_{ICR} \\ y^T_{ICR} \end{bmatrix} = \begin{bmatrix} \cos\Phi 2 & -\sin\Phi 2 \\ \sin\Phi 2 & \cos\Phi 2 \end{bmatrix} \begin{bmatrix} 0 \\ \cot\Phi 1 \end{bmatrix} + \begin{bmatrix} \Phi 3 \\ 0 \end{bmatrix} = \begin{bmatrix} \Phi 3 - \cot\Phi 1 \sin\Phi 2 \\ \cot\Phi 1 \cos\Phi 2 \end{bmatrix} \tag{2.3}$$

Given the combination of these steering inputs, the vehicle can be commanded to turn about any ICR or to translate in any direction. There is no need to perform any mode switching operation.

Defining Target Orientations of Wheels

Once the target ICR has been defined, the target orientations of the wheels can be determined. Under the kinematic constraint, the orientations of the wheels must comply with the following constraint:

$$\vec{\omega} \times (\vec{r}_\imath - \vec{r}_{ICR}) = \vec{v}_\imath \tag{2.4}$$

where $\vec{v}_\imath$ is the longitudinal velocity of wheel $\imath$, and $\vec{r}_\imath$ and $\vec{r}_{ICR}$ are the position vectors of the center of wheel $\imath$ and the ICR, respectively. In the extended steering interface, $\Phi 1 \neq 0$ and $\Phi 1 = 0$ represent a turning motion and a translation motion, respectively. For $(x^T_{ICR}, y^T_{ICR}) \neq (x_\imath, y_\imath)$, the target orientation of wheel $\imath$ can be obtained as follows:

1) If $\Phi 1 = 0$, $\delta^T_\imath = \Phi_2$.

2) If $\Phi 1 \neq 0$,

$$\delta^T_\imath = \begin{cases} \frac{\pi}{2} & y_\imath = y^T_{ICR} \\ \frac{x_\imath - x^T_{ICR}}{-(y_\imath - y^T_{ICR})} & y_\imath \neq y^T_{ICR} \end{cases} \tag{2.5}$$

Moreover, if $y^T_{ICR} = y_\imath$, there will be a singular line, the opposite side of which will undergo a sudden change by π *rad*. Even if the ICR does not pass through the singular point, but only comes close to it, it may also lead to a huge change in the target orientation. The steering actuator may not be fast enough to move to the target orientation. As a result, the target ICR is best kept away from the singular points and singular lines.

Hardware Prototype

Figure 2.22 shows the hardware prototype of the extended steering interface. In the extended steering interface, the turning ($\phi 1$) and sliding ($\phi 2$) joints are connected to a force feedback motor. The steering wheel is mounted directly onto the output shaft of the force feedback motor, while the slide rail is connected to the force feedback motor through the rack and pinion. Each motor is equipped with an optical encoder to obtain the posture of each joint. A micro controller collects the posture of the steering interface and sends it to the vehicle control system. The micro controller also acts as the force feedback controller by acquiring the appropriate interface posture from the vehicle control system.

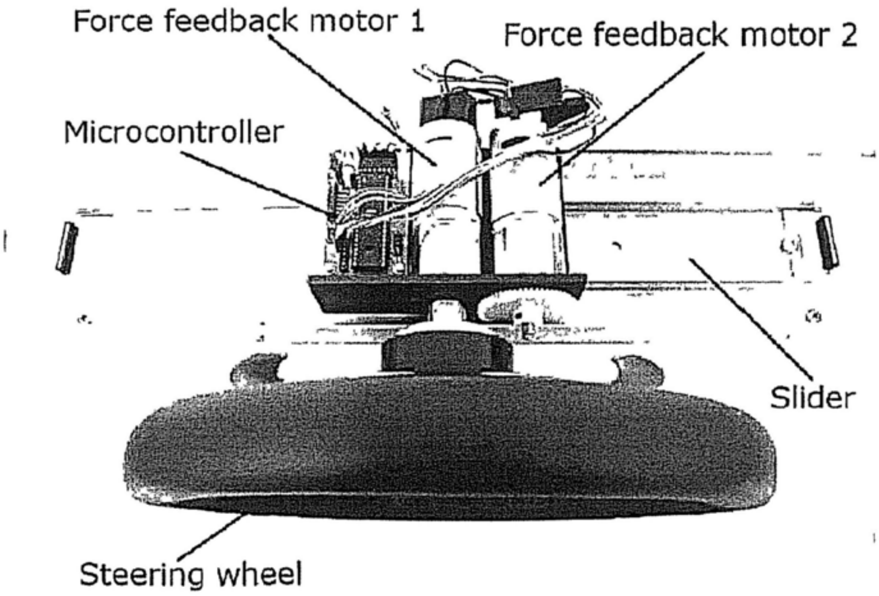

Figure 2.22: Prototype of the extended steering interface

Simulation Platform and Experiments

For safety reasons, the proposed design and algorithms of the extended steering interface must be verified in a virtual environment before being implemented in a real vehicle. The verification process is carried out through HIL simulations. In the following simulations, the real-time Windows target [41] in MATLAB is selected as the HIL simulation environment. To realize the steering effect, the Virtual Reality Toolbox [42] is used to visualize the motion of the vehicle.

Figure 2.23 shows the HIL simulation platform as a whole. The architecture of the HIL simulation environment consisting of a host PC and real hardware is illustrated in Figure 2.24. The real hardware used in the simulation environment includes the extended steering interface and a foot pedal. Communication between the host PC and the real hardware is channeled through an RS232 serial line. The host PC acts as a vehicle control system that communicates with the extended steering interface and receives the signal from the foot pedal. It calculates the target orientations of the wheels and the appropriate steering interface posture according to the information acquired from the extended steering interface and the vehicle model, respectively. It also acts as a steering motor controller. The motion of the vehicle and the wheels can be visualized in the virtual reality environment. In the extended steering interface, the steering input ϕ_3 is realized virtually in the host PC. The foot pedal is included to define the longitudinal driving force of each wheel.

In the HIL simulation, the author attempts to steer the vehicle with different steering inputs. Figure 2.25 shows some of the simulation results with $\phi_3 = -1.25$. The ICR can be changed to any point at any time. The extended steering interface provides the driver with omnidirectional controllability and allows the driver to experience a novel and powerful driving style.

Due to the limitation of time, this interface has not be integrated into

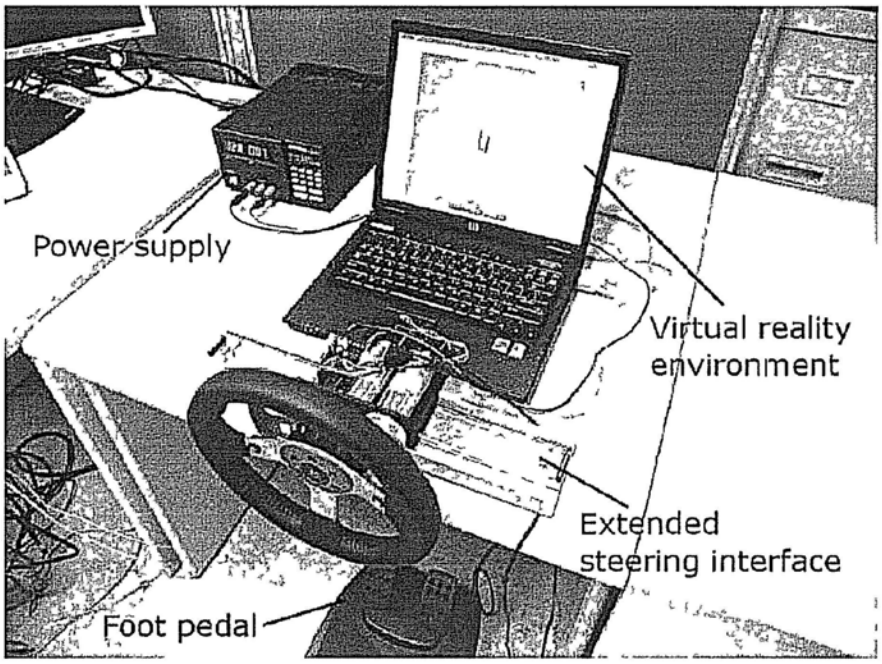

Figure 2 23· HIL simulation platform

the final vehicle yet. The proposed vehicle structure with the extend steering interface is illustrated as below

2.6 Vehicle Integration and Implementation

Implementation of Omni-directional Motions

Figure 2.27 provides an overall illustration of the ISDV

Table 2 2 lists the specifications of the ISDV

Having described development of the ISDV, I now turn to realization of the ZRT and LP functions and demonstrate the significant advantage of the ISDV in parking scenarios Tests (Figure 2 28 and 2 29) are carried out in scenarios featuring two common parking slot arrangements (i) vehicles

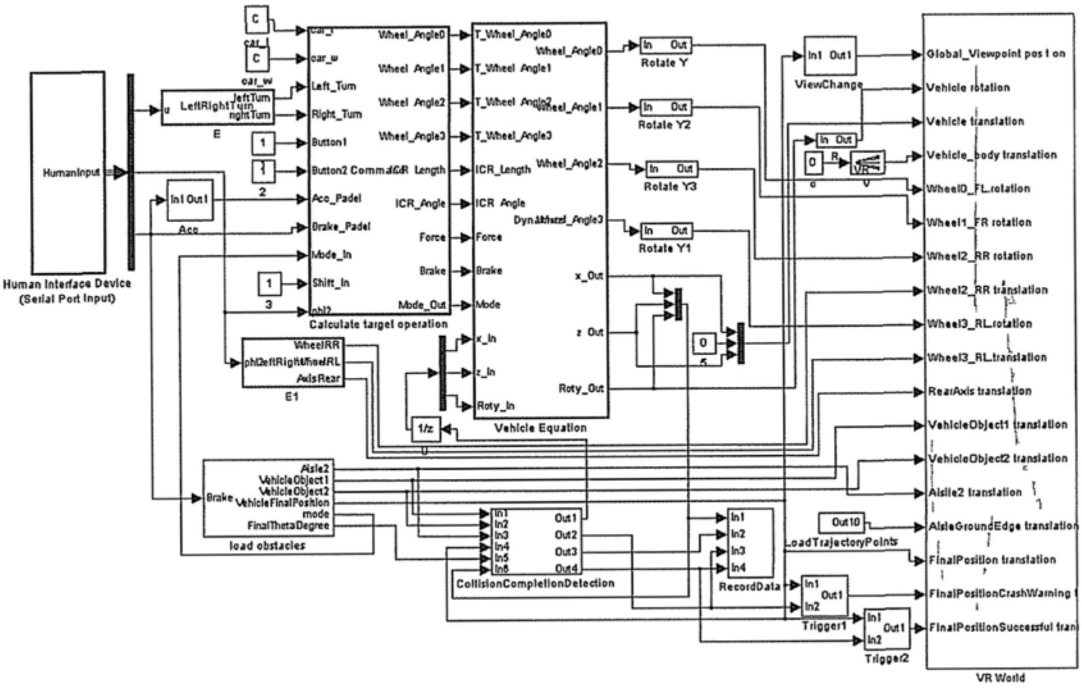

Figure 2 24 System blocks in simulink

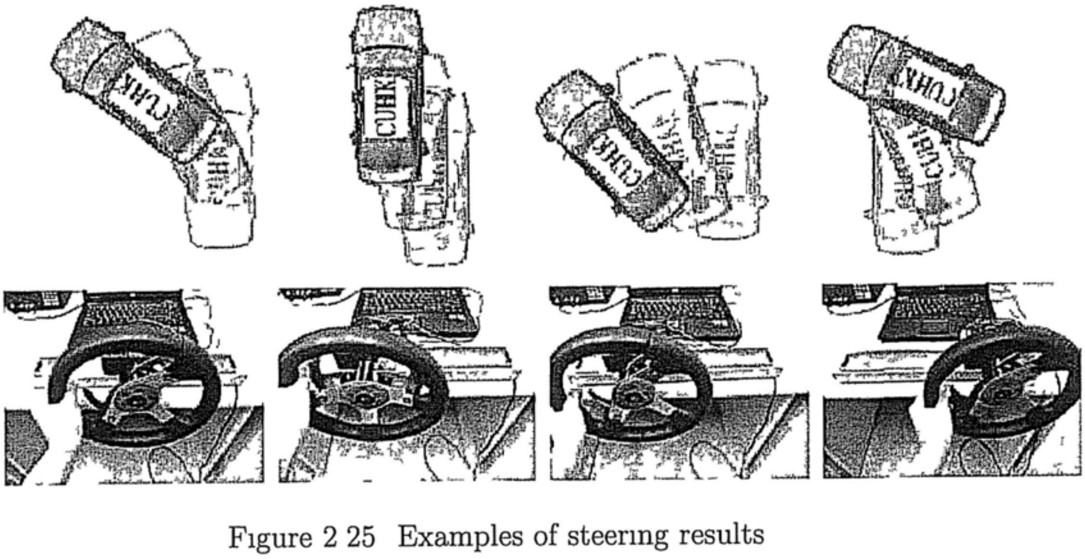

Figure 2 25 Examples of steering results

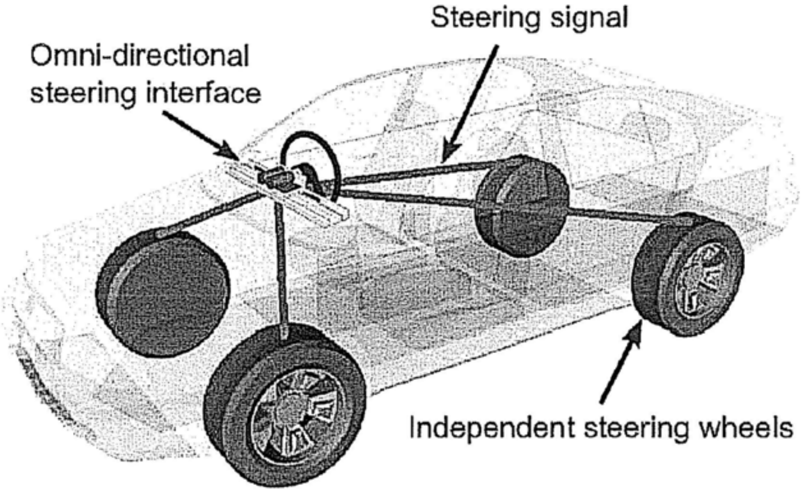

Figure 2.26: Omni-directional steer-by-wire system

Figure 2.27: Outlook of the ISDV)

Table 2.2: System specification of the ISDV

Wheel base	1.8m
Vehicle width	1.8m
Vehicle length	2.6m
Front overhang	0.4m
Rear overhang	0.4m
Mass	300kg
Driving motor	48V, 600W
Steering motor	42V, 90W
Battery	48V, 44Ah

parked head-to-tail; and (ii) vehicles parked side-by-side.

The experiment shows that both the ZRT and LP functions of the ISDV perform well. The demands placed on the driver in trajectory selection and generation are greatly reduced. The decoupling of rotation and translation enables the driver to manipulate the vehicle more freely and easily.

2.7 Summary

This chapter gives a detailed description of the design and development of the ISDV. The kinematic modeling of traditional front-wheel steering vehicles is initially discussed before turning to that of ISDV with motion capabilities including arbitrary ICR turning, zero radius turning, and lateral parking. The chassis system adopted for the ISDV including its chassis frame and its steering and driving mechanism are described in detail. The control framework including a four-wheel independent steering subsystem and a four-wheel independent driving subsystem with electronic peripherals and a control in-

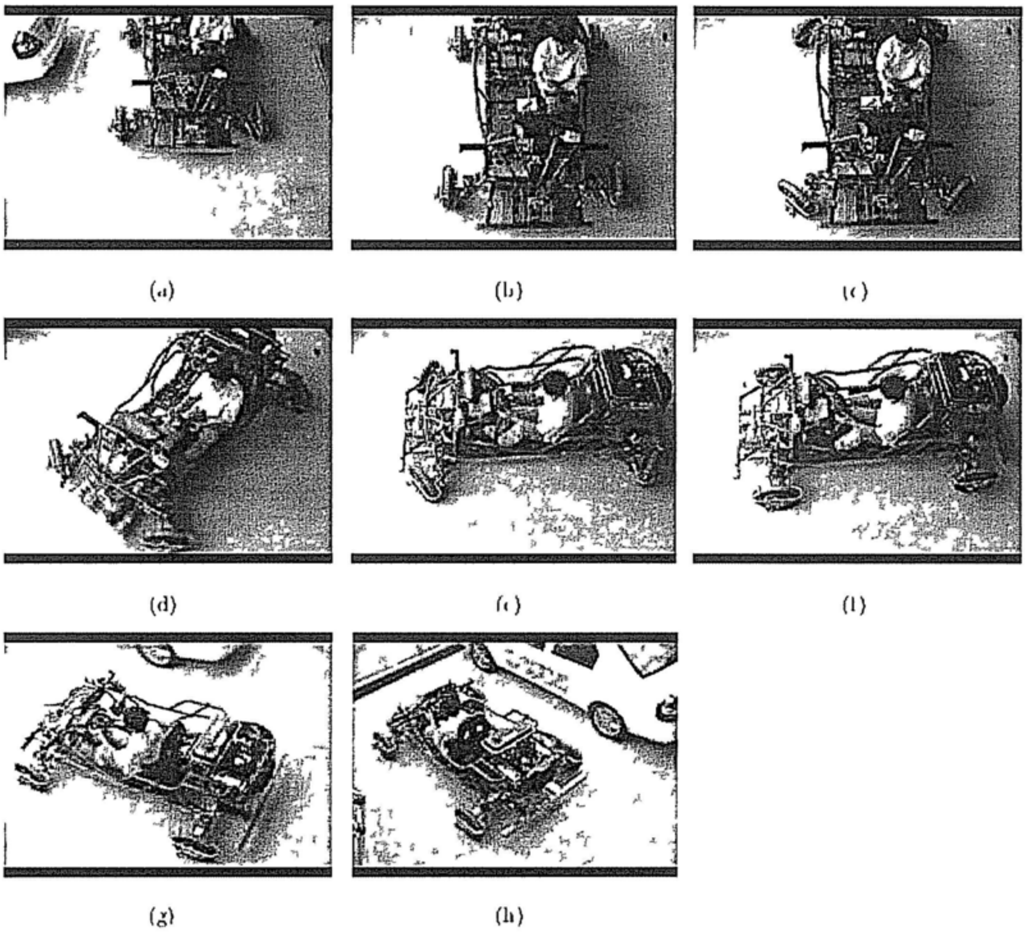
(a) (b) (c) (d) (e) (f) (g) (h)

Figure 2 28 Implementation of zero radius turning

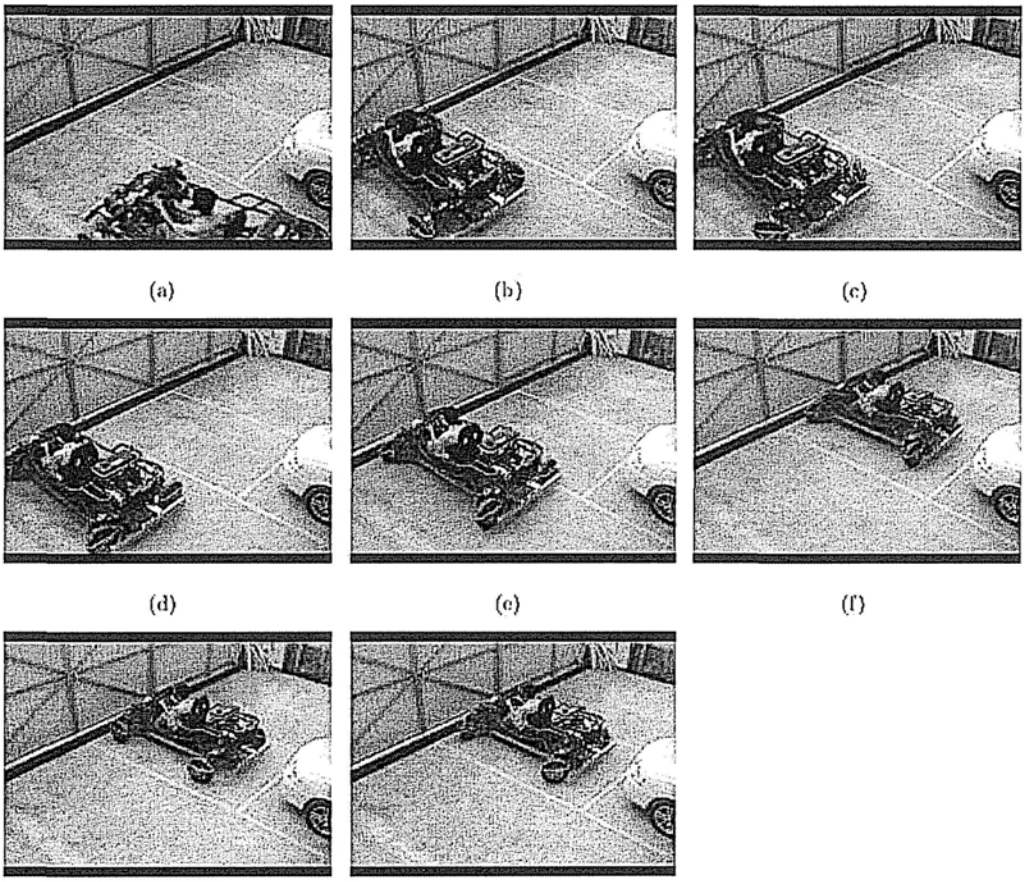

(a) (b) (c) (d) (e) (f) (g) (h)

Figure 2.29: Implementation lateral parking

terface is then introduced. Software flowcharts are also provided to clarify the systems employed in the vehicle. Finally, two steering interfaces are developed and elaborated. One enables discrete mode change so as to realize the front-wheel-steering, zero-radius-turning, and lateral-parking, while the other takes fully utilization of the omni-directionality by continuously allocating the ICR.

Chapter 3

Energy Management of the Independent Steering and Driving Vehicle

3.1 Introduction

Energy has been a global problem over the course of human civilization. On the one hand, transportation boosts human civilization by allowing us to work more quickly and produce more. On the other hand, it consumes a great deal of energy, especially non-renewable fuels such as gasoline and diesel.

These non-renewable energy sources on which human civilization is so dependent nowadays will ultimately be depleted if no solution to the supplydemand imbalance is found. Transportation accounts for significant proportion of the fuel consumed in the world. Encouragingly, much effort has been directed toward enhancing energy efficiency and reducing energy loss. These endeavors include both technological and non-technological solutions [64]. There has also been a major focus on exploring new energy sources such as electric batteries, fuel cells, and flywheels. Powertrains in motor vehicles use electrical energy to propel the vehicle.

In vehicle research, hybrid electric vehicles (HEVs) and electric vehicles (EVs) have been developed and improved with the goal of transforming electrical energy into more highly efficient kinematic energy. Much effort has been devoted to managing engine and motor energy in HEVs [71] [72] [73] [74]. Some HEVs such as the Toyota Prius [75], the Honda CivicHEV [76], and the BYD Dual Mode F3 [77] have been commercialized. Studies of energy management in EVs assess the reduction of energy expenditure brought about by the deactivation of auxiliary devices such as air conditioners and lighting when the surrounding environment permits [61], wheel slippage reduction [66], and dual energy sources comprising a battery and an ultra capacitor [62] [63].

The advent of EVs has revealed the start of a technological revolution in which fuels are replaced by electricity, a cleaner and renewable source of energy. However, there is still a long way to go before the driving distance per charge is long enough to make EVs acceptable to drivers. Enhancing the efficiency of the propelling actuator-the motor-is one promising research direction.

Because most EVs are driven by a single traction motor such as those described by [53] and [54], efficiency improvements have to deal with technical methodologies facilitating the manufacture of a motor that loses less energy through heat resistance, friction, etc.

In the robotics field, four-wheel independent drive (4WID) or direct drive technologies have resulted in a rich literature on mobile robots. Some examples are the Titan (Ratner 2000), a 4WD wheelchair [80], a four-wheel differentially steered (4WDS) mobile robot [81], and a 4-wheel omnidirectional mobile robot [82], and so on. This research has attracted much attention to the fields of traction control and robot traversability [67] [65]. However, few studies in the robotics area focus on energy management in the 4WID configuration. This might be due to the non-urgency of the energy-saving issue given the relatively small quantity of robots in service. However, energy saving is very important in the auto industry and is therefore explored in this thesis.

In the vehicle industry, energy consumption is evaluated by driving the vehicle in a number of predetermined driving cycles to assess speed in respect to time based on numerous statistical driving data. In a traditional EV, a single high-power traction motor is responsible for propelling the whole vehicle [68]. In an established driving cycle, there is no room for power management in this traction motor because all it can do is to output the overall level of power demanded by the driver.

In contrast, if the number of motors is increased to $\mathrm{N}(\mathrm{N} > 1)$, several low-power motors can work together and increase the DOF to $\mathrm{N} - 1$.

Thus, the 4WID configuration has the potential to reduce energy consumption further by managing the power within its four driving motors to improve energy efficiency.

Based on the statistics in [69], the motors used in transportation equipment in the late 1990s reached approximately 1800 TWh/year in the US. With the emergence of EVs, this energy consumption figure will now be significantly higher. As a result, 4WID technology can make a greater contribution to energy efficiency.

This chapter analyzes the energy efficiency improvement brought about by the 4WID structure. Section 2 introduces the modeling of EVs in standard conditions. Motor models including those for the traditional traction motor and the in-wheel motor for 4WID vehicles are also discussed. Section 3 introduces a map grid refinement for acceptable torque/speed precision. Optimal torque distribution (OTD) strategies are discussed in Section 4. In Section 5, I compare the two torque distribution strategies with the traditional single motor driving approach based on an overall efficiency map. In Section 6, simulations are conducted for validation. Section 7 concludes the chapter.

3.2 Modeling of Electric Vehicle Powertrain

3.2.1 Vehicle Dynamic Model

For the most general case, i.e. EV on a slope, Figure 3.1 illustrates the 4WID configuration.

The slope gradient is $\tan(\theta)$. N_i $(i = 1, 2, 3, 4)$ are the slope normal upthrust forces on the left front, left rear, right rear and right front wheels, respectively. F_{drivei} , F_{rolli}, and T_i $(i = 1, 2, 3, 4)$ are the driving forces directly

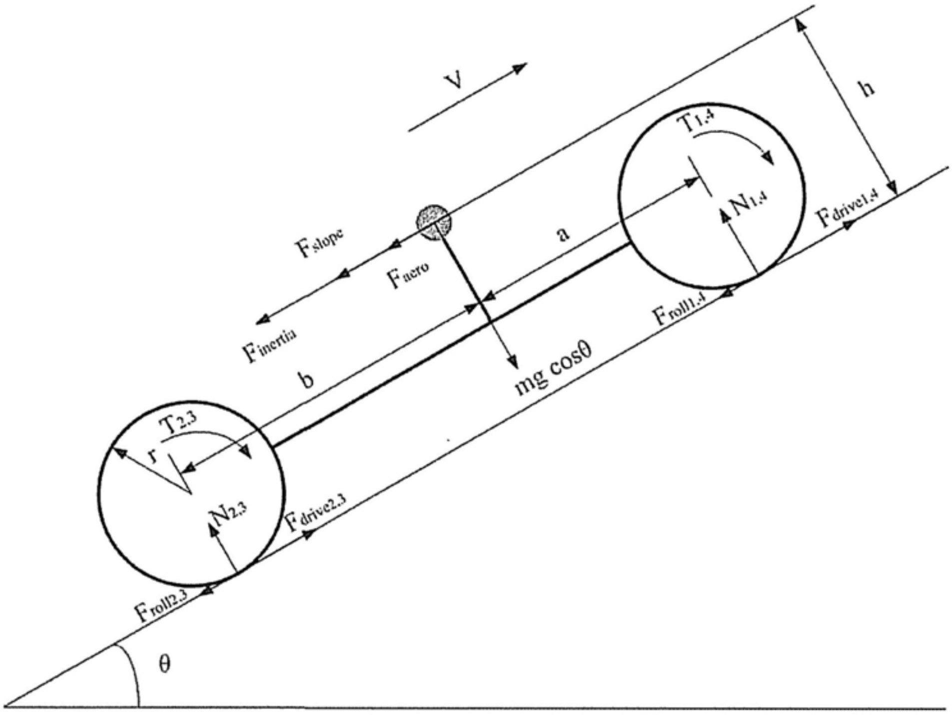

Figure 3.1: 4WID configuration on a slope

generated by tyre-road friction, rolling friction, and the torque of the in-wheel motor, respectively, subject to the same indexing rule as that applicable to the upthrust force. F_{slope}, $F_{inertia}$, and F_{aero} are the dragging forces due to the slope, vehicle inertia acceleration/deceleration, and aerodynamic friction, respectively. All other denotations and values are indicated in Table 3.1. The vehicle parameters are based on the Smartcar EV [53] configuration with a maximum speed of 100 km/h.

The vehicle dynamic equations can be derived as follows and are utilized to compute the total driving torque T_{total} for each second in a driving cycle.

Table 3.1: Denotations and values for electric vehicle powertrain modeling

Parameter	Symbol	Unit	Value
Vehicle total mass	m	kg	1144
Wheel radius	r	m	0.282
Wheel inertia	$\mathrm{I_{wh}}$	$\mathrm{kgm^2}$	3.2639
Center of gravity (CG) height	h	m	0.5
Distance (front axis to CG)	a	m	1.04
Distance (rear axis to CG)	b	m	1.56
Rolling resistance coefficient	μ_r		0.009
Maximal adhesive coefficient	μ		0.9
Air friction coefficient	$\mathrm{C_D}$		0.335
Wind contact area	A	$\mathrm{m^2}$	2
Air density	ρ	$\mathrm{kg/m^3}$	1.2
Traditional EV gearbox ratio	ζ		10.6385

$$\sum_{i=1}^{4} F_{drivei} = F_{slope} + F_{aero} + F_{inertia} + \sum_{i=1}^{4} F_{rolli} \tag{3.1}$$

$$T_i = r(F_{drivei} - F_{rolli}) + \frac{I_{wh}}{r}\frac{dv}{dt} \tag{3.2}$$

From equations 3.1 and 3.2, the total torque is

$$T_{total} = \sum_{i=1}^{4} T_i = r(F_{aero} + F_{inertia} + F_{slope}) + \frac{4I_{wh}}{r}\frac{dv}{dt} \tag{3.3}$$

where

$$F_{slope} = mg\cos(\theta)$$
$$F_{aero} = \frac{1}{2}C_D A \rho v^2$$
$$F_{inertia} = m\frac{dv}{dt}$$

3.2.2 Powertrain Model of Electric Vehicle with Single Motor

Electric Motor Model

The Smartcar EV is propelled by a 30kW motor (MC_AC75) with peak efficiency of 0.92. The motor efficiency map [60] is a key to evaluating its performance. Figure 3.2 shows the efficiency map for this single motor denoted as $\eta_0(\omega_0, T_0)$.

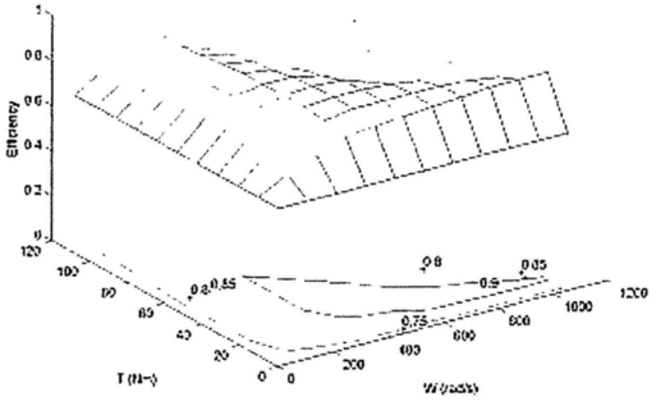

Figure 3.2: Electric Motor Model

Gearbox Model

In the 4WID vehicle, because four independent in-wheel motors are utilized for direct propulsion, there is no need for a gearbox. However, in the traditional EV structure, a gearbox is required to reduce the speed of the motor output shaft and increase the torque for final wheel drive. Efficiency is shown in Figure 3.3.

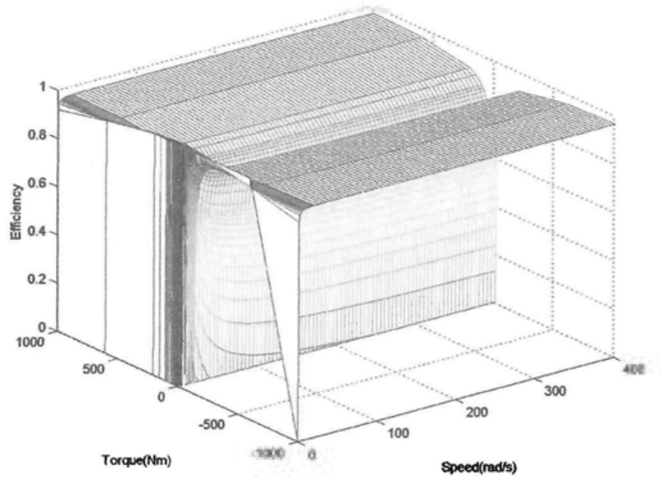

Figure 3.3: Gearbox Efficiency Map

Overall Powertrain Efficiency Model

In the single motor propelled EV, the output speed and the output torque of the driving motor are

$$\omega_0 = \omega_{wh}\zeta \tag{3.4}$$

$$T_0 = \frac{T_{total}}{\zeta\eta_{gb}(\omega_{wh}, T_{total})} \tag{3.5}$$

where $\zeta = 6.6732$ is the gearbox ratio for the EV SMART and η_{gb} is gearbox efficiency.

The total input power is

$$P_0 = \frac{\omega_0 T_0}{\eta_0(\omega_0, T_0)} = \frac{\omega_{wh} T_{total}}{\eta_{gb}(\omega_{wh}, T_{total})\eta_0(\omega_0, T_0)} \tag{3.6}$$

Thus the overall efficiency of the powertrain is

$$\eta_S(\omega_{wh}, T_{total}) = \eta_{gb}(\omega_{wh}, T_{total})\eta_0\left(\omega_{wh}\zeta, \frac{T_{total}}{\zeta\eta_{gb}(\omega_{wh}, T_{total})}\right) \tag{3.7}$$

where ω_0 and T_0 output the rotational speed and torque of the single traction motor, $\eta_{gb}(\omega_{wh}, T_{total})$ is gearbox efficiency, and ω_{wh} and T_{total} are the wheel speed and total driving torque.

3.2.3 Powertrain Model of Electric Vehicle with 4-wheel-independent-drive

To enable a fair comparison, the 4WID vehicle utilizes a similar efficiency map with only speed and torque scaling factors α and β and has total power equivalent to that of the MC_AC75.

$$\eta_i(\omega_i, T_i) = \eta_0(\omega_{0i}, T_{0i}) \tag{3.8}$$

$$\omega_i = \alpha \times \omega_{0i} \tag{3.9}$$

$$T_i = \beta \times T_{0i} \tag{3.10}$$

where $\eta_i(\cdot,\cdot)$, ω_i, and T_i $(i = 1, 2, 3, 4)$ are the efficiency, speed, and torque of the left front, left rear, right rear, and right front in-wheel motor, respectively; $(\omega_{0i} and T_{0i})$ are the speed and torque mapped from (ω_i, T_i) by scaling the factors α and β. $\alpha \times \beta = \frac{1}{4}$ to satisfy the total power constraint. It should be noted that (ω_{0i}, T_{0i}) is not the operational point (ω_0, T_0) of the single traction motor at the same point in the cycle.

It is assumed that both the two front wheels and the two rear wheels have the same torque as each other. Hence, there will be no yawing influence on vehicle stability. The overall efficiency of a 4WID car can be derived as follows.

$$\begin{aligned}
P_{in} &= 2\left(\frac{\omega_1 T_1}{\eta_1(\omega_1,T_1)} + \frac{\omega_2 T_2}{\eta_2(\omega_2,T_2)}\right) \\
&= 2\left(\frac{\omega_{wh} T_1}{\eta_1(\omega_{wh},T_1)} + \frac{\omega_{wh}(\frac{T_{total}}{2} - T_1)}{\eta_2(\omega_{wh},\frac{T_{total}}{2} - T_1)}\right) \\
&= \omega_{wh} T_{total}\left(\frac{\frac{2T_1}{T_{total}}}{\eta_1(\omega_{wh},T_1)} + \frac{1 - \frac{2T_1}{T_{total}}}{\eta_2(\omega_{wh},\frac{T_{total}}{2} - T_1)}\right) \\
&= P_{out}\left(\frac{\frac{2T_1}{T_{total}}}{\eta_1(\omega_{wh},T_1)} + \frac{1 - \frac{2T_1}{T_{total}}}{\eta_2(\omega_{wh},\frac{T_{total}}{2} - T_1)}\right)
\end{aligned}$$

$$\eta_{4WID} = \left(\frac{\frac{2T_1}{T_{total}}}{\eta_1(\omega_{wh}, T_1)} + \frac{1 - \frac{2T_1}{T_{total}}}{\eta_2(\omega_{wh}, \frac{T_{total}}{2} - T_1)}\right)^{-1} \tag{3.11}$$

where T_1 is the torque exerted by one front motor. The objective of torque distribution is to find the optimal T_1 that maximizes η_{4WID}.

3.3 Motor Map Grid Refinement

The original motor map contains only 11×11 grids in the first quadrant and in the non-negative parts of the motor speed and torque axes. The torque step $\Delta T_{mt} = 10.8$ Nm, corresponding to 115.2 Nm at the wheel, and the motor speed step $\Delta\omega_{mt} = 104.7 rad/s$. Hence, grid refinement is necessary to distribute torque more precisely.

Linear 2D interpolation is an approximating method for grid refinement. However, there are two motor maps on which grid refinement can be conducted: the motor efficiency map and the motor input power map. The problem is that the correct map matrix after refinement is unknown.

In the evaluation approach, the original maps of efficiency and input power are downgraded to two 6×6 maps by selecting the odd indexed value in the motor speed and torque axes. These maps are assumed to be known and the missing grids are assumed to be unknown.

Linear 2D interpolations are conducted on the downgraded maps.

3.3.1 Interpolation 1

$$\begin{aligned}\hat{\eta}_{eff}(n\Delta\omega_{mt}, m\Delta T_{mt}) = \frac{1}{4}[&\eta((n-i)\Delta\omega_{mt}, (m-j)\Delta T_{mt})\\ &+\eta((n-i)\Delta\omega_{mt}, (m+j)\Delta T_{mt})\\ &+\eta((n+i)\Delta\omega_{mt}, (m-j)\Delta T_{mt})\\ &+\eta((n+i)\Delta\omega_{mt}, (m+j)\Delta T_{mt})]\end{aligned} \tag{3.12}$$

where $i = 1$, if n is even; and $i = 0$, if n is odd; $j = 1$, if m is even; and $j = 0$, if m is odd. $n, m \in \{1, 2, 3, ...11\}$

The input power map based on the 2D interpolation on the efficiency map is computed as shown in equation 3.3.1.

$$\hat{P}_{eff}(n\Delta\omega_{mt}, m\Delta T_{mt}) = \frac{nm\Delta\omega_{mt}\Delta T_{mt}}{\hat{\eta}_{eff}(n\Delta\omega_{mt}, m\Delta T_{mt})} \tag{3.13}$$

3.3.2 Interpolation 2

Interpolation of the input power map denoted as $\hat{P}_{inpwr}(n\Delta\omega_m, m\Delta T_m)$ is conducted in a similar way. The estimated efficiency map based on the input power map interpolation is also calculated by

$$\hat{\eta}_{inpwr}(n\Delta\omega_{mt}, m\Delta T_{mt}) = \frac{nm\Delta\omega_{mt}\Delta T_{mt}}{\hat{P}_{inpwr}(n\Delta\omega_{mt}, m\Delta T_{mt})} \tag{3.14}$$

The two interpolations are compared with the original 11×11 maps and the figures below show the error difference. The mean errors on the efficiency maps by Interpolation 1 and 2 are 1.7% and 1.0% respectively, and the mean errors on the input power maps by Interpolation 1 and 2 are 524 watts and 383 watts, respectively.

Hence, it is better to adopt the input power map interpolation and calculate back the efficiency. From the shape of the maps, it can been seen that the input power map (Figure 3.5) is more linear than the efficiency map (Figure 3.2), which might explain its low mean errors.

I therefore choose to refine the input power map. Each $\Delta\omega_{mt}$ and ΔT_{mt} is broken into 10 uniform intervals, and thus the final refined map has dimensions of 101×101, as illustrated in Figure 3.5.

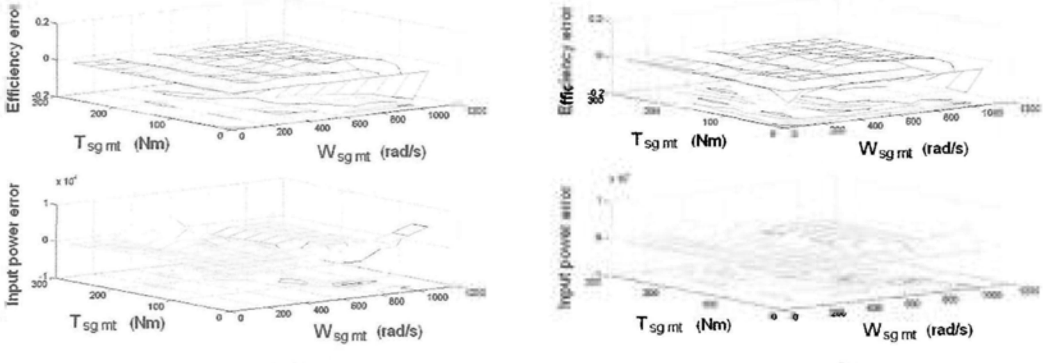

(a) Interpolation 1

(b) Interpolation 2

Figure 3.4: Interpolation Error Comparison

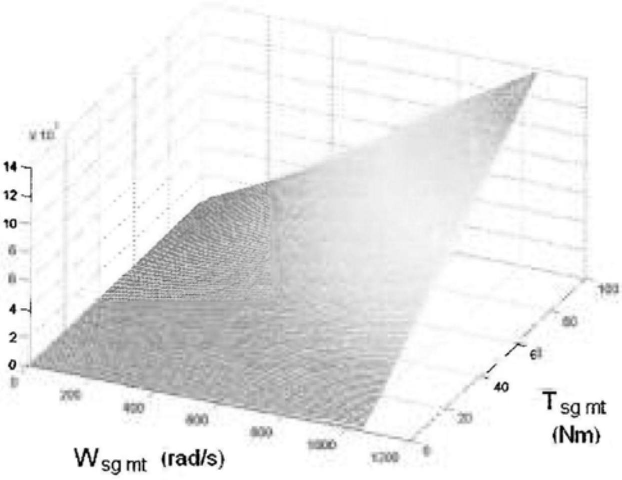

Figure 3.5: Input power map after Refinement

3.4 Real-time Optimal Torque Distribution

The aim of torque distribution is to obtain the proportion of front and rear wheel torques in real-time when total torque is known to ascertain the lowest total input power, or in other words, to achieve the highest level of energy efficiency. For real-time performance, it is practical to compute the layers of input power or energy efficiency spanned by the front motor torque and the rear motor torque offline.

In this tradeoff, the optimization process is broken down into two steps: 1) offline computation of the matrix minimal input power $P_{OTD}(\omega_{wh}, T_{Total})$ for each T_{Total}. The torque distribution rules for each T_{Total} at the speed of ω_{wh} is stored in $\lambda_{OTD}(\omega_{wh}, T_{Total})$; 2) online retrieval of λ for the driving cycle.

For each ω_{wh} and for the lines of grids intersected by the hypotenuse line indicating the same $T_1 + T_2$ (same T_{Total} as well), there will be a minimal total input power $P_{OTD}(\omega_{wh}, T_{Total})$. Due to the symmetry of the matrix, if the minimum is not located in the central diagonal ($T1 = T2$), there will be at least two minima, i.e. two or more minima. Here, only the one in the upper triangular matrix is selected.

The overall efficiency matrix spanned by T_1 and T_2 can then be computed according to Figure 3.6.

For ease of observation, Figure 3.7 shows the layers of the efficiency map rather than the layers of the input power map for various ω_{wh}.

The blue stars on the map indicate the maximal efficiency points for a specific wheel speed ω_{wh} with a T_{Total} that is a line $T_1+T_2 = T_{Total}$. From the

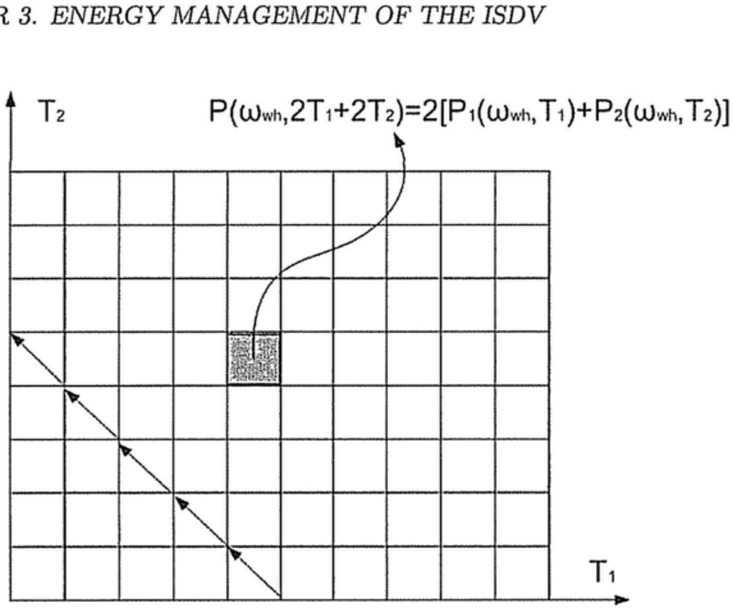

Figure 3.6: Input power matrix spanned by T1 and T2

evolution of the efficiency map with respect to ω_{wh}, it can be observed that the overall layer of the efficiency map increases from (a) to (d). Thereafter, from (d) to (g), efficiency in the small T_1 and T_2 regions remains high, while efficiency falls in the other regions. Two apparently convex lines appear, and due to the symmetry described by $T_1 = T_2$, one of them is selected as the maximal efficiency line.

From (a) to (d), OTD is almost consistent and maintains an even distribution (ED). Although there are different points not located in the diagonal line $T_1 = T_2$, the flatness of the efficiency map, i.e. its low gradient, reduces the difference between them. In the small T_{Total} region, OTD is equal to ED, a phenomenon that is independent of ω_{wh}. However, in (f) and (g), the visible difference still makes OTD better than ED.

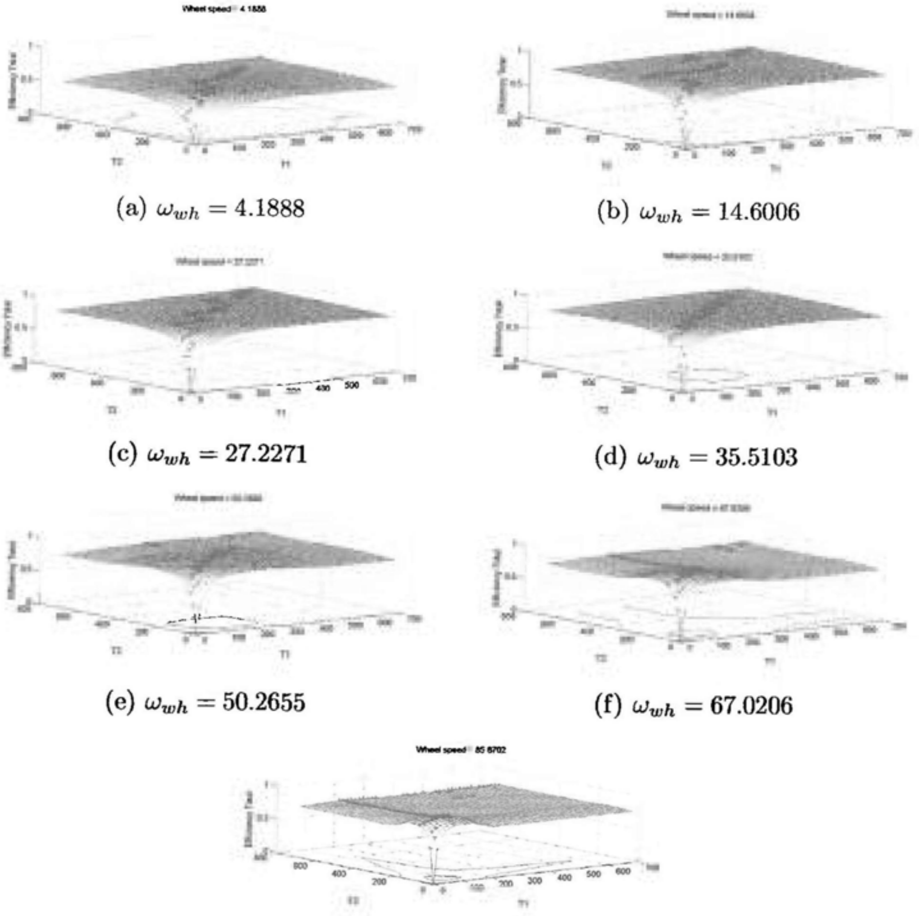

(a) $\omega_{wh} = 4.1888$

(b) $\omega_{wh} = 14.6006$

(c) $\omega_{wh} = 27.2271$

(d) $\omega_{wh} = 35.5103$

(e) $\omega_{wh} = 50.2655$

(f) $\omega_{wh} = 67.0206$

(g) $\omega_{wh} = 85.8702$

Figure 3.7: Layers of efficiency matrix spanned by T1 and T2 in different wheel speed

3.5 Overall Efficiency Map

For a specific α, the overall efficiency maps derived by OTD and ED can be computed offline.

The charts in sub-figures (a), (c), and (e) compare the overall efficiency maps (upper) and the input power maps (lower) for a 4WID ED and a single motor EV with various scaling factors α. With an increase in α (towards $1/\zeta$), the relatively high efficiency zone of ED in comparison with that of a single motor EV results in a shift from the low speed and large torque region to the high speed and low torque region. When $\alpha = 1/\zeta$, the efficiency difference seems to be mainly due to gearbox efficiency and all the other parts of the efficiency map are flat. Some parts in (a) and (c) have a negative efficiency difference, indicating the negative effect of a small α. Although a small alpha increases efficiency in some parts of the map, it decreases efficiency in the others. It is necessary to consider this pattern based on different cycles to drive the vehicle in such a way that more operational points are located in the high efficiency region.

To compare OTD and ED, the right hand column of Figure 3.8 illustrates the comparison of the input power map and the efficiency map derived by each strategy. It can be seen that there is a mountain-like convex shape in both the efficiency difference map and the input power difference map. The "mountains" are located in the high speed and high torque region and shift from the upper left zone to the lower right zone. Clearly, OTD is more efficient than ED. Although the efficiency improvement is small, peaking at about 5%, it will still be valuable once the number of EVs and the driving

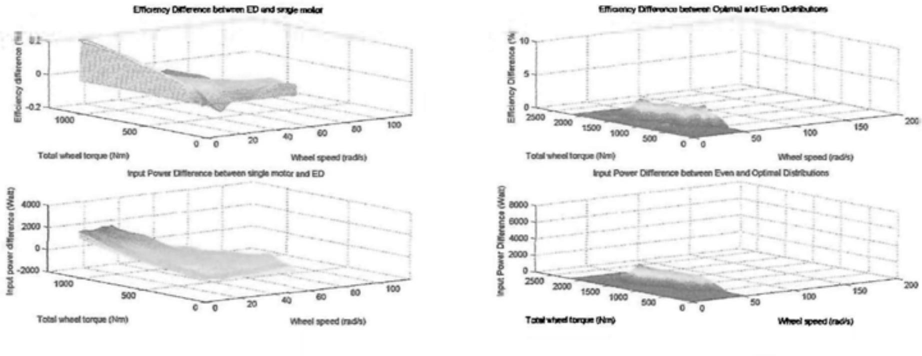

(a) $\alpha = 0.050$ (b) $\alpha = 0.050$

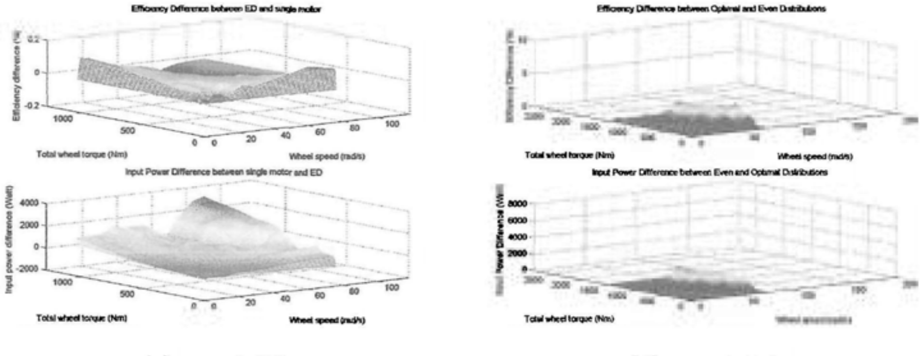

(c) $\alpha \approx 0.072$ (d) $\alpha \approx 0.072$

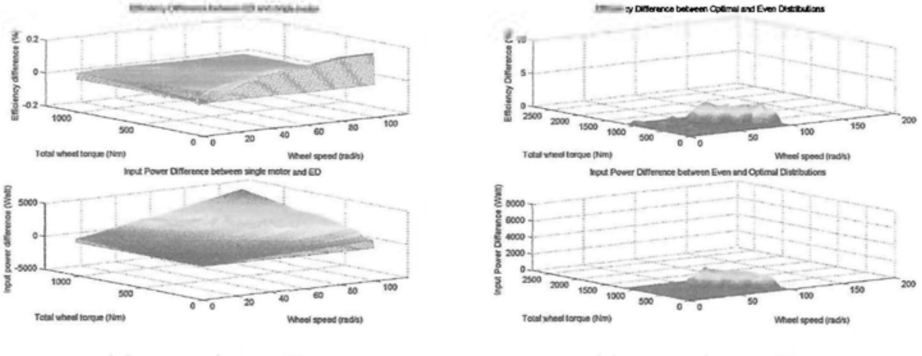

(e) $\alpha = 1/\zeta \approx 0.094$ (f) $\alpha = 1/\zeta \approx 0.094$

Figure 3.8: Overall efficiency map and input power comparison

distance increase.

Computing optimal torque distribution for one α on a PC with an Intel Pentium 4 CPU 3.06GHz and 504 MB RAM takes about 19.5 seconds. The total size of the efficiency map is 162 KByte. The cost of space reduces the time cost that limits the real-time application of such maps in vehicles.

3.6 Driving Cycle Analysis

I test a low-speed driving cycle (the Manhattan Cycle) and a high-speed driving cycle (the HWYFET Cycle). The Manhattan Cycle is for buses driven in a crowded part of Manhattan, although it is also suitable for other crowded cities such as Hong Kong. However, the gradients of Hong Kong roads are steeper. Hence, the Manhattan Cycle is modified by adding the 12% road gradient commonly found in Hong Kong.

Because motor regenerative braking is a separate and somewhat complicated topic not covered by this thesis, I simulate and analyze only motor discharging power.

Figure 3.9 illustrates the percentage of fuel saved by OTD and ED in comparison with a single motor EV. The percentage of fuel saved drops from approximately 26% to 16% as α increases from 0.05 to $1/\zeta$.

Figure 3.10 shows the simulation results. From (b), it can be seen that OTD performs better than the single motor EV in all discharging periods. The Manhattan cycle on a slope includes a large number of sudden accelerations that result in operational points with a low speed and a large torque. As a result, the single motor has to consume a large amount of input power at

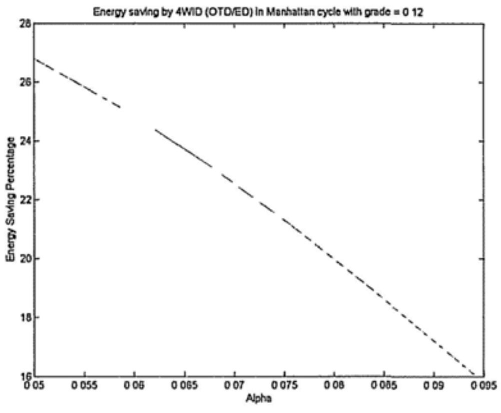

Figure 3.9: Input power saving percentage with various α in Manhattan Cycle (grade = 12%)

a low level of efficiency. In comparison, in-wheel motors with a small scaling factor α can filter out such power shocks by working in a higher efficiency region. The histogram clearly shows the relative efficiency rates, i.e. η_S/η_{OTD}, for each operational point. Part (d) of the figure confirms that OTD performs better than a single motor EV at a low speed with high torque. It can also be seen that there are some small regions with contours marked 0.98 in which 4WID OTD has a negative effect. ED and OTD perform at the same level in this driving cycle because no operational points fall into the high speed and high torque region.

Figure 3.11 shows the simulation results for the US EPA highway fuel economy certification test (HWYFET) with road grade 0. Because the cycle speed reaches the approximated maximal speed of the designed EV, there is not much space for α and $\alpha = 1/\zeta$ to adjust. The operational points mainly fall in the region where the efficiency of the single motor EV is reduced by the transmission as the torque is low. These test results therefore indicate

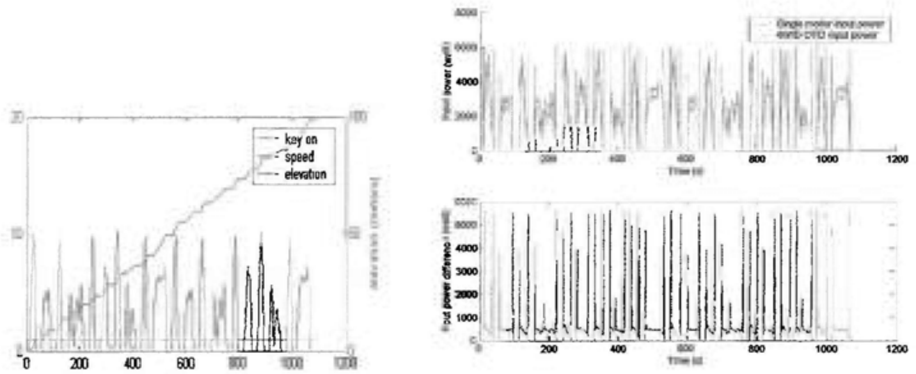

(a) Manhattan Cycle with grade 12% (b) Input power and input power difference

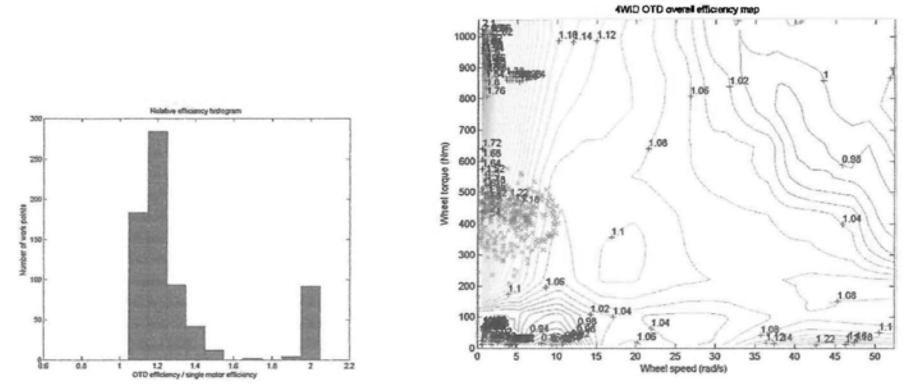

(c) Operational points histogram (d) Operational point distribution in relative efficiency map by OTD

Figure 3.10: Manhattan Cycle (grade=12%) simulation results

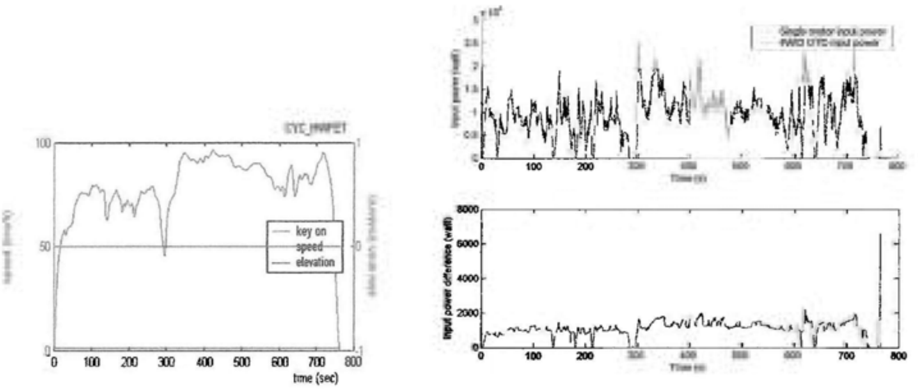

(a) HWYFET Cycle with grade 0 (b) Input power and input power difference

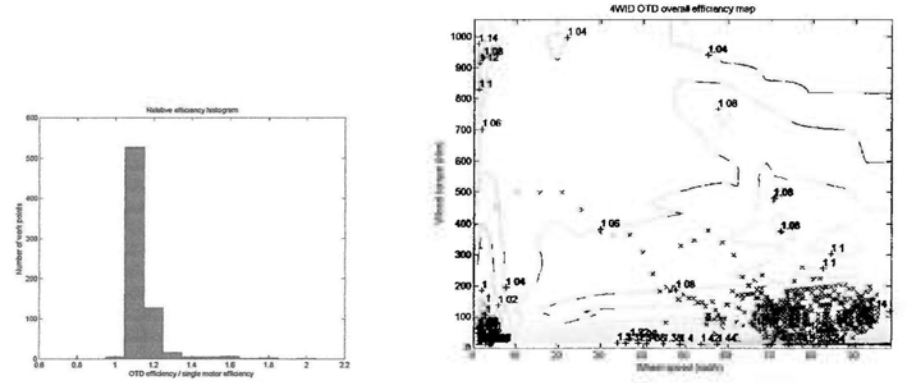

(c) Operational points histogram (d) Operational point distribution in relative efficiency map by OTD

Figure 3.11: HWYFET Cycle (grade=0) simulation results

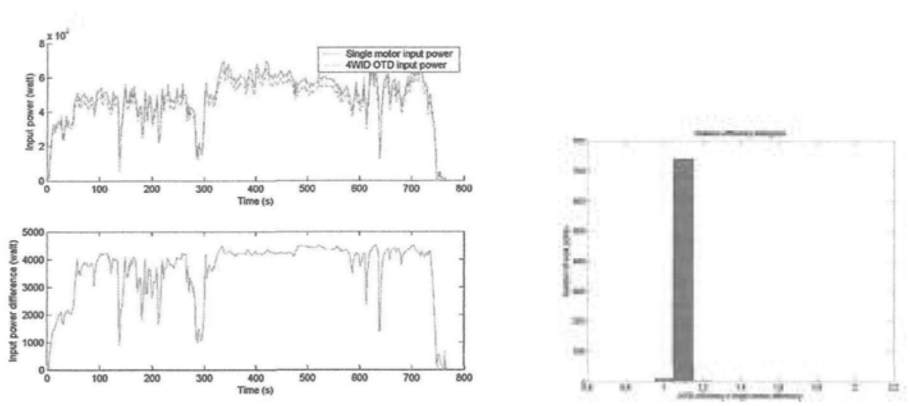

(a) Input power and input power difference (b) Operational points histogram

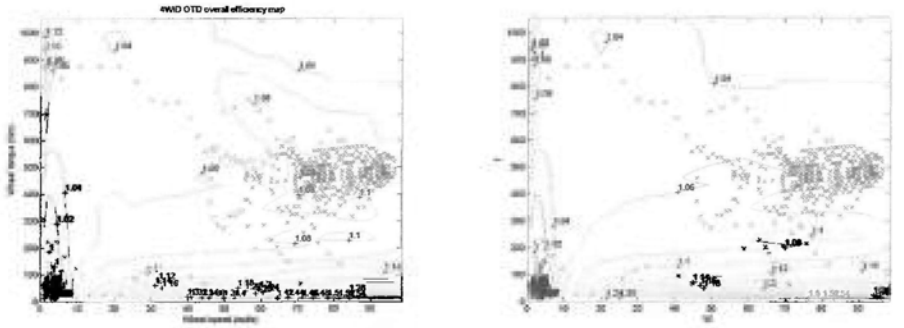

(c) Operational point distribution in relative efficiency map by OTD (d) Operational point distribution in relative efficiency map by ED

Figure 3.12: HWYFET Cycle (grade=12%) simulation results

that 4WID is more efficient than the single motor EV, while OTD and ED perform at the same level.

Figure 3.12 shows that in the high-speed zone, an increase in torque improves the performance of the single motor EV and moves it closer to that of the 4WID configuration, and also lead to improved transmission efficiency. However, a performance difference between OTD and ED appears as the torque increases.

Table 3.2 summarizes the simulation results. The 4WID configuration

Table 3.2: Simulation results for energy efficiency

Cycle	Grade (%)	α	Type	Discharge Energy (kJ)	Saved Energy Percentage (%)	Saved Energy Amount (kJ)
Manhattan	12	0.050	SGM	2209	–	–
			OTD	1617	26.8	592
			ED	1617	26.8	592
		≈ 0.072	SGM	2209	–	–
			OTD	1722	22.1	487
			ED	1722	22.1	487
		$1/\zeta \approx 0.094$	SGM	2209	–	–
			OTD	1854	16.1	355
			ED	1854	16.1	355
HWYFET	0	$1/\zeta \approx 0.094$	SGM	7467	–	–
			OTD	6627	11.2	840
			ED	6627	11.2	840
	12		SGM	37486	–	–
			OTD	34686	7.5	2800
			ED	35468	5.4	2018

in the ISDV can save more energy than a traditional single motor vehicle. Moreover, when its motors work in the high speed and high torque region, the OTD strategy will have the effect of saving even more energy in comparison with the ED strategy.

3.7 Summary

This chapter further explores the 4WID configuration of the ISDV by adjusting torque distribution to increase energy efficiency. 2D interpolation for map refinement is first explored, revealing that grid refinement is more accurate in the motor input power map than in the motor efficiency map. The chapter then examines the OTD strategy involving offline overall efficiency map rendering and online retrieval. Simulations validate the superior performance of the OTD strategy in comparison with the traditional single motor EV in low-speed and large-torque, high-speed and low-torque, and high-speed and large-torque cycles.

Chapter 4

Parking Analysis of the Independent Steering and Driving Vehicle

4.1 Introduction

With the increase in the number of vehicles in urban areas, parking has become a significant problem in the design and development of cities. It is a universal challenge for drivers to find a parking slot or even to park their vehicle in the slot when they eventually find one.

In traditional parking lot design, [12] [19] [20] [21] [22], the vehicle has to be driven manually to navigate around the car park and find a parking slot. It is also necessary to set aside a significant amount of space to allow the driver to maneuver the moving vehicle

Research and development work has been undertaken on fully automatic parking garages as an alternative parking solution Studies conducted to date include those of Stolzer Parkhaus [13], Perfect Park [14], Klaus Multiparking [15], LTW [16], and Smart Parking [17]. These systems are based on the concept of the assembly line and require sophisticated steel frames Moreover, because vehicles are parked in series, parking time is subject to bottlenecks that preclude their adoption in crowded conditions Another aspect to consider is that cost will become an issue if a parallel processing line is manufactured. It is also difficult to modify the scale of the car park once construction is complete

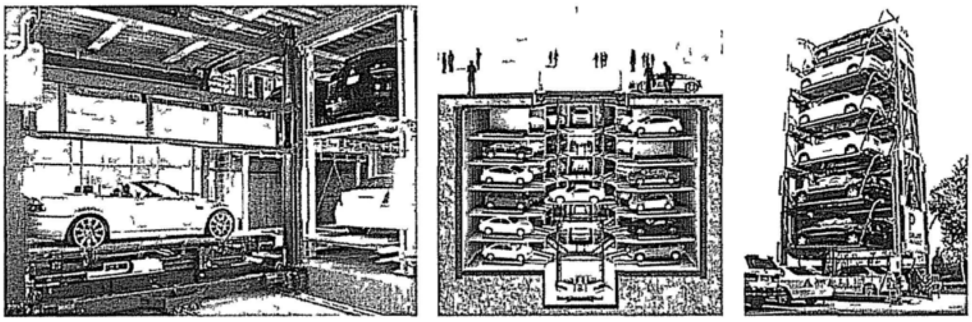

(a) Stolzer Parkhaus (b) Perfect Park (c) Smart Parking

Figure 4 1 Examples of current automatic parking structures

To overcome the problems of traditional manned parking lots and fully automated parking frame systems, the use of wheeled mobile robots that function as mobile platforms by carrying vehicles to their parking destination has also been explored These robots can then unload/load vehicles to park/retrieve them for customers One problem inevitably encountered in this type of design is mobile robot path planning There is a rich literature on automatic navigation and parking. Murray [25] used sinusoids to manipulate a car-like robot confined by nonholonomic constraints. Paromtchik [27] [28] designed parallel parking controls in a platform named LIGIER. Lo [29]and Chao [24] maneuvered vehicles based on the combination of two circular trajectories. Fraichard [2] and *Müller* [26] investigated continuous curvature paths for vehicle parking. These studies focus on trajectory and motion generation based on a predetermined parking environment. However, to ensure the civil development of society, it is necessary to study how to park the same amount of vehicles in a smaller parking space, i.e. to design parking lots that save space. Moreover, investigation of which mobile robot structure delivers a higher level of space efficiency-the ratio of parking space to total parking and traveling space-is also inevitable.

The nonholonomic constraints in car-like robots result from the fact that their four wheels cannot be steered independently of each other, making the rotation and translation of car-like robots dependent on each other, which in turn precludes any further increase in space efficiency. In contrast, the use of an omnidirectional structure-four-wheel independent steering (4WIS)-removes the dependence between translation and rotation of the robot and therefore facilitates subtle changes in either translation or rotation to enhance the mobility of the robot and allow for vehicles to be parked in a limited space.

This chapter analyzes two aspects in parking, i.e. space and time. For traditional front-wheel-steering vehicles, a method inspired by computer vision is proposed to compute the maximal space efficiency based on steering by continuous curvature. As comparisons, omni-directional parking based on ZRT and freely omni-directional motions, are also analyzed. In the aspect of time, a human-in-loop experiment is designed to test the performances of the ISDV and traditional front-wheel-steering vehicles.

4.2 Space Analysis of Parking

4.2.1 Parking Based on Front-wheel-steering Motion

Modeling of Vehicle Trajectory

The front-wheel-steering is the same as the motion of a traditional vehicle, which can generally be expressed by a single track model that satisfies the constraints in equation 4.1.

$$\begin{bmatrix} \frac{dx_c}{dt} \\ \frac{dy_c}{dt} \\ \frac{d\theta}{dt} \\ \frac{d\kappa}{dt} \end{bmatrix} = \begin{bmatrix} \cos(\theta) \\ \sin(\theta) \\ \kappa \\ 0 \end{bmatrix} v(t) + \begin{bmatrix} 0 \\ 0 \\ 0 \\ 1 \end{bmatrix} \sigma(t) \tag{4.1}$$

where (x_c, y_c) is the coordinate of the center of virtual wheel, $\kappa = \frac{tan(\phi)}{L_b}$, and $\sigma = \frac{1}{Lcos^2(\phi)}\omega(t)$.

Fraichard and Scheuer [2] proposed the continuous curvature (CC) steering for motion of front-wheel-steering vehicles. They assumed vehicle velocity to be constant for the entire trajectory, that is .

$$\frac{ds}{dt} = v_0 \tag{4.2}$$

where s is the curve distance in the trajectory, and v_0 is the constant velocity at the $(x_c(t), y_c(t))$.

Equation 4.1, can then be derived to obtain

$$\begin{bmatrix} \frac{dx_c}{ds} \\ \frac{dy_c}{ds} \\ \frac{d\theta}{ds} \\ \frac{d\kappa}{ds} \end{bmatrix} = \begin{bmatrix} \cos(\theta) \\ \sin(\theta) \\ \kappa \\ 0 \end{bmatrix} + \begin{bmatrix} 0 \\ 0 \\ 0 \\ 1 \end{bmatrix} \frac{\sigma}{v_0} \tag{4.3}$$

The driver's steering manipulation is divided into three stages:

1. Increase the curvature κ from zero to the maximum $\kappa_{max} = \frac{tan(\phi_{max})}{L_b}$ in time interval $[t_0, t_0 + \Delta t]$ at a constant rate $\frac{\kappa_{max}}{\Delta t}$;
2. Keep the angle at κ_{max} in the time interval $[t_0 + \Delta t, t_1 - \Delta t]$;
3. Reduce the angle from ϕ_{max} to zero in the time interval $[t_1 - \Delta t, t_1]$ at a constant rate $-\frac{\kappa_{max}}{\Delta t}$.

The steering wheel-related control is denoted by

$$\sigma(t) = \begin{cases} \frac{\kappa_{max}}{\Delta t} v_0 & t \in [t_0, t_0 + \Delta t] \\ 0 & t \in (t_0 + \Delta t, t_1 - \Delta t] \\ -\frac{\kappa_{max}}{\Delta t} v_0 & t \in (t_1 - \Delta t, t_1] \end{cases} .$$

Due to the constant velocity over time, the horizontal axis for time can be replaced by a distance axis with linear transformation $s = v_0 t$.

In each of the three stages, the CC curve can be obtained by integration as shown below.

1. Turning from neutral position,i.e. $s \in [v_0 t_0, v_0(t_0 + \Delta t)]$:

$$\begin{cases} \kappa(s) = \frac{\sigma}{v_0} s \\ \theta(s) = \frac{\sigma}{2v_0} s^2 \\ x_c(s) = \sqrt{\frac{\pi v_0}{\sigma}} C_f(\sqrt{\frac{\sigma}{\pi v_0}} s) \\ y_c(s) = \sqrt{\frac{\pi v_0}{\sigma}} S_f(\sqrt{\frac{\sigma}{\pi v_0}} s) \end{cases} \tag{4.4}$$

2. Maintaining the steering angle, i.e. $s \in (v_0(t_0 + \Delta t), v_0(t_1 - \Delta t)]$:

$$\begin{cases} \kappa(s) = \kappa_{\max} \\ \theta(s) = \kappa_{\max} - \frac{\kappa_{\max}^2 v_0}{2\sigma} \\ x_c(s) = \frac{1}{\kappa_{\max}} \left[\sin(\kappa_{\max}(s - s_1) + \theta_1) - \sin(\theta_1)\right] + x_c(s_1) \\ y_c(s) = \frac{1}{\kappa_{\max}} \left[\cos(\theta_1) - \cos(\kappa_{\max}(s - s_1) + \theta_1)\right] + y_c(s_1) \end{cases} \tag{4.5}$$

where $\kappa_{\max} = \frac{\sigma}{v_0}\Delta t$, $s_1 = v_0(t_0 + \Delta t)$, $\theta_1 = \frac{\kappa_{\max} s_1}{2}$, $x_c(s_1)$ and $y_c(s_1)$ are computed based on equation 4.4.

3. Turning back to neutral position,i.e. $s \in (v_0(t_1 - \Delta t), v_0 t_1]$:

$$\begin{cases} \kappa(s) = \kappa_{\max} - \frac{\sigma}{v_0}(s - s_2) \\ \theta(s) = \theta(s_2) - \frac{\sigma}{2v_0} s^2 + \frac{\sigma}{2v_0} s_2^2 + (\kappa_{\max} + \frac{\sigma}{v_0} s_2)(s - s_2) \\ x(s) = x(s_2) - \sqrt{\frac{\pi v_0}{\sigma}} \left[S_f\left(-\sqrt{\frac{\sigma}{\pi v_0}} s + \sqrt{\frac{v_0}{\pi\sigma}}\kappa_{\max} + \frac{1}{2\kappa_{\max}}\sqrt{\frac{\pi\sigma}{v_0}}\right) - S_f\left(\sqrt{\frac{v_0}{\pi\sigma}}\kappa_{\max}\right)\right] \\ y(s) = y(s_2) + \sqrt{\frac{\pi v_0}{\sigma}} \left[C_f\left(\sqrt{\frac{\sigma}{\pi v_0}} s - \sqrt{\frac{v_0}{\pi\sigma}}\kappa_{\max} - \frac{1}{2\kappa_{\max}}\sqrt{\frac{\pi\sigma}{v_0}}\right) - C_f\left(\sqrt{\frac{v_0}{\pi\sigma}}\kappa_{\max}\right)\right] \end{cases} \tag{4.6}$$

where $s_2 = v_0(t_1 - \Delta t)$, $\theta(s_2)$, $x_c(s_2)$ and $y_c(s_2)$ are computed based on the analytical equations in 4.5.

The aforementioned equations include two key mathematic functions that require further elaboration. $C_f(\cdot)$ and $S_f(\cdot)$ are Fresnel integrals.

$$\begin{cases} S_f(x) = \int\limits_0^x \sin\left(\frac{\pi}{2}t^2\right)dt \\ C_f(x) = \int\limits_0^x \cos\left(\frac{\pi}{2}t^2\right)dt \end{cases} \tag{4.7}$$

This can be numerically computed by

$$\begin{cases} S_f(x) = \sqrt{\frac{2}{\pi}} \sum\limits_{n=0}^{\infty} (-1)^n \frac{\left(\sqrt{\frac{\pi}{2}}x\right)^{4n+3}}{(2n+1)!(4n+3)} \\ C_f(x) = \sqrt{\frac{2}{\pi}} \sum\limits_{n=0}^{\infty} (-1)^n \frac{\left(\sqrt{\frac{\pi}{2}}x\right)^{4n+1}}{(2n)!(4n+1)} \end{cases} \tag{4.8}$$

Matlab has provided the maple callback function for computation of the two Fresnel integrals. This step can be conducted offline to save on computational costs incurred in trajectory generation. Figure 4.2 displays the Fresnel functions computed offline.

Modeling of Vehicle Contour

Although many studies in the robotics literature have provided vehicle trajectory models, few have explored the most important problem in vehicle motion planning for a crowded environment: the space contour swept by the vehicle body. This section goes a step further by modeling the vehicle contour to facilitate more detailed analysis of the space within which the vehicle moves.

To analyze the contour curve of the area that the vehicle body swipe, I

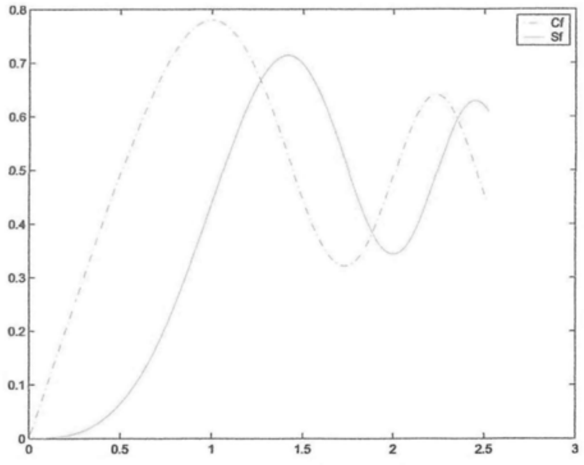

Figure 4.2: Fresnel functions

proposed a numeric method inspired by computer vision, in which the 2D plane is discretized first into an array of pixels.

One important factor in discretization via this numeric method is the pixel size mapped into the real 2D Euclidian space. Figure 4.3 reproduces the vehicle state space configuration. It is reasonable to adopt the same pixel size $(\delta x, \delta y)$ for the two axes, $\overrightarrow{OX}$ and $\overrightarrow{OY}$, i.e. $\delta x = \delta y$

Two criteria should be considered to determine $(\delta x, \delta y)$, i.e.

1. **Precision**: Because all the position points within the pixel will be considered to be points at the center of the pixel, the finer the pixel, the greater the degree of precision.

2. **Computational cost**: Because the image size increases proportional to $\frac{1}{\delta x^2}$, the memory required will be inversely proportional to δx^2. Moreover, the computational time will also increase when the grid becomes more refined.

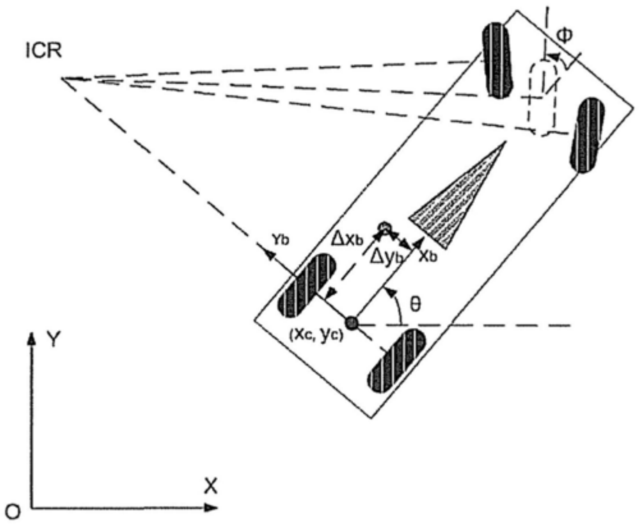

Figure 4.3: Traditional front-wheel-steering vehicle state

Muller proposed a computational approach to visualize the area occupied in the parking process [26] in which a series of rectangles are plotted to show the trajectory of the vehicle body. Nevertheless, this approach is computationally expensive and time-consuming. Moreover, the contour of the occupied area is not continuous. Considering that the only information required is the contour of the space occupied by the vehicle, the trajectories of several extreme points and the edges of the initial and final states are sufficient.

In Figure 4.3, the position of an arbitrary point $(\Delta x_b, \Delta y_b)$ on the vehicle body in the vehicle inertia coordinate frame $X_b O_b Y_b$ can be expressed as

$$\begin{cases} x_P = x_c + \Delta x_b \cos(\theta) + \Delta y_b \cos\left(\theta + \frac{\pi}{2}\right) \\ y_P = y_c + \Delta x_b \sin(\theta) + \Delta y_b \sin\left(\theta + \frac{\pi}{2}\right) \end{cases} \tag{4.9}$$

Thus, after computation of x_c, y_c, and θ in equations 4.4-4.6, the trajectories of arbitrary points in the vehicle body can be obtained.

Contour Connectivity

One basic constraint applicable to contour rendering is that the rendered contour should be a connected curve. When the pixel dimension, i.e. (δ, δ), is large, this will not be a major problem. However, the drawback of a large pixel size is less precision. When the dimensions of the pixel are small, sampling at s should be considered in more detail to guarantee the connectivity of the contour.

By differentiating equation 4.9 with respect to t, we obtain

$$\begin{cases} \frac{dx_p}{dt} = v_0 \cos\theta - \left[\Delta x_b \sin\theta + \Delta y_b \sin\left(\theta + \frac{\pi}{2}\right)\right] \kappa v_0 \\ \frac{dy_p}{dt} = v_0 \sin\theta + \left[\Delta x_b \cos\theta + \Delta y_b \cos\left(\theta + \frac{\pi}{2}\right)\right] \kappa v_0 \end{cases} \tag{4.10}$$

Taking into consideration of $\frac{ds}{dt} = v_0$,

$$\begin{cases} dx_p = \left\{\cos\theta - \left[\Delta x_b \sin\theta + \Delta y_b \sin\left(\theta + \frac{\pi}{2}\right)\right] \kappa\right\} ds \\ dy_p = \left\{\sin\theta + \left[\Delta x_b \cos\theta + \Delta y_b \cos\left(\theta + \frac{\pi}{2}\right)\right] \kappa\right\} ds \end{cases} \tag{4.11}$$

To assess connectivity, the eight-connected neighborhood shown in Figure 4.4 is adopted in which each pixel (i, j) is connected to the eight adjacent pixel neighbors, i.e. $(i \pm 1, j \pm 1)$. The following figure illustrates this concept.

Hence, a connected contour requires that $\forall s_i \in [0, v_0 t_f]$,

$$\begin{cases} |dx_p| \le \delta \\ |dy_p| \le \delta \end{cases} \tag{4.12}$$

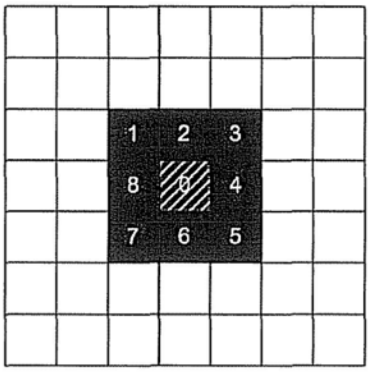

Figure 4.4: Eight-connected neighborhood

Substitute equation 4.11 into inequality 4.12,

$$\begin{cases} |ds| \leq \frac{\delta}{\left|\cos\theta - \left[\Delta x_b \sin\theta + \Delta y_b \sin\left(\theta + \frac{\pi}{2}\right)\right]\kappa\right|} \\ |ds| \leq \frac{\delta}{\left|\sin\theta - \left[\Delta x_b \cos\theta + \Delta y_b \cos\left(\theta + \frac{\pi}{2}\right)\right]\kappa\right|} \end{cases} \tag{4.13}$$

Hence the discretization step of s is

$$\delta_s = \frac{\delta}{\max(|g_{xi}(s)|, |g_{yi}(s)|)} \tag{4.14}$$

where

$$\begin{cases} g_{xi}(s) = \cos\theta(s) - \left[\Delta x_b \sin\theta(s) + \Delta y_b \sin\left(\theta(s) + \frac{\pi}{2}\right)\right]\kappa(s) \\ g_{yi}(s) = \sin\theta(s) + \left[\Delta x_b \cos\theta(s) + \Delta y_b \cos\left(\theta(s) + \frac{\pi}{2}\right)\right]\kappa(s) \end{cases} \tag{4.15}$$

Because $\Delta x_b \in [-b, L-b]$ and $\Delta y_b \in [-\frac{W}{2}, \frac{W}{2}]$ are independent on each other, the relationship of $|g_{xi}|$ with respect to either Δx_b or Δy_b is either a line or a continuous convex broken line. Thus its maximum is at one of the four points $(-b, -\frac{W}{2})$, $(-b, \frac{W}{2})$, $(L-b, -\frac{W}{2})$, and $(L-b, \frac{W}{2})$. It is the same for the maximum of $|g_{yi}|$.

Computational Algorithm

Figure 4.5 below summarizes the the flowchart of the computational algorithm.

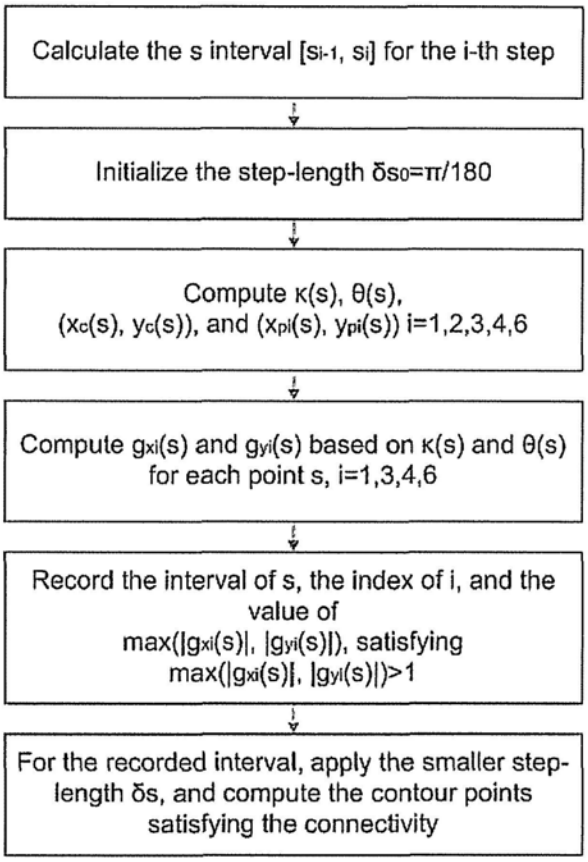

Figure 4.5: Connectivity refinement flow chart

There are three steps in the overall interval $s \in [0, v_0 t_f]$. $\kappa(s)$, $\theta(s)$, $x_c(s)$, and $y_c(s)$ are calculated according to the equations derived in these three steps.

Figure 4.6 visualizes the g_{xi} and g_{yi}, $(i = 1, 3, 4, 6)$ over the s in the case of backward motion with $b = 1.10m$, $r_{min} = 1.91m$, $\Delta t = 5sec$. Figure 4.7

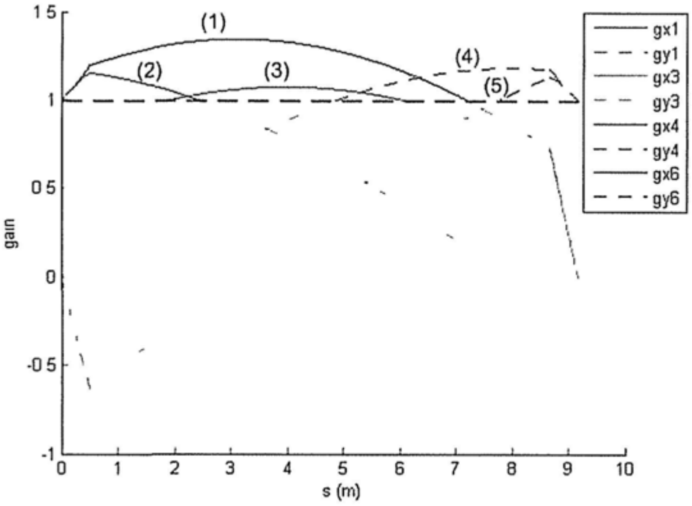

Figure 4.6: An example of gain

shows the broken contour for the situation.

There are 5 parts with an absolute gain of greater than 1. Parts (1), (2), and (3) result in a broken contour in the x direction, and parts (4) and (5) correspond to the broken contour in the y direction. The gaps are all filled after δs is refined.

As a result, for any Δt, there will be one image for the contour showing the trajectories of P_i ($i = 1, 2, 3, 4, 6$) and the initial and final boundaries for the sake of contour detection. The trajectory of the center point in the rear axis is also plotted for reference.

Slot Arrangement

In the parking manipulation by front-wheel-steering motion, aside of CC steering to change to the final altitude, the driver will also undertake straight translational motion if the longitudinal state has not reach the final position.

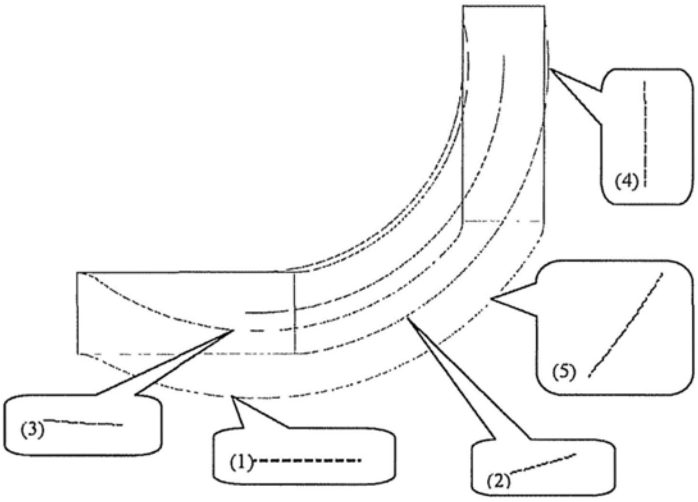

Figure 4.7: Trajectory with broken contour

These complicated manipulations pose a tremendous challenge for analytic or geometric methods. I therefore analyze the parking contour numerically.

The width of the aisle and the width of the slot for each contour figure are determined by using another variable d_f, i.e. the final straight distance the vehicle has to travel before it reaches its final position.

As shown in Figure 4.8, five key points on the contour are used to determine slot width and aisle width.

1. P_r: The rightmost point.
2. P_d: The downmost point.
3. P_t: The topmost point.
4. P_{s1}: The left intersection point by the upper aisle boundary and the contour.

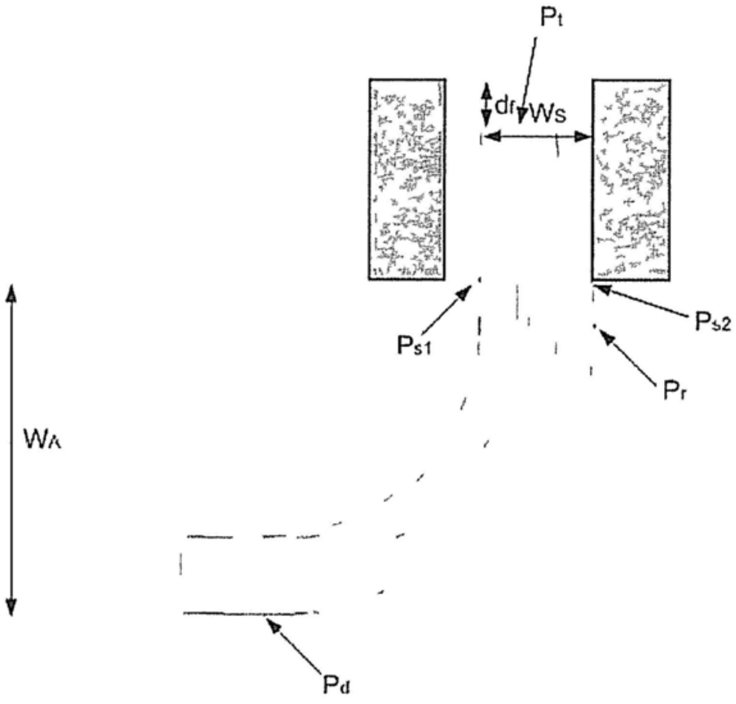

Figure 4.8 Slot-aisle arrangement on CC contour with d_f

5 P_{s2}· The right intersection point by the upper aisle boundary and the contour.

Due to the connectivity of contours, all five key points in the contour image can be determined Determination of the slot width and the aisle width is illustrated in the flowchart in Figure 4 9

The three key points of P_r, P_d and P_t are determined on the basis of the contour image for any parameterized driving behavior with Δt and d_f Thereafter, the lower aisle boundary location measured by pixels is determined on the basis of P_d by setting its discrete vertical coordinate according to

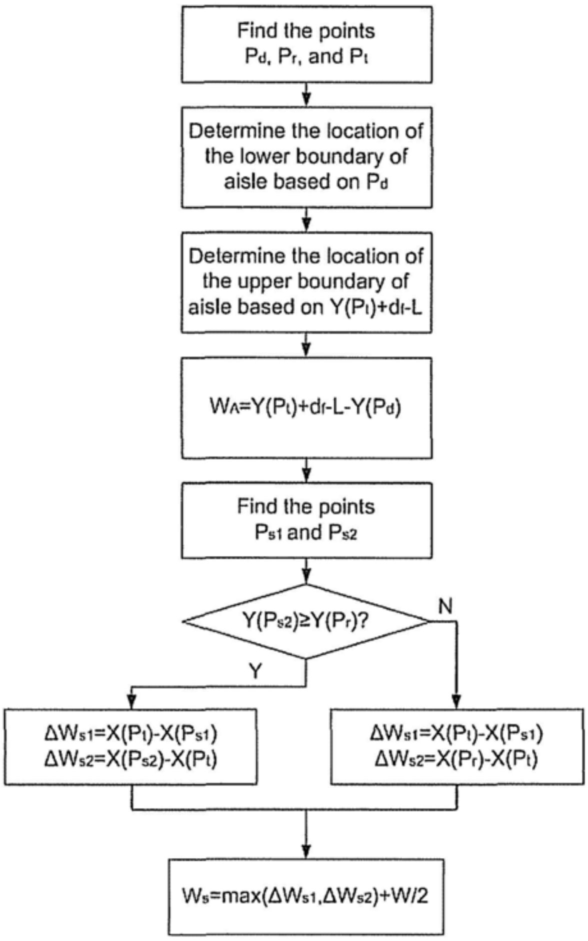

Figure 4.9: Flowchart of slot-aisle determination numerically

$$Y_{AisleLower} = Y(P_d) - 1 \tag{4.16}$$

The upper aisle boundary is determined by

$$Y_{AisleUpper} = Y(P_t) + ceiling((d_f - L)/\delta) \tag{4.17}$$

where $ceiling(x)$ is to find the integer satisfying $ceiling(x) - 1 < x \leq ceiling(x)$.

Thereafter, P_{s1} and P_{s2} can be determined on the basis of the upper aisle boundary. If $Y(P_{s2}) \geq Y(P_r)$, the rightmost points will not be included in the parking slot and thus will not play a role in expanding the slot width (the case in Figure 4.8). P_{s1} and P_{s2} are the two points determining the slot width. If $\Delta W_{s2} = X(P_{s2}) - X(P_t) > \Delta W_{s1} = X(P_t) - X(P_{s1})$, the vehicle will sweep a larger area in the right part of the vehicle, so $W_s = \Delta W_{s2} + \frac{W}{2}$. The left part of the vehicle will make use of the empty area in the left slot not occupied by the vehicle to the left.

If $\Delta W_{s2} = X(P_{s2}) - X(P_t) < \Delta W_{s1} = X(P_t) - X(P_{s1})$, $W_s = \Delta W_{s1} + \frac{W}{2}$. The right part of the vehicle will make use of the empty area in the right slot not occupied by the vehicle to the right.

The overall parameter space is three-dimensional and contains independent variables of the vehicle's structural parameters: the rear overhang b, and two driving behavioral parameters, i.e., CC steering time Δt and final straight line distance d_f. For each point in this parameter space, there will be one parking contour and one slot arrangement can be determined.

As seen from the previous section, there is an asymptotic space efficiency

Table 4.1: Structural parameters of the Toyota

Name	Symbol	Value (meter)
Length	L	4.82
Width	W	1.82
Wheelbase	L_b	2.78
Front overhang	a	0.95
Rear overhang	b	1.10

when the capacity of the parking lot reaches infinity. Denote this asymptotic space efficiency as $\tilde{\eta}_S$. Another subscript S or D is added to indicate single line parking or double line parking, i.e. $\tilde{\eta}_{SS}$ or $\tilde{\eta}_{SD}$.

The specifications of the Toyota Camry [18] are considered for numeric computation.

Figure 4.10 is the single line parking space efficiency cube in the 3D structure-behavior parameter space. The color bar on the right shows the space efficiency percentage. It should be noted that the rear overhang is no more than $\frac{L}{2}$. The region with $b > \frac{L}{2}$ represents cases in which the vehicle is reverse parked with a rear overhang of $L - b$. The red diamond denotes the behavioral parameter pair with maximal $\tilde{\eta}_{SS}$ for this b layer. The blue triangle represents the optimal behavioral parameter with $\Delta t = 0$. The black square denotes the optimal behavioral parameter with $d_f = 0$.

Figure 4.11 visually represents the isosurface of the space efficiency in the 3D parameter cube. When the $\tilde{\eta}_{SS}$ reaches about 40%, the length of the rear overhang should be the same as half of the vehicle's length. Moreover, in Figure , $\tilde{\eta}_{SS}$ is more sensitive to the behavioral parameter d_f than it is to Δt.

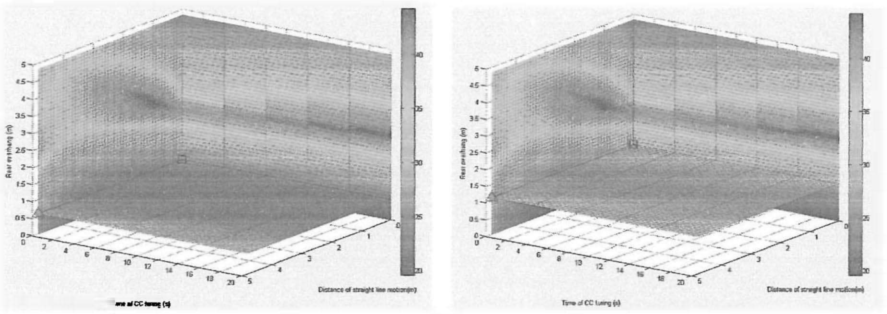

(a) b=0.60 (b) b=1.10

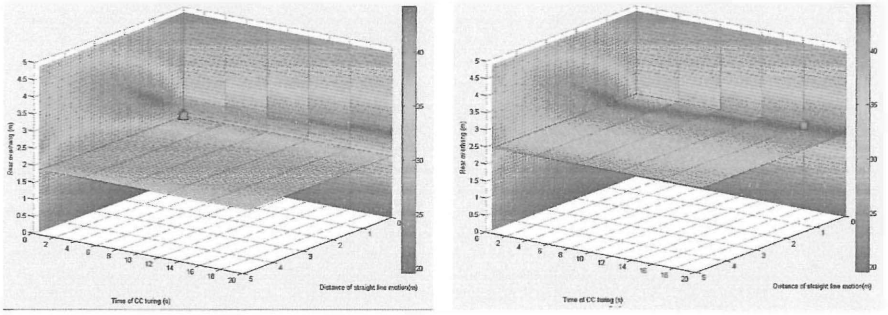

(c) b=1.81 (d) b=2.41

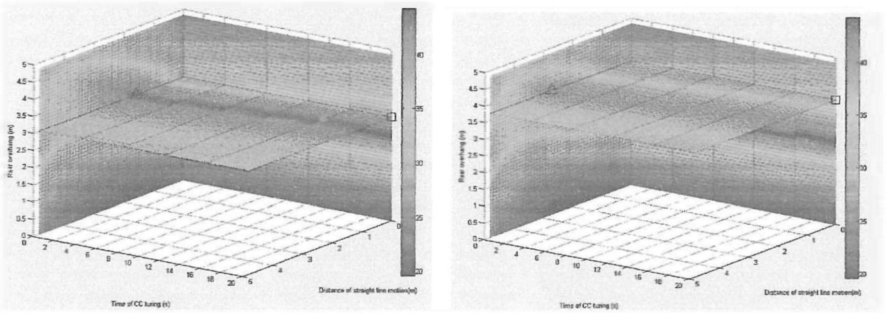

(e) b=3.02 (f) b=3.72

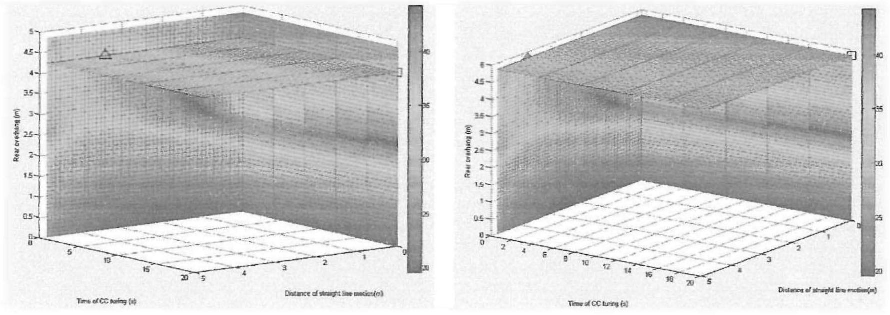

(g) b=4.22 (h) b=4.82

Figure 4.10: Efficiency evolution cube

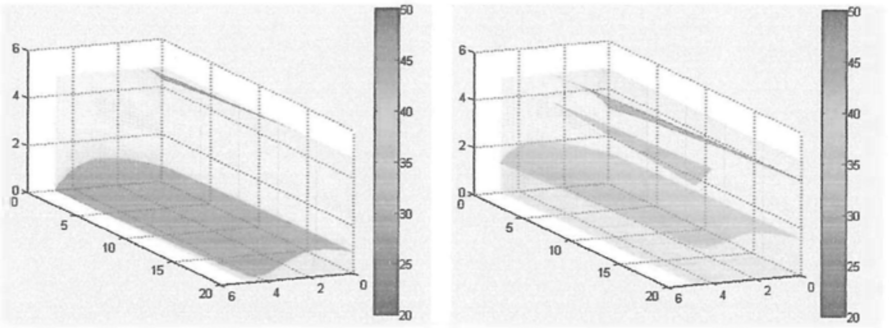

(a) $\tilde{\eta}_{SS} = 26\%$ (b) $\tilde{\eta}_{SS} = 32\%$

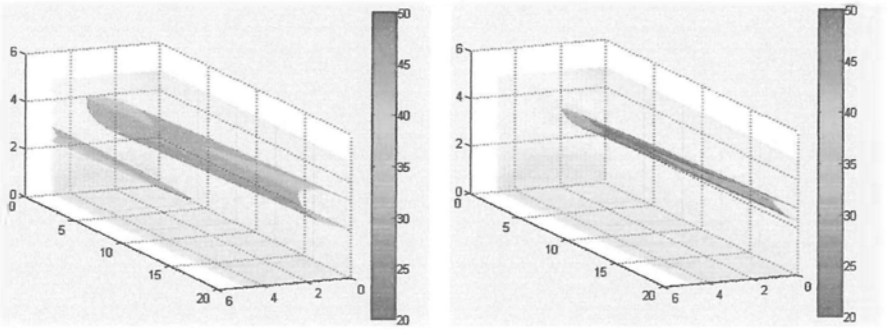

(c) $\tilde{\eta}_{SS} = 38\%$ (d) $\tilde{\eta}_{SS} = 42\%$

Figure 4.11: Isosurface in efficiency evolution cube

Figures 4.12 and 4.13 show the width of the slot and the width of the aisle in the 3D parameter space.

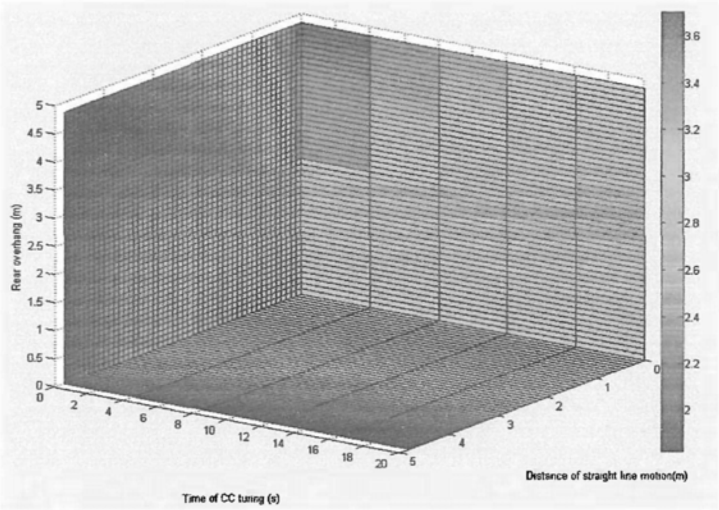

Figure 4.12: Slot width cube in the 3D parameter space

Figure 4.14 shows the maximized result for single line parking space efficiency in the 2D behavioral parameter for each structural parameter. The line circled in blue represents the space efficiency of R-S steering, the least efficient form of steering manipulation. It is as efficient as other forms of steering only in a small approximate interval of $b \in [1.3, 2.0]$.

In the forward parking scenarios, performing a CC-turn does not result in an increase in space efficiency, while final straight line translation will enhance $\tilde{\eta}_{SS}$. When the vehicle is parked in reverse, the appropriate CC steering, $\tilde{\eta}_{SS}$, can be increased by $5 - 10\%$, while an appropriate d_f will improve space efficiency even further by approximately 10%.

Figure 4.15 illustrates the structural-behavioral parameters at which space efficiency is maximized.

The most spatially efficient structure is b=2.41. When Δt =16 and d_f=0,

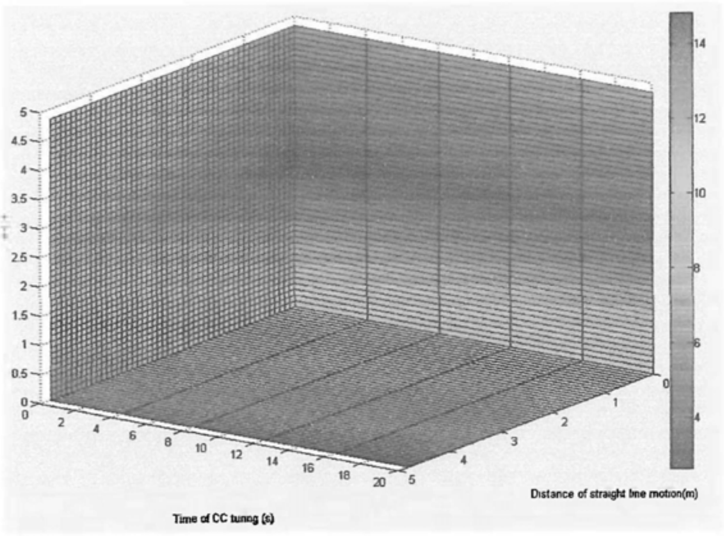

Figure 4.13: Aisle width cube in the 3D parameter space

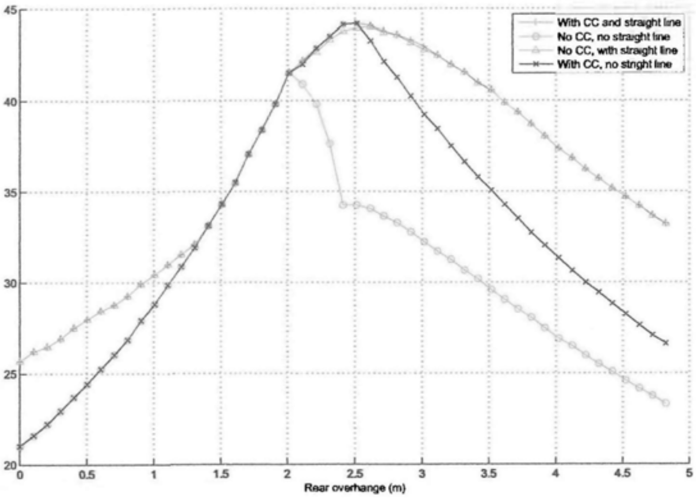

Figure 4.14: Maximal space efficiency with respect to rear overhang

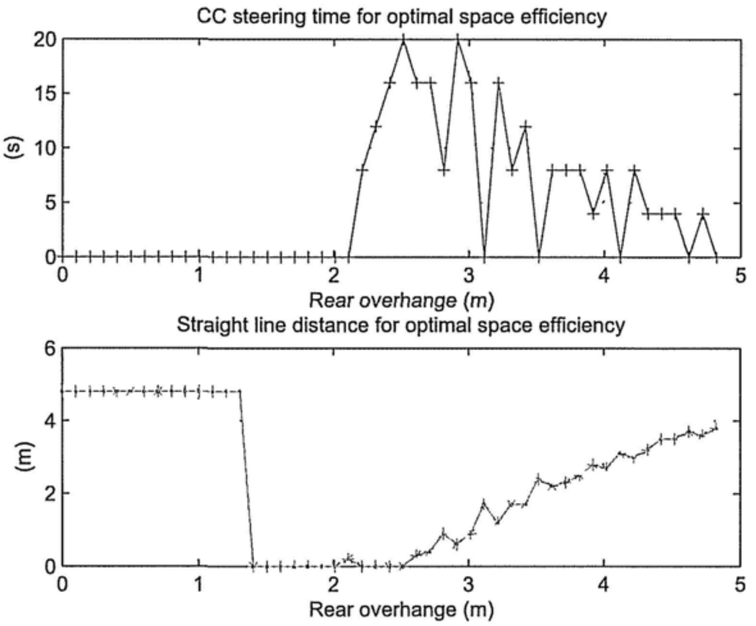

Figure 4.15: Behavioral parameters with respect to structural parameter for each space efficiency maximum

the asymptotic space efficiencies for single line and double line parking reach their highest level of about 44.2% and 56.5%, respectively. The slot and aisle widths are $W_S = 2.32$ and $W_A = 3.74$, respectively. The arrangement of slot and aisle widths, as well as the contour, are illustrated in Figure 4.16.

From Figure 4.10(b), when $\Delta t = 0$ and $d_f = 4.8$, the asymptotic space efficiencies for single line and double line parking are maximized at about 31.0% and 47.2%, respectively. The aisle width is 10.67 and the slot width is 1.83. From Figure 4.10(f)[1], when $\Delta t = 8$ and $d_f = 2.1$, the asymptotic space efficiencies for reverse parking of the Toyota in the single line and double line parking scenarios are maximized at approximately 39.3% and 55.6%,

---

[1] When the rear overhang is the complement to 1.10m, i.e. b =3.72=L-1.10, forward parking under this structure is the same as in the case of reverse parking with the complement rear overhang.

respectively. The corresponding aisle and slot widths are 6.80 and 1.92, respectively. It is interesting to note that although there is a difference of approximately 5% in $\tilde{\eta}_{SS}$ for reverse parking of front-wheel steering vehicles with $b = 1.10$ and $b = 2.41$[2], this difference is reduced significantly to less than 1% in double line parking. This partially explains why vehicles are commonly parked in reverse in parking lots.

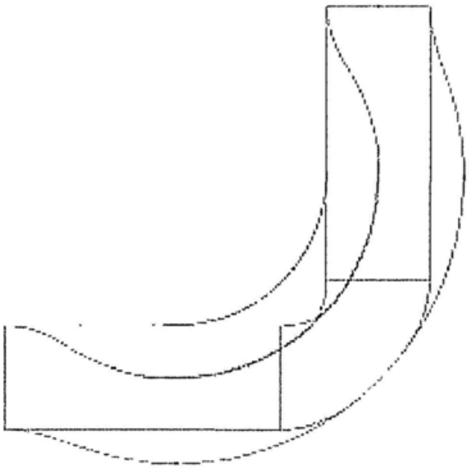

Figure 4.16: Contour for maximal space efficiency for traditional vehicle structure

Table 4.2: Experimental results for front-wheel-steering vehicle parking

b (m)	W_A (m)	W_S (m)	d_f (m)	Δt (s)	$\tilde{\eta}_{SS}$	$\tilde{\eta}_{SD}$
1.10	10.67	1.83	4.8	0	31.0%	47.2%
2.41	3.74	2.32	0	16	44.2%	56.5%
3.72	6.80	1.92	2.1	8	39.3%	55.6%

---

[2] Because the rear axis is in the center of the vehicle body, reverse parking and forward parking are the same.

4.2.2 Parking Based on Zero Radius Turning Motion

Occupancy Area Contour

The area in which the ISDV is parked in a perpendicularly arranged slot is occupied in three steps: (i) translation from the entrance to the appropriate position for turning; (ii) 90-degree ZRT to adjust the heading direction; and (iii) translation to the final parking position.

The second and most significant step is shown in Figure 4.17.

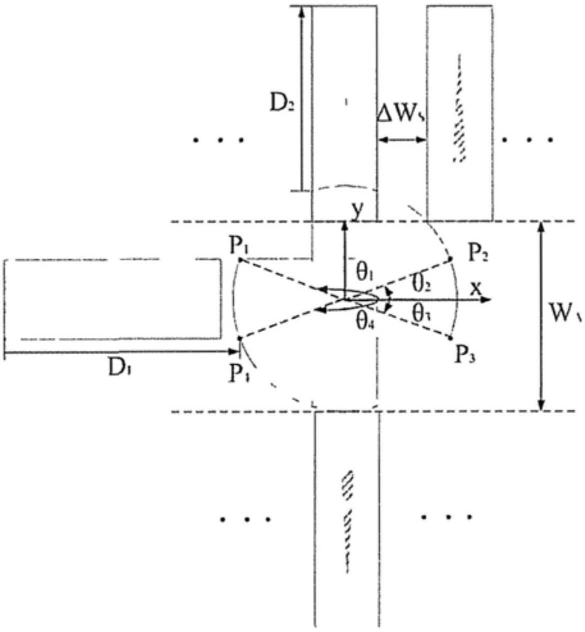

Figure 4.17: Parking of the ISDV

The extreme points of the ZRT are the four points at each corner of the vehicle body. Their trajectories form part of a circle.

$$T_i = \frac{\sqrt{L^2 + W^2}}{2} \begin{pmatrix} \cos(\theta_i + \omega t) \\ \sin(\theta_i + \omega t) \end{pmatrix} \tag{4.18}$$

where T_i is the trajectory of the point P_i, $i = 1, 2, 3, 4$, ω is the rotational speed, θ_i is the initial phase of P_i, and $0 < t < \frac{\pi}{2\omega}$

The rest of the contour for this step consists of the line segments of the vehicle's initial and final state.

Slot Arrangement

The third step-translation of displacement D_2 from the adjusted altitude to the final slot-determines the position of the final slot and also determines the width of the aisle and the final gap between the slots. The aisle width can be expressed by

$$W_A = D_2 + \frac{\sqrt{W^2 + L^2} - L}{2} \tag{4.19}$$

To prevent the upper aisle from being swept by the vehicle's left boundary in the first step of translation, the aisle should satisfy

$$W_A > \frac{L + W}{2} + \frac{\sqrt{W^2 + L^2} - L}{2} \tag{4.20}$$

By substituting equation 4.2.2,

$$D_2 > \frac{L + W}{2} \tag{4.21}$$

The gap between the parking vehicle and the parked vehicles depends on the trajectories of P_2 and P_3.

$$\Delta W_S = \begin{cases} \sqrt{(\frac{W}{2})^2 + (\frac{L}{2})^2 - (D_2 - \frac{L}{2})^2} - \frac{W}{2} & \text{if } \frac{L+W}{2} \leq D_2 \leq L \\ 0 & \text{if } D_2 > L \end{cases} \tag{4.22}$$

For parking one vehicle in a single line arrangement or parking two vehicles in a double line arrangement, the basic area requirements are

$$A_{basic\_single} = \left(D_2 + \frac{\sqrt{W^2 + L^2} + L}{2} \right) \left(\frac{\sqrt{L^2 + W^2} + W}{2} + \Delta W_S \right) \tag{4.23}$$

$$A_{basic\_double} = \left(D_2 + \frac{\sqrt{W^2 + L^2} + L}{2} + L \right) \left(\frac{\sqrt{L^2 + W^2} + W}{2} + \Delta W_S \right) \tag{4.24}$$

For any additional vehicle in the single line arrangement or any two vehicles in the double line arrangement, the additional area needed is

$$A_{additional\_single} = \left(D_2 + \frac{\sqrt{W^2 + L^2} + L}{2} \right) (W + \Delta W_S) \tag{4.25}$$

$$A_{additional\_double} = \left(D_2 + \frac{\sqrt{W^2 + L^2} + L}{2} + L \right) (W + \Delta W_S) \tag{4.26}$$

Hence, the space efficiency of a single line parking lot with a capacity of n ISDV is

$$\eta_{SS} = \frac{nWL}{A_{basicsingle} + (n-1)A_{additionalsingle}} \tag{4.27}$$

That for the double line parking lot with a capacity of $2n$ ISDV is

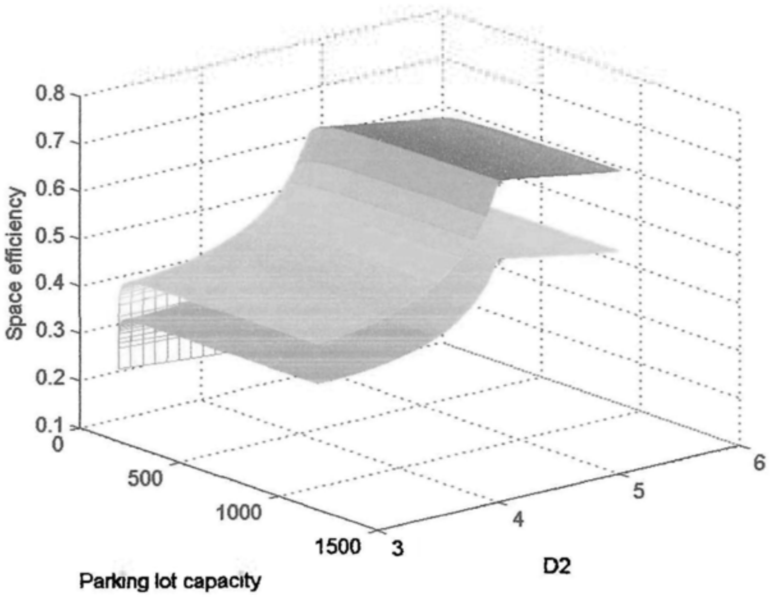

Figure 4.18: Space efficiency of ISDV parking

$$\eta_{SD} = \frac{2nWL}{A_{basicdouble} + (n-1)A_{additionaldouble}} \tag{4.28}$$

Computational Result

For vehicles with a fixed width and length, I simulate parking space efficiency for the two types of manipulation (i.e. forward and reverse parking) in the two types of slot arrangement (i.e. single line and double line). It is revealed that space efficiency for vehicles with a fixed width and length depends on the size of the rear overhang and the number of vehicles.

For the ISDV, the simulation is conducted in terms of variation in D_2 (within $[\frac{L+W}{2}, L+1]$)[3] and number of vehicles (within $[1, 1000]$).

---

[3] The upper bound $L+1$ is aimed at establishing that the maximal point at L is included in the interval

Table 4.3: Space efficiency of ISDV

	Single line	Double line
D_2	4.82	
Slot width (m)	1.82	
Aisle width (m)	4.99	4.99
Space efficiency (capacity=1000)	49.1%	65.8%
Asympotic space efficiency	49.1%	65.9%

Figure 4.18 illustrates that the double line arrangement (the higher layer) for ISDV has the highest space efficiency of 65.8% when $D_2 = L = 4.82$ and the number of vehicles reaches the maximum. With the same value for D_2 and the same number of vehicles, the special efficiency of the single line arrangement (the lower layer) is 49.1%.

Thus, in comparison with 2WS vehicles, the ISDV provides a higher level of space efficiency for parking regardless of how their structural parameters, such as the size of the rear overhang, are changed.

Based on the investigation discussed above, I test the ISDV for parking in a narrow workshop. Snapshots of different points in the parking process are shown in Figure 2.28.

4.2.3 Parking Based on Freely Omni-directional Motion

Motion-slot Modeling

It is arguable that because the vehicle is omnidirectional, there might be types of omnidirectional motion other than ZRT that allow for free and unconstrained motion. Because there will be no kinematic constraint on any such system, the motion contour is arbitrary and thus the contour space will be infinitely large. Consequently, the contour-based search method for aisle and slot widths discussed previously is not applicable here.

For analysis of this type of omnidirectional motion, I propose an analytical geometry-based approach for modeling the aisle-slot combination in space efficiency analysis.

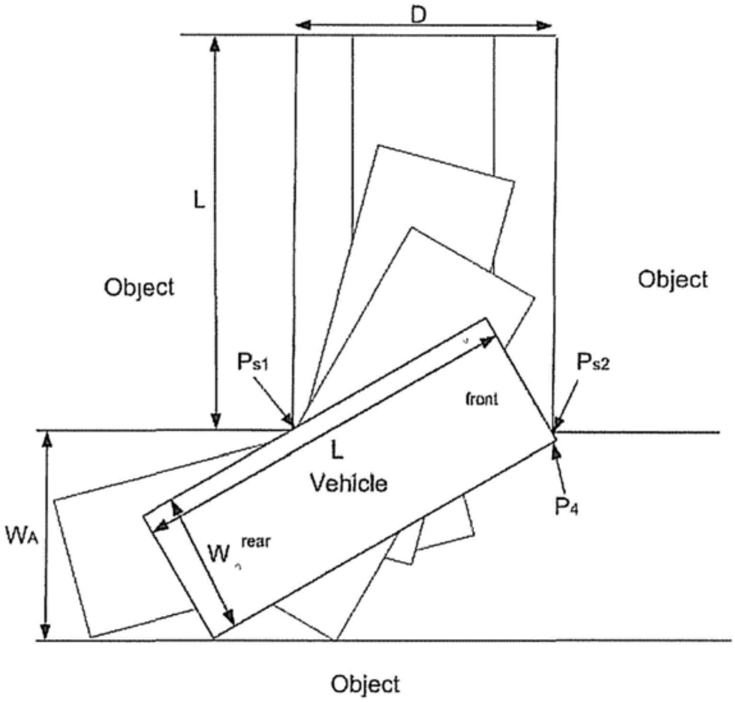

Figure 4.19: Outline for freely omni-directional motion

Figure 4.19 shows the vehicle being parked in an freely omnidirectional motion. It can be seen that the aisle width should satisfy $W \leq W_A \leq \sqrt{W^2 + L^2}$. A narrower aisle width will lead to the vehicle being unable to enter the aisle, while a larger aisle width will lead to space being wasted as the two ends of the longest line in the vehicle will not touch the two aisle boundaries simultaneously.

The vertical parking problem can be transformed into a problem of increasing the state θ from 0 to $\frac{\pi}{2}$ without the vehicle colliding with objects.

For a given aisle width W_A, the narrowest slot width will result in the left corner point P_{s1} of the object touching the left edge of the vehicle. If there is any gap between them, the slot will not be at its narrowest.

The other slot boundary constraint is imposed by either the right corner point P_{s2} of the object or the right front corner P_4 of the vehicle.

There are two cases in which a point on the vehicle's edge comes into contact with objects during a left hand turn. These are now analyzed in detail geometrically.

1. Case 1 When θ is small, the narrowest slot that can be achieved will lead to P_{s2} coming into contact with the vehicle's front boundary.

2. Case 2

   When θ increases, the front of the vehicle slides into the slot. In this case, the narrowest slot that can be achieved will lead to P_r coming into contact with the boundary of the right hand slot.

These two cases can be integrated using the alternative method illustrated in Figure 4.22. First fix a coordinate frame to the vehicle body with P_6 as the origin, $\overrightarrow{P_6P_5}$ as the $\overrightarrow{X_b}$ direction, and $\overrightarrow{P_6P_1}$ as the $\overrightarrow{Y_b}$ direction. Then draw a quarter circle with radius W_A. It will intersect with $\overrightarrow{X_b}$ and $\overrightarrow{Y_b}$ at A and B, respectively.

For each point P_T on the quarter circle, a tangent line can be drawn. This line is the location of the upper aisle boundary when P_6 is on the lower aisle

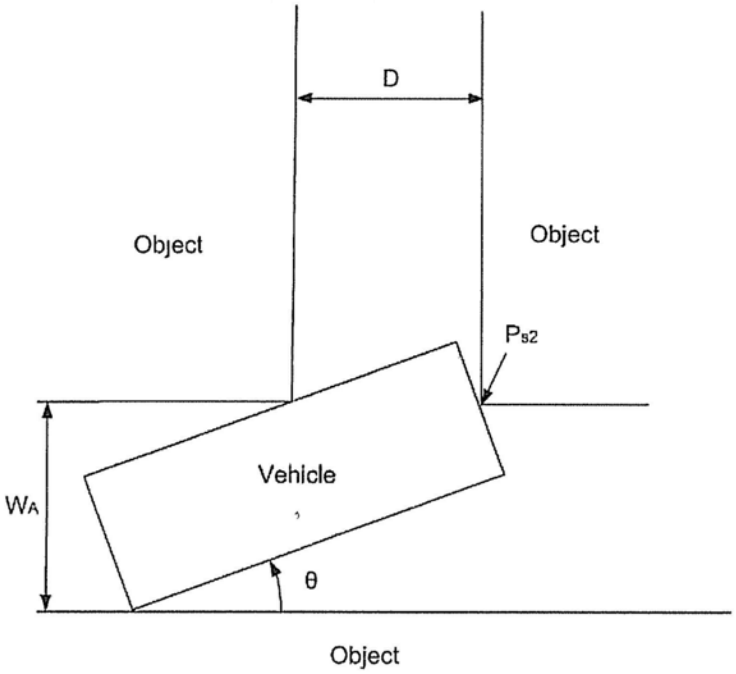

Figure 4.20: Case 1 of edge-point contact

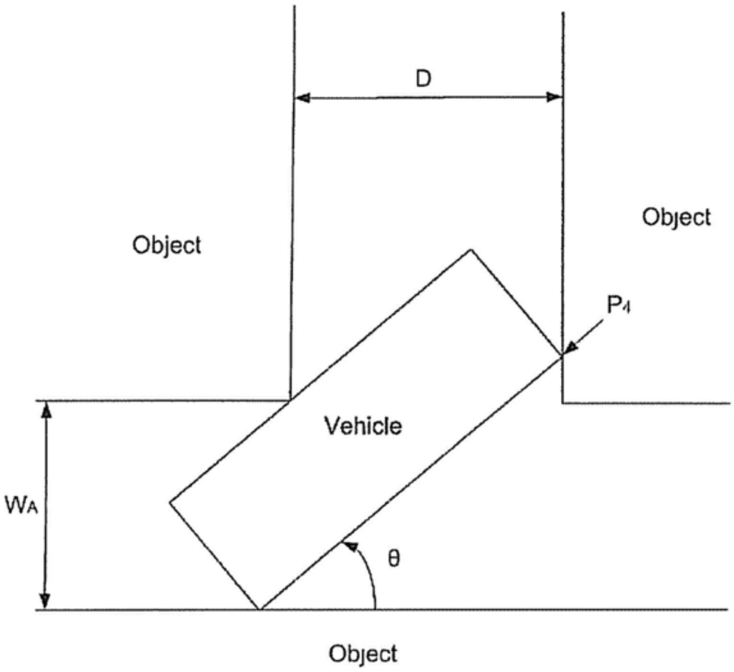

Figure 4.21: Case 2 of edge-point contact

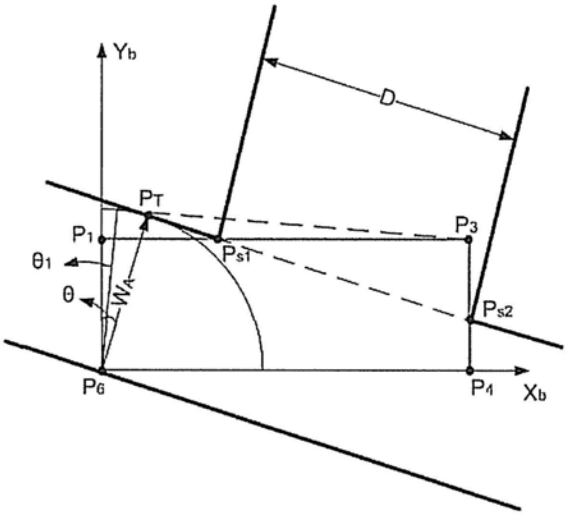

Figure 4.22: Tangent point variance case 1 for type 1

boundary. When it intersects with the vehicle body, part of the vehicle is in the slot. Otherwise, the entire vehicle body is in the aisle. The attitude of the vehicle, i.e. θ, is equivalent to the angle spanned by $\overrightarrow{Y_b}$ and the normal vector $\overrightarrow{P_6P_T}$ that is perpendicular to the tangent line.

W_A can be divided into two intervals.

1. $W_A \in (W, L]$

There must be a tangent line going through P_3. Denote the corresponding angle as θ_1. When $\theta < \theta_1$, the tangent line will not intersect with the vehicle body, indicating that the entire vehicle is in the aisle.

The analytic-geometric method can be used to derive the equation whereby

$$\theta_1 = \arcsin \frac{W_A}{\sqrt{L^2 + W^2}} - \arcsin \frac{W}{\sqrt{L^2 + W^2}} \tag{4.29}$$

As θ increase from θ_1, the tangent line will first intersect the boundaries $\overline{P_1P_3}$ and $\overline{P_3P_4}$ at P_{s1} and P_{s2}, respectively. Based on analytical geometry, it is not difficult to obtain their coordinates as

$$\begin{cases} X_b(P_{s1}) & = & \frac{W_A}{\sin(\theta)} - \frac{W_A}{\tan(\theta)} \\ Y_b(P_{s1}) & = & W \end{cases} \tag{4.30}$$

where $X_b(P)$ and $Y_b(P)$ are the coordinates in the X_b and Y_b directions in the $X_bP_3Y_b$ coordinate frame.

$$\begin{cases} X(P_{s2}) & = & L \\ Y(P_{s2}) & = & \frac{W_A}{\cos(\theta)} - L\tan(\theta) \end{cases} \tag{4.31}$$

Hence, if the slot width can vary to maintain contact at P_{s1} and P_{s2},

$$\begin{aligned} D^2 &= \left(L - \frac{W_A}{\sin(\theta)} + \frac{W}{\tan(\theta)}\right)^2 + \left(W + L\tan(\theta) - \frac{W_A}{\cos(\theta)}\right)^2 \\ &= L^2 + \frac{W_A^2}{\sin^2(\theta)} + \frac{W^2}{\tan^2(\theta)} - \frac{2LW_A}{\sin(\theta)} + \frac{2LW}{\tan(\theta)} - \frac{2W_AW\cos(\theta)}{\sin^2(\theta)} \\ &\quad + W^2 + L^2\tan^2(\theta) + \frac{W_A^2}{\cos^2(\theta)} + 2WL\tan(\theta) - \frac{2W_AW}{\cos(\theta)} - \frac{2W_AL\sin(\theta)}{\cos^2(\theta)} \\ &= \left(\frac{W_A}{\sin(\theta)\cos(\theta)} - \frac{L}{\cos(\theta)} - \frac{W}{\sin(\theta)}\right)^2 \end{aligned} \tag{4.32}$$

And therefore

$$D = \left|\frac{W_A}{\sin(\theta)\cos(\theta)} - \frac{L}{\cos(\theta)} - \frac{W}{\sin(\theta)}\right| \tag{4.33}$$

As θ passes $\arcsin(\frac{W_A}{L})$, case 1 evolves into cases 2.

The coordinate of P_{s1} can still be expressed by equation 4.30. However,

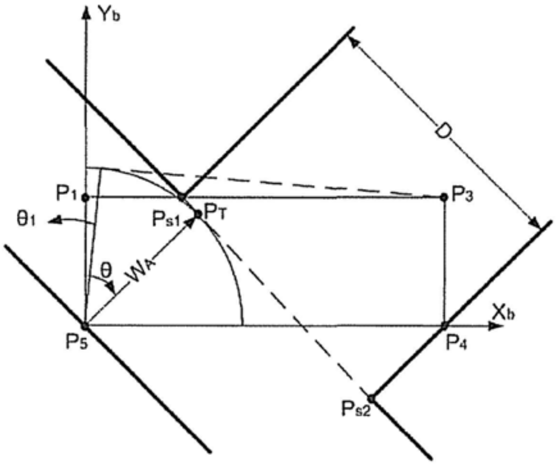

Figure 4.23: Tangent point variance case 2 for type 1

the position of P_{s2} becomes

$$\begin{cases} X(P_{s2}) & = & W_A \sin(\theta) + L\cos^2(\theta) \\ Y(P_{s2}) & = & W_A \cos(\theta) - L\sin(\theta)\cos(\theta) \end{cases} \tag{4.34}$$

Thereafter,

$$\begin{aligned} D^2 &= (W_A \sin(\theta) + L\cos^2(\theta) - \tfrac{W_A}{\sin(\theta)} + \tfrac{W\cos(\theta)}{\sin(\theta)})^2 + (W_A\cos(\theta) - L\sin(\theta)\cos(\theta) - W)^2 \\ &= \tfrac{\cos^4(\theta)}{\sin^2(\theta)} W_A^2 + L^2\cos^2(\theta) + \tfrac{W^2}{\sin(\theta)} - \tfrac{W_A L\cos^2(\theta)}{\sin(\theta)} - \tfrac{W_A W\cos(\theta)}{\sin^2(\theta)} + \tfrac{2LW\cos(\theta)}{\sin(\theta)} \\ &= \left(\tfrac{W_A}{\tan(\theta)} - L\cos(\theta) - \tfrac{W}{\sin(\theta)}\right) \end{aligned} \tag{4.35}$$

Hence,

$$D = \left|\frac{W_A}{\tan(\theta)} - L\cos(\theta) - \frac{W}{\sin(\theta)}\right| \tag{4.36}$$

For all $\theta \in [\theta_1, \frac{\pi}{2}]$, D will be computed. The minimal distance required to allow the vehicle to perform the motion will be $\max(D)$. The attitude θ at which D is maximized is derived as

$$\hat{\theta} = arg_{\theta} \max(D(\theta)) \tag{4.37}$$

$\hat{\theta}$ is the bottleneck attitude at which no further translation is permitted. After $\hat{\theta}$, D falls to permit more unconstrained motion. It can be seen that because the possible range of motion is freely omnidirectional, it is better that the vehicles on the left and the right are equidistant. Hence,

$$W_s = \frac{D(\hat{\theta}) + W}{2} \tag{4.38}$$

2. $W_A \in (L, \sqrt{W^2 + L^2})$

When the aisle width exceeds L, the slot width requirement is relaxed even further. Figure 4.24 shows that only case 1 exists, whereas case 2 is eliminated.

In this type of motion, meaningful values for θ are bounded in the interval between θ_1 and θ_2.

θ_1 is the same as that derived by equation 4.29, while

$$\theta_2 = \arccos \frac{W_A}{\sqrt{L^2 + W^2}} + \arccos \frac{W}{\sqrt{L^2 + W^2}} \tag{4.39}$$

Hence, D is computed in the same way as in equation 4.33

Moreover, it should be noted that in the interval of $W_A \in (L, \sqrt{W^2 + L^2})$, D can be less than W, which will lead to an unreasonable result.

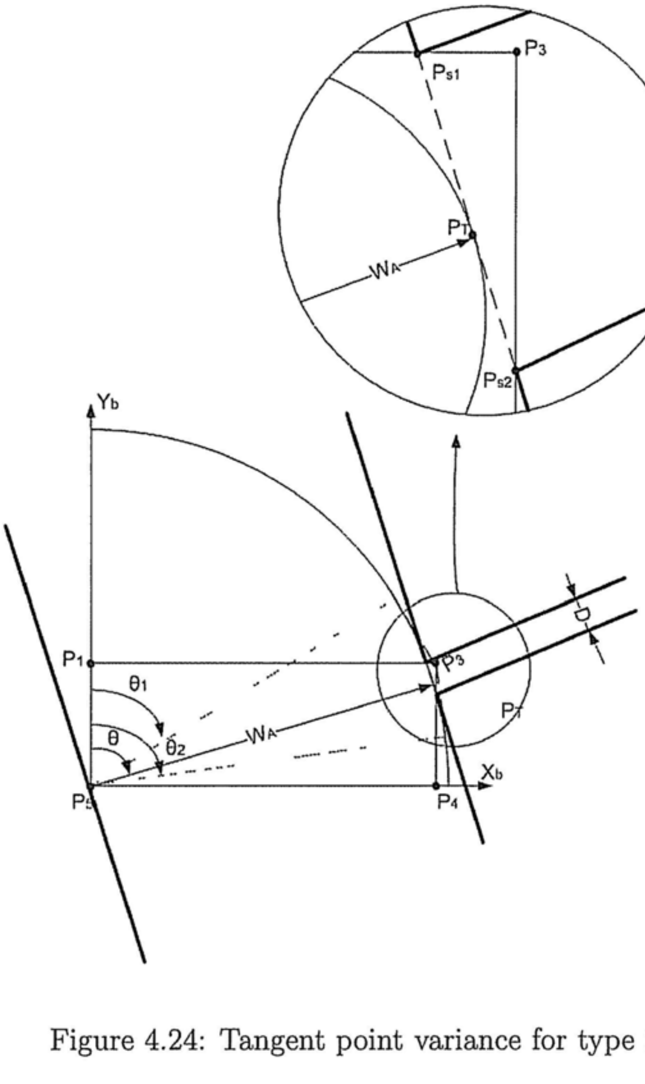

Figure 4.24: Tangent point variance for type 2

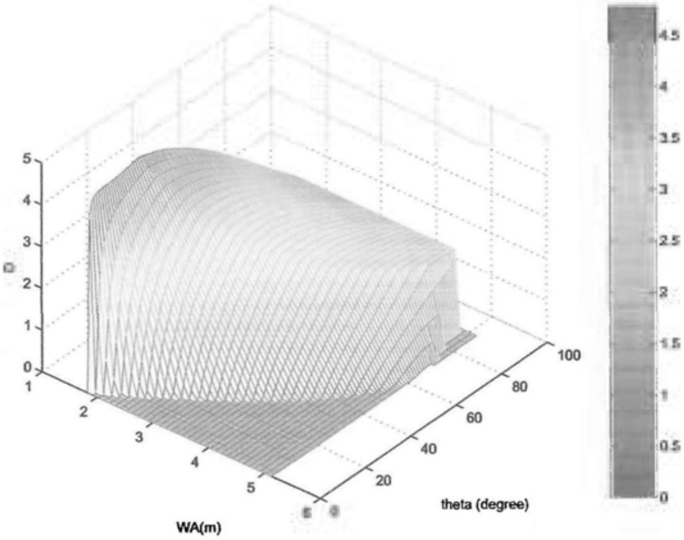

Figure 4.25: Distance from the left and right objects

Thus,

$$W_s = \max\left(\frac{D+W}{2}, W\right) \tag{4.40}$$

Computational Result

The results of computing D with respect to W_A and θ are reported in Figure 4.25.

The asymptotic space efficiencies for the single and double line parking scenarios are

$$\tilde{\eta}_{SA} = \frac{WL}{W_S(W_A + L)} \tag{4.41}$$

$$\tilde{\eta}_{DA} = \frac{2WL}{W_S(W_A + 2L)} \tag{4.42}$$

Figure 4.26 shows the computational results for asymptotic space efficiency over $W_A \in (W, \sqrt{W^2 + L^2}]$. When $W_A = L$, $\tilde{\eta}_{SA}$ is maximized at

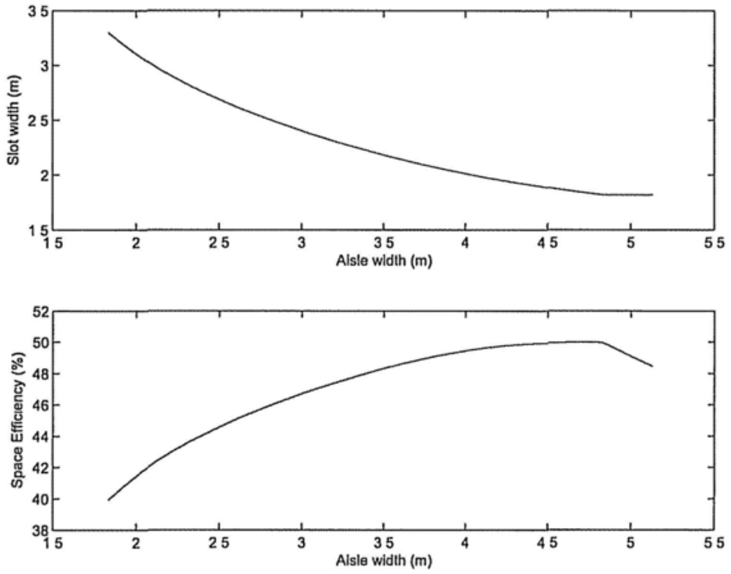

Figure 4.26: Asympotic space efficiency for freely omni-directional motion

50%. Note that this result is for single layer parking. When vehicles are parked on both sides of the aisle, $\tilde{\eta}_{DA}$ reaches a maximum value of about 66.7%.

This result is approximately the same as that achieved in the parking motion combining ZRT with straight line translation.

4.2.4 Summary of Space Analysis

Table 4.4 summarizes the experimental results discussed in space analysis. It shows that in comparison with traditional front-wheel steering vehicles, the ISDV offers 10% more asymptotic space efficiency in single line parking scenarios and 18% more asymptotic space efficiency than that of forward parking in a double line parking lot. Both forms of omnidirectional motion considered deliver asymptotic space efficiency of approximately 50% in the single line scenario and 66.7% in the double line scenario. They are therefore somewhat similar in terms of space efficiency.

Table 4.4: Comparison of asympotic space efficiencies for front-wheel-steering vehicles and the ISDV

			Asympotic space efficiency	
			Single line	Double line
Front wheel steering	b=1.10m	Forward	31.0%	47.2%
		Reverse	39.3%	55.6%
	b=2.41m		44.2%	56.5%
Omni-directional	ZRT-based		49.1%	65.9%
	Free motion		50%	66.7%

4.3 Time Analysis of Parking

Aside of space, it is also much concerned in the aspect of time, because this indicates how convenient the vehicle could be parked.

4.3.1 Final State Approximation

Parking effort is related to the time needed to park a vehicle in its final state (x_f, y_f, θ_f). However, in some circumstances, it can be highly difficult or sometimes even impractical to park the vehicle in the exact final state. Hence, I release the final state constraint for successful parking to an expanded rectangular zone with a small variation in Δ in both the x and y directions. In Figure 4.27, the hollow circular dot shows the precise final position with altitude $\frac{\pi}{2}$, while the black dot in the rear axis marks the approximate final position with altitude θ. The four corner points are marked by the four remaining black dots.

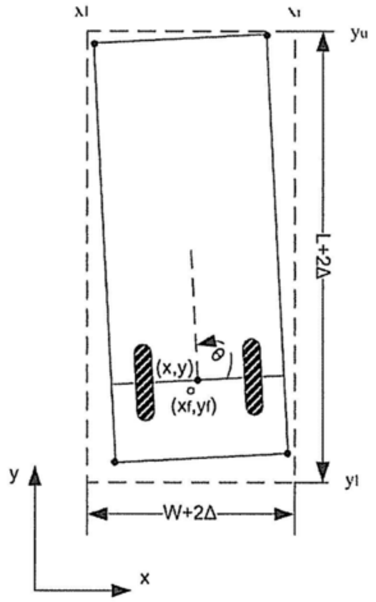

Figure 4.27: Final state approximation

Because the vehicle body is a polygon, the sufficient-necessary condition for the vehicle to be bounded in this square is that all four corner points of the vehicle rectangle are bounded by this expanded square. Denote the x coordinates of the left and right boundaries of the expanded rectangle as x_l and x_r, and the y coordinates of the lower and upper boundaries as y_l and y_u.

Then

$$\begin{cases} x_l = x_f - \frac{W}{2} - \Delta \\ x_r = x_f + \frac{W}{2} + \Delta \\ y_l = y_f - b - \Delta \\ y_u = y_f + L - b + \Delta \end{cases} \tag{4.43}$$

Hence,

$$\begin{cases} x_l \le x + (L-b)\cos\theta + \frac{W}{2}\cos(\theta + \frac{\pi}{2}) \le x_r \\ x_l \le x + (L-b)\cos\theta + \frac{W}{2}\cos(\theta - \frac{\pi}{2}) \le x_r \\ x_l \le x + b\cos(\theta+\pi) + \frac{W}{2}\cos(\theta + \frac{\pi}{2}) \le x_r \\ x_l \le x + b\cos(\theta+\pi) + \frac{W}{2}\cos(\theta - \frac{\pi}{2}) \le x_r \\ y_l \le y + (L-b)\sin\theta + \frac{W}{2}\sin(\theta + \frac{\pi}{2}) \le y_r \\ y_l \le y + (L-b)\sin\theta + \frac{W}{2}\sin(\theta - \frac{\pi}{2}) \le y_r \\ y_l \le y + b\sin(\theta+\pi) + \frac{W}{2}\sin(\theta + \frac{\pi}{2}) \le y_r \\ y_l \le y + b\sin(\theta+\pi) + \frac{W}{2}\sin(\theta - \frac{\pi}{2}) \le y_r \end{cases} \tag{4.44}$$

To save computational effort, geometrical analysis shows that there are two cases in which (x, y, θ) is in the small neighborhood of $(x_f, y_f, \frac{\pi}{2})$, as discussed below.

1)When $\theta \le \frac{\pi}{2}$,

$$\begin{cases} x + (L-b)\cos\theta + \frac{W}{2}\cos(\theta - \frac{\pi}{2}) \le x_r \\ x + b\cos(\theta+\pi) + \frac{W}{2}\cos(\theta + \frac{\pi}{2}) \ge x_l \\ y + (L-b)\sin\theta + \frac{W}{2}\sin(\theta + \frac{\pi}{2}) \le y_u \\ y + b\sin(\theta+\pi) + \frac{W}{2}\sin(\theta - \frac{\pi}{2}) \ge y_l \end{cases} \tag{4.45}$$

2) When $\theta > \frac{\pi}{2}$,

$$\begin{cases} x + (L-b)\cos\theta + \frac{W}{2}\cos(\theta + \frac{\pi}{2}) & \geq \; x_l \\ x + b\cos(\theta + \pi) + \frac{W}{2}\cos(\theta - \frac{\pi}{2}) & \leq \; x_r \\ y + (L-b)\sin\theta + \frac{W}{2}\sin(\theta - \frac{\pi}{2}) & \leq \; y_u \\ y + b\sin(\theta + \pi) + \frac{W}{2}\sin(\theta - \frac{\pi}{2}) & \geq \; y_l \end{cases} \tag{4.46}$$

4.3.2 Collision Detection

In the simulation environment, it is necessary to detect any collision that occurs to allow for the parking trial to be terminated. Because all the objects (the vehicles with blue surrounding bars (Figure 4.28)) and the vehicle to be parked (the vehicle with yellow surrounding bars) are polygonal, one intuitive idea is to ascertain whether (1) any vertex of objects is inside the vehicle body; or (2) any vertex of the vehicle is inside the body of any object. However, neither of these events alone will work on all occasions. For instance, (1) cannot detect the situation in Figure 4.28(b) and (2) cannot detect the situation in Figure 4.28(a). Even worse, neither of them can detect the situation in Figure 4.28(c).

Hence, in the simulation, collisions are detected when none of the line boundary segments in the parking vehicle set intersect with any of the line boundary segments in the object set.

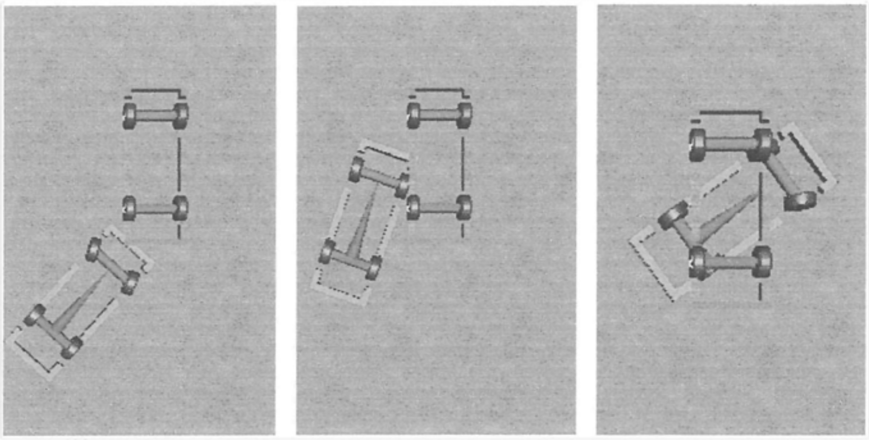

(a) Collision detectable by (1) but not by (2) (b) Collision detectable by (2) but not by (1) (c) Collision not detectable by either (1) or (2)

Figure 4.28: Collisions

4.3.3 Aisle and Slot Widths Selection

In the section dealing with space efficiency, I compute both the aisle and slot widths in the steering manipulation space, which consists of CC turn time Δt and final straight distance d_F. For each rear overhang, there will be two 2D matrices: M_{W_A} for aisle width and M_{W_S} for slot width. This chapter looks into these two matrices to investigate the problem of how much effort is needed to park the vehicle in that scenario given a combination of aisle and slot widths.

Parking Behavior Parameter Histogram

For each pair of parking behavior parameters $(\Delta t_0, d_{F0})$, there will be one combination of (W_{A0}, W_{S0}), that permits the specific parking manipulation to be performed without requiring any additional space.

The objective of this section is to analyze the parking effort required in the

2D aisle-width space. For this purpose, the space (W_A, W_S) can be discretized to construct a parking parameter histogram denoted as $N(W_A, W_S)$, which indicates the total number of parking parameter pairs that permit the vehicle to be parked in the aisle-slot pair (W_A, W_S). The discretization step is $\frac{\Delta}{2}$. Δ is the parking error in Equation 4.3.1.

W_A and W_S are discretized into N_A and N_S points, denoted as $W_A[p]$ and $W_S[q]$ $(1 \leq p \leq N_A,\ 1 \leq q \leq N_S)$, respectively. The matrices M_{W_A} and M_{W_S} are scanned simultaneously. In the pair of entries $M_{W_A}(i,j)$ and $M_{W_S}(i,j)$, i and j indicate the two parking maniputlation parameters $\Delta t_0(i)$ and $d_F(j)$.

If $W_A[p-1] < M_{W_A}(i,j) \leq W_A[p]$ and $W_S[q-1] < M_{W_S}(i,j) \leq W_S[q]$, then the parking parameter for $(W_A[p], W_S[q])$ increases by one unit. The upper bound rather than the lower bound is selected for histogram construction; otherwise, the parking parameters would be mistakenly put into the aisle-slot width pair that does not permit the relevant parking manipulation.

Figure 4.29 illustrates the histogram constructed for a traditional vehicle with rear overhang $b = 1.10m$.

The barrier with broader aisle and slot widths is for the forward parking manipulation, while the other barrier is for reverse parking.

Let $N(W_A[p], W_S[q])$ denote the histogram value in $(W_A[p], W_S[q])$. If $N(W_A[p], W_S[q]) > 0$, there is parking manipulation that allows for the vehicle to be parked. However, it is not necessary that there be no permitted parking manipulation if $N(W_A[p], W_S[q]) = 0$. A cumulative histogram is constructed to tackle this problem.

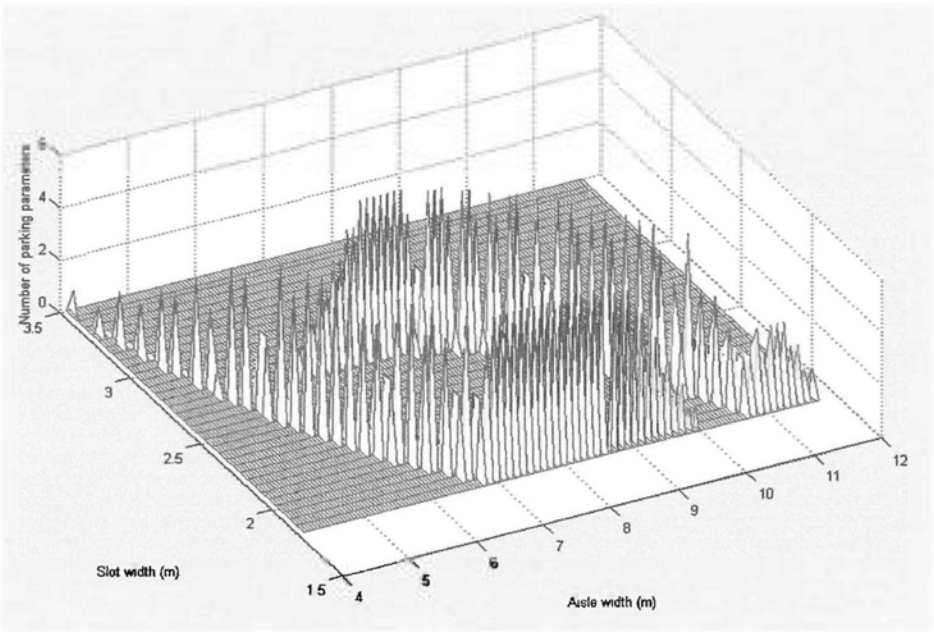

Figure 4.29: Parking parameters with respect to aisle and slot widths

Denote the cumulative histogram as $N_C(W_A[p], W_S[q])$.

$$N_C(W_A[p], W_S[q]) = \sum_{i=1}^{p} \sum_{j=1}^{q} N(W_A[i], W_S[j]) \tag{4.47}$$

The cumulative histogram can then be related to the ease of parking the vehicle for the pair $(W_A[p], W_S[q])$.

Combined Efficiency

It can be seen that the broader the widths W_A and W_S, the easier it is to park the vehicle. However, given that an increase in these widths will also reduce the asymptotic space efficiency of the vehicle, there must be a tradeoff between space efficiency and time efficiency.

Asymptotic space efficiency for the single line parking scenario defined in

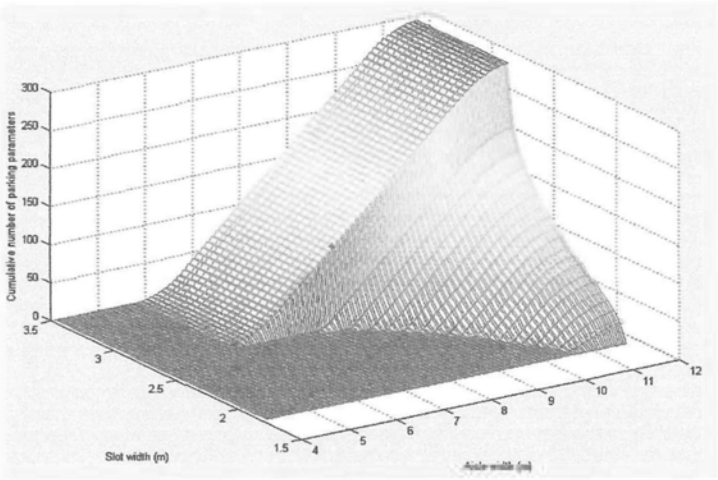

Figure 4.30: Cumulative parking parameters with respect to aisle and slot widths (forward parking)

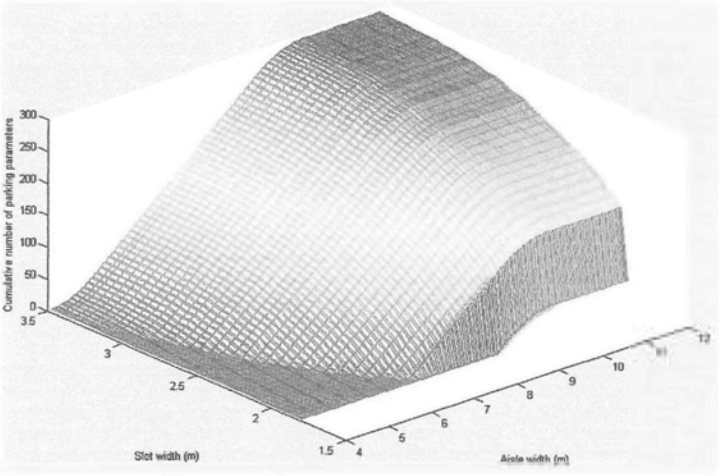

Figure 4.31: Cumulative parking parameters with respect to aisle and slot widths (backward parking)

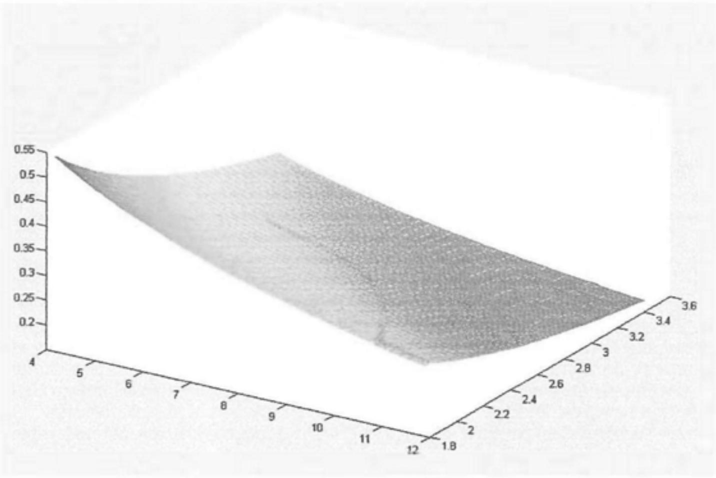

Figure 4.32: Asympotic space efficiency for single line parking

$$\tilde{\eta}_S(W_A, W_S) = \frac{LW}{W_S(L + W_A)} \tag{4.48}$$

is illustrated in Figure 4.32.

Combined efficiency considers both space efficiency and time efficiency and is defined below.

$$\eta_{ST} = \bar{\eta}_S \cdot \bar{\eta}_T \tag{4.49}$$

$$\bar{\eta}_S = \frac{\eta_S - \min(\eta_S)}{\max(\eta_S) - \min(\eta_S)} \tag{4.50}$$

$$\bar{\eta}_T = \frac{f(N_C, threshold_{N_C})}{threshold_{N_C}} \tag{4.51}$$

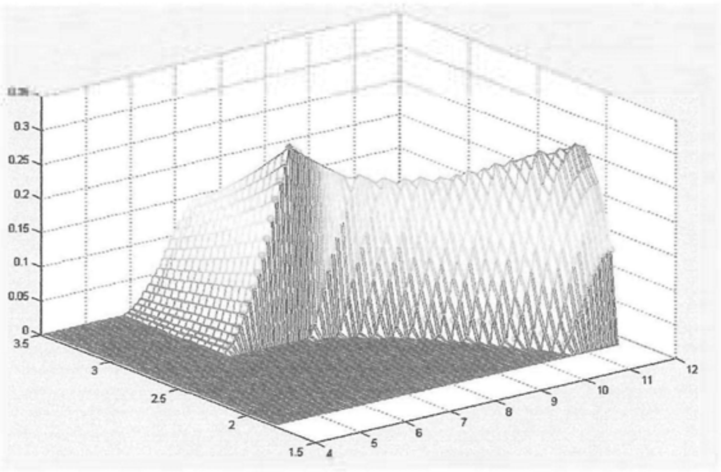

Figure 4.33: Combined efficiency for forward parking ($threshold_{NC} = 60$)

where

$$f(N_C, threshold_{N_C}) = \begin{cases} N_C & if N_C < threshold_{N_C} \\ threshold_{N_C} & N_C \geq threshold_{N_C} \end{cases} \tag{4.52}$$

The threshold in Equation 4.52 includes nonlinear effort to reflect the parking parameters to such an extent that large values will have no additional effect on overall efficiency.

Combined efficiency for forward parking with $threshold_{NC} = 60$ is visualized in Figure 4.33. The maximal level of combined efficiency is located at $W_A = 7.30m$ and $W_S = 2.77m$.

Figure 4.34 shows the combined efficiency for reverse parking.

This aisle-slot pair with maximal combined efficiency in the forward parking scenario is used to test the time taken in practice to park the vehicle in the approximate final position.

The reason I choose forward parking rather than reverse parking is that

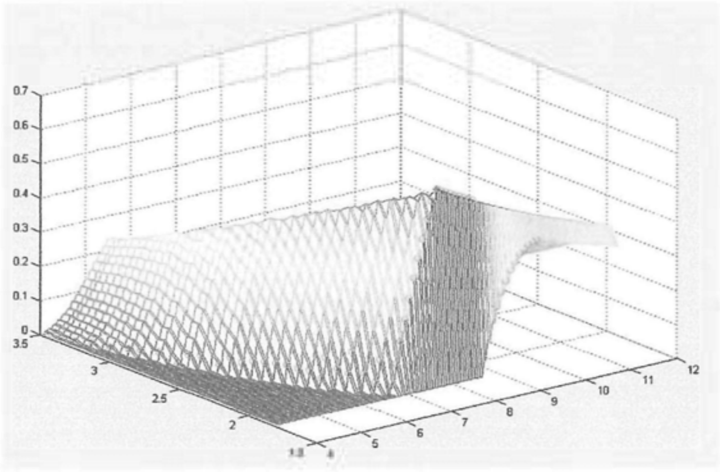

Figure 4.34: Combined efficiency for backward parking ($threshold_{NC} = 60$)

reverse parking normally includes forward translation, a shift change, then reverse parking. Thus, parking efficiency will be influenced greatly by the degree of accuracy in determining the point at which to change the shift. To avoid this influence, I analyze time efficiency in forward parking scenarios.

4.3.4 Experimental Results

Parking manipulation tests are both expensive and dangerous in the real environment as collisions will occur in tight parking scenarios. Hence, I conduct the time efficiency tests using a virtual reality environment and simulink in Matlab. This is a hardware-in-loop (HIL) platform as illustrated in Figure 2.23 in which the extended steering interface for the ISDV serves as the input.

Two scenarios are considered to evaluate the time efficiency of traditional vehicles (with different rear overhangs) and the ISDV. The first scenario is the aisle-slot widths pair $(7.30, 2.77)$ previously shown to maximize combined efficiency. The other scenario is more of a challenge: the aisle-slot widths pair $(5.87, 2.75)$ that delivers the optimal level of space efficiency for vehicles with a traditional rear overhang.

Scenario 1

To eliminate the effect of vehicle speed, the function of the accelerator pedal is not activated, i.e. the absolute speed of the center of the rear axis is fixed to a certain value (0.3 m/s, a normal parking speed) in these experiments. The braking pedal is used to control the sign of the speed. When it is released, the vehicle moves forward, and when it is depressed, the vehicle moves backward. It is difficult to park the vehicle in the approximate final state and iteration of forward-backward adjustments is sometimes necessary.

In the traditional vehicle experiments, two rear overhangs are tested: a traditional rear overhang of $1.10m$ and a rear overhang of $2.41m$ that delivers the optimal level of space efficiency in Figure 4.14. For these two types of rear overhang, the test driver controls the vehicle by changing ϕ_1 through the steering wheel. If the parking result does not satisfy the approximate final state, the driver can iteratively depress or release the brake pedal to drive the vehicle backward or forward and adjust the final position of the vehicle. Simulink records the total time taken to park successfully in the final state. If the vehicle collides with an object, the trial will be regarded as a failure.

As in the front-wheel steering vehicle experiments, the ISDV is also steered by the driver to test the time needed to park using ZRT-based motion and unresricted omnidirectional motion.

For each type of driving, the driver is asked to drive the vehicle in 20

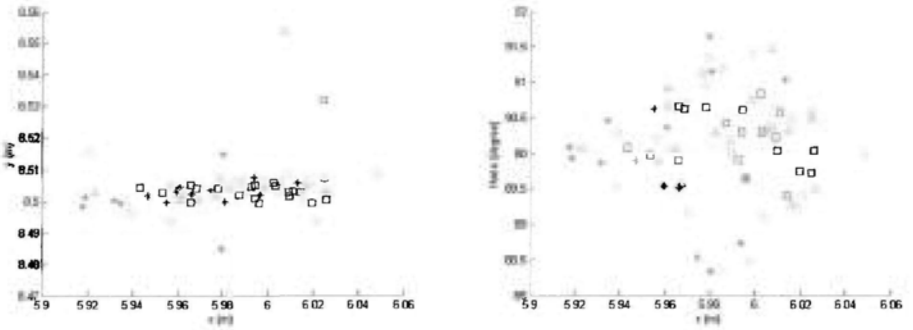

(a) X-Y view (b) X-θ view

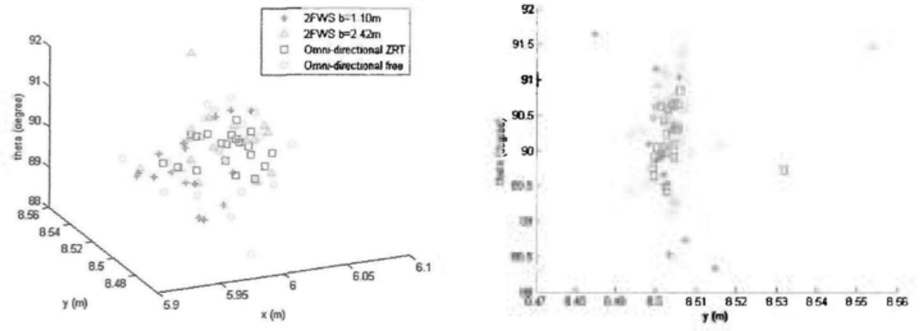

(c) 3D view (d) Y-θ view

Figure 4.35: Error cloud for scenario1

trials without gaining any prior experience of the scenario. The vehicle must be parked within the approximate final state of $\Delta = 0.08m$ for the parking result to be considered successful.

Table 4.5 summarizes the experimental results in Scenario 1. From the error rows, it can be seen that the approximate final state is achieved in all four groups of parking cases, although using a traditional vehicle results in a collision. This scenario tallies with the initial position of the traditional vehicle with a rear overhang of $1.10m$ shown in Figure 4.37. The driver does not find it particularly difficult to steer the vehicle a rear overhang of 1.10m

Table 4.5: Experiment result of time efficiency in scenario 1

	Traditional		Omni-directional	
	$b = 1.10m$	$b = 2.41m$	ZRT	Free motion
No. of collisions	4	1	0	0
Time mean (s)	61	65	60	45
Time standard deviation (s)	31	22	11	9
X error (cm)	4	3	2	3
Y error (cm)	1	1	1	1
θ error (o)	0.9	0.6	0.4	0.9

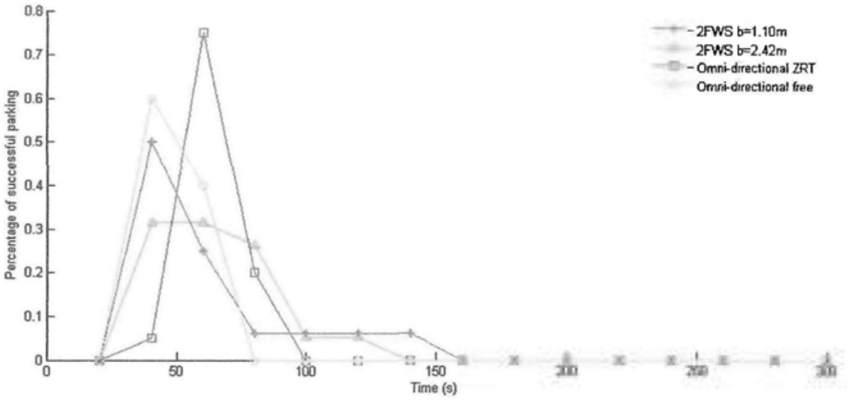

Figure 4.36: Time performance histogram in scenario 1

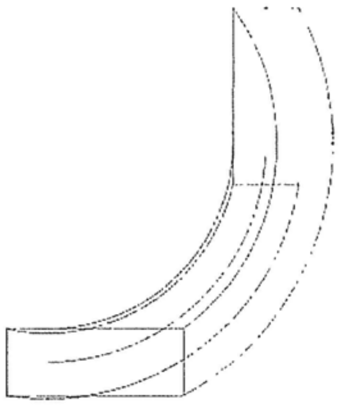

Figure 4.37: Approximate contour of parking for scenario1

in some of the trials. The average time taken to park [4] is about 61 seconds, a relatively short period. However, a lack of agility still results in 4 failed trials in which the vehicle collides with an object. Moreover, the standard deviation of the parking time is the highest in this scenario, indicating that parking time is the least stable.

Given their far greater agility, the standard deviation of parking time improves in traditional vehicles with a rear overhang of $b = 2.41m$, although the mean parking time increases slightly to 65, because extra time is needed to assume the initial position.

Both the mean and standard deviation of steering time is the shortest for the ISDV. Moreover, it is not involved in any collisions, showing it is convenient to drive. Unrestricted omnidirectional motion achieves the lowest mean parking time of around 45 seconds.

Figures A.1, A.2, A.3, and A.4 in the Appendix show the control signals

---

[4] Collisions are not considered in computing the average time.

for the scenario 1 experiment.

Scenario 2

The second scenario is the tightest for the Toyota vehicle, with $W_A = 5.87$ and $W_S = 2.75$. The test driver attempts forward parking in 20 trials, but collides with an object on each occasion. The only way in which a traditional vehicle with a rear overhang of b=1.10 can be parked is to pre-set the steering angle to the leftmost position before starting.

Table 4.6 shows the results for the other two vehicle structures.

Although the vehicle with a rear overhang of $b = 2.41m$ collides with an object on one occasion, it still reaches the approximate final position 19 times. However, due to the challenge of negotiating the narrow space, its time performance is worse than that achieved in scenario 1 in terms of both mean and standard deviation. In contrast, the ISDV is not involved in any collisions. Its parking time performance is much better than that of the other vehicles. The standard deviation of its parking time remains at around 12 seconds and its mean parking time is even shorter than in scenario 1. This is because in this narrower scenario, the distance from the initial position to the approximate final position is shorter. The decoupling of turning from translation makes the agility of the ISDV more apparent.

Figure 4.38 shows that the precision of parking is high for the two vehicles, thus demonstrating their agility. However, the traditional vehicle is involved in one collision, showing that it is difficult to manipulate. Furthermore, in Figure 4.39, the shorter parking time achieved with the ISDV demonstrates its superior controllability.

Table 4.6: Experiment result of time efficiency in scenario 2

	Traditional		Omni-directional	
	$b = 1.10m$	$b = 2.41m$	ZRT	Free motion
No. of collisions	20	1	0	0
Time mean (s)	-	75	57	38
Time standard deviation (s)	-	30	12	11
X error (cm)	-	2	3	3
Y error (cm)	-	1	1	1
θ error (o)	-	0.8	0.8	0.6

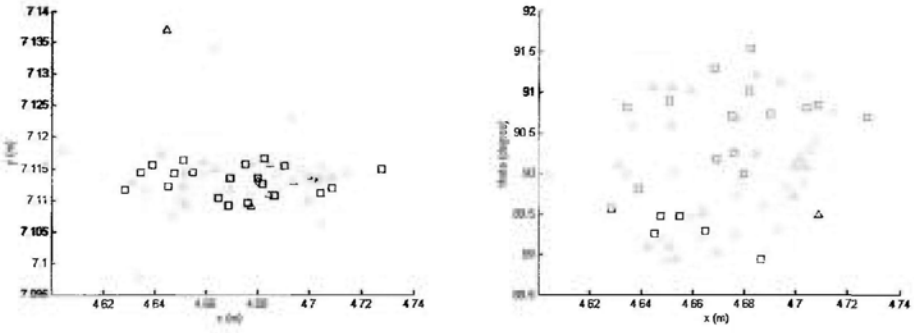

(a) X-Y view (b) X-θ view

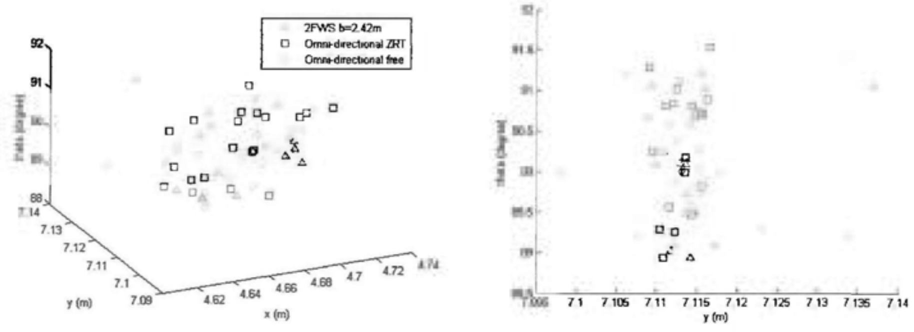

(c) 3D view (d) Y-θ view

Figure 4.38: Error cloud for scenario2

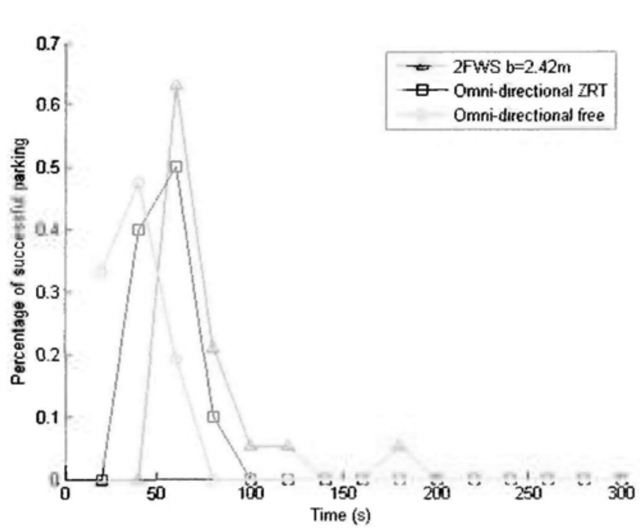

Figure 4.39: Time performance histogram in scenario 2

Figures A.5, A.6, and A.7 in the Appendix show the control signals for the scenario 2 experiment.

4.4 Summary

In this chapter, I investigate two parking related aspects, i.e. space and time. A numeric method inspired by computer vision is developed for steering with continuous curvature. Front-wheel-steering vehicles with a traditional rear overhang of $1.10m$ achieves a maximum level of space efficiency of 31.0% for forward parking and 39.3% for reverse parking in single line scenarios. With omni-directional motions, the space efficiency can be increased by 10%. Moreover, in the aspect of time, the omni-directionality can reduce the time standard deviation by maximally 63%, which indicates the stable performance in driving the ISDV.

Chapter 5

Conclusions

This thesis investigates a novel design of a new vehicle concept ISDV, with independent steering and driving feature. It is capable of omnidirectional motions. This vehicle concept can contribute to higher efficiency of transportation and human civilization: less energy consumption, less space occupation in parking, and less time expenditure in parking.

5.1 Contributions

5.1.1 Propose a Novel Vehicle Concept with Independent Steering and Driving

First, I propose a new vehicle concept with robotic technologies of steer-by-wire, drive-by-wire, four-wheel-independent-steering, and four-wheel-independent-driving. By analyzing the drawback from the traditional vehicle structures, I discovered that the independent steering and independent driving are necessary features for vehicles with higher ability.

5.1.2 Design and Develop the Independent Steering and Driving Vehicle Platform

After the concept proposal, I designed and developed the ISDV platform. The novelty lays in the steering and driving mechanism, which has functions of independent steering, independent driving, and heavy load suspension. The chassis system of the ISDV includes its chassis frame and four independent steering and driving mechanisms. The control framework including a four-wheel independent steering subsystem and a four-wheel independent driving subsystem with electronic peripherals and a control interface is then introduced. Stable software flowcharts are also provided to clarify the systems employed in the vehicle. I also designed and developed two steering interfaces for two applications. One enables discrete mode change so as to realize the front-wheel-steering, zero-radius-turning, and lateral-parking. With this, the driver can handle the ISDV with enough omni-directionality for easy parking. The other takes fully utilization of the omni-directionality by continuously allocating the ICR. This will be a further research topic. The omni-directional motions, including ZRT and LP, are realized.

5.1.3 Propose and Develop the Optimal Torque Distribution Strategy for Higher Energy Efficiency

A further contribution of this thesis is to propose and develop the optimal torque distribution (OTD) strategy in the ISDV. 2D interpolation for map refinement is firstly explored, revealing that grid refinement is more accurate in the motor input power map than in the motor efficiency map. I thereafter examine the OTD strategy involving offline overall efficiency map rendering and online retrieval. Simulations validate the superior performance of the OTD strategy in comparison with the traditional single motor EV in low-speed and large-torque, high-speed and low-torque, and high-speed and large-torque cycles.

5.1.4 Develop the Methodology to Evaluate Space Efficiency in Parking

I investigate the methodology to evaluate space efficiency in parking. Contours in parking a traditional front-wheel-steering vehicle are modeled on the basis of a new approach inspired by computer vision. The algorithm to guarantee contour connectivity so as to enable automatic computation of space efficiency is proposed and tested. Thereafter, the space efficiency to park a traditional vehicle is computed for test. The space efficiency in parking the ISDV is also investigated. Two analytic-geometric approaches are developed for ZRT-based motion and freely omni-directional motion. The maximally 10% space efficiency enhancement is achieved in single line parking scenario.

5.1.5 Develop the Human-in-loop Approach to Evaluate Time Efficiency in Parking

Finally, the parking time is also investigated experimentally. To reduce the test cost and increase the experiment safety against collision, I developed the human-in-loop (HuIL) experiment. Statistics show that the time needed to park the ISDV is shorter than that to park a front-wheel-steering vehicle, which proves the easier manipulation of the ISDV in parking.

5.2 Future Research

This ISDV does provide a structure for better energy management strategy, and easier parking. However, the independent steering and driving mechanism also introduces sophisticated control. An important direction for future research would be to examine the dynamics of the ISDV in more depth by evaluating the stability of the vehicle in various scenarios such as highway lane changing and locomotion on a slippery road. Another possible area of future study is automated parking of the ISDV. Research on this issue would take us one step closer to robot-based vehicle parking garages. Were this function to be realized, the ISDV platform could serve as a robot to help drivers to avoid the problem of parking, and from another perspective, would also achieve the space-saving objective and reduce the cost of parking.

Appendix A

Control Signals for Time Efficiency Experiments

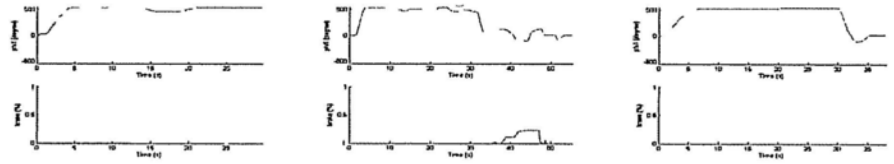

(a) Trial 1 (collision) (b) Trial 2 (c) Trial 3

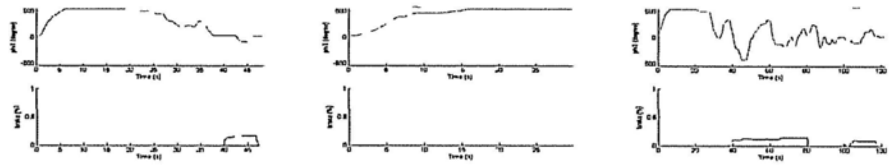

(d) Trial 4 (e) Trial 5 (collision) (f) Trial 6

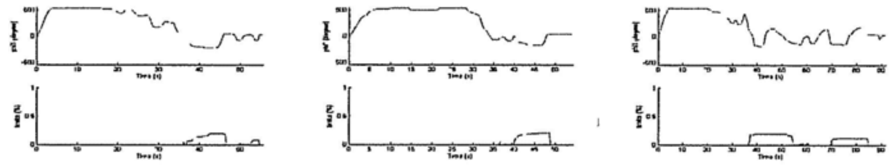

(g) Trial 7 (h) Trial 8 (i) Trial 9

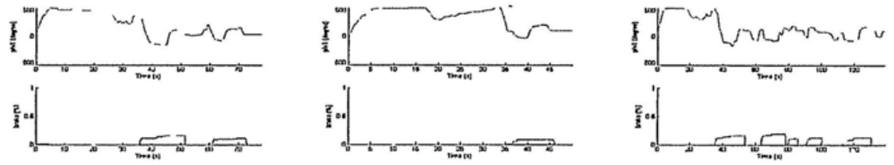

(j) Trial 10 (k) Trial 11 (l) Trial 12

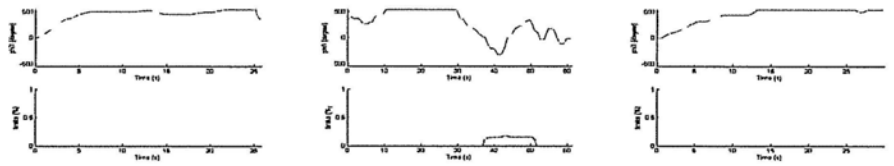

(m) Trial 13 (collision) (n) Trial 14 (o) Trial 15 (collision)

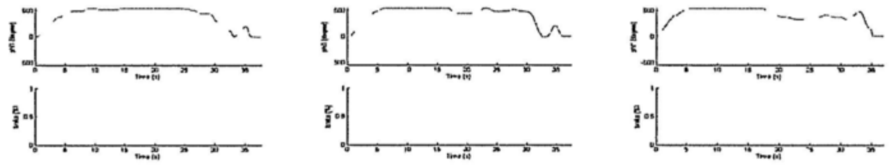

(p) Trial 16 (q) Trial 17 (r) Trial 18

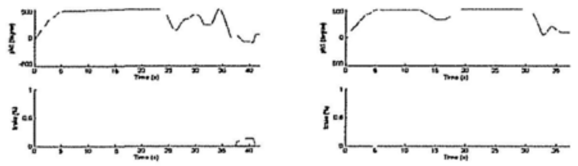

(s) Trial 19 (t) Trial 20

Figure A.1: Control signals for scenario 1 for front-wheel-steering vehicle with b=1.10

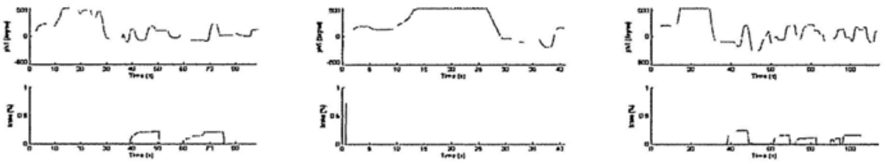

(a) Trial 1 (b) Trial 2 (c) Trial 3

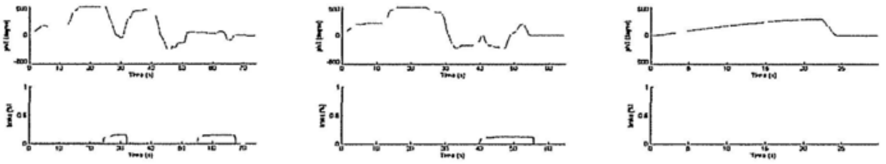

(d) Trial 4 (e) Trial 5 (f) Trial 6 (collision)

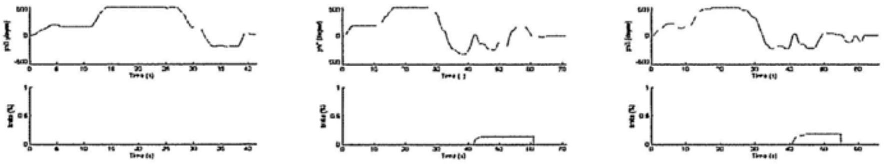

(g) Trial 7 (h) Trial 8 (i) Trial 9

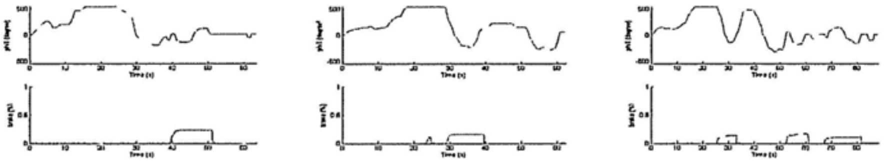

(j) Trial 10 (k) Trial 11 (l) Trial 12

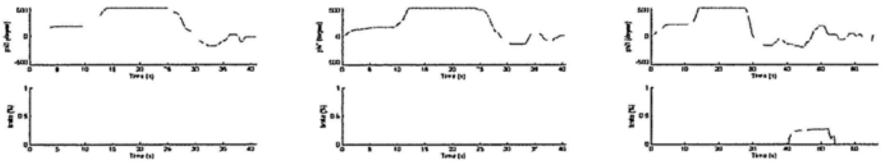

(m) Trial 13 (n) Trial 14 (o) Trial 15

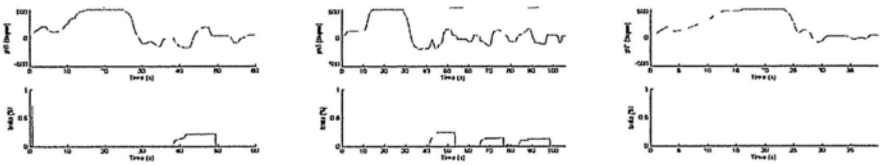

(p) Trial 16 (q) Trial 17 (r) Trial 18

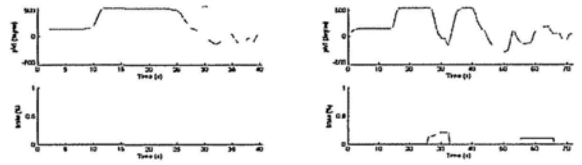

(s) Trial 19 (t) Trial 20

Figure A.2: Control signals for scenario 1 for front-wheel-steering vehicle with b=2.41

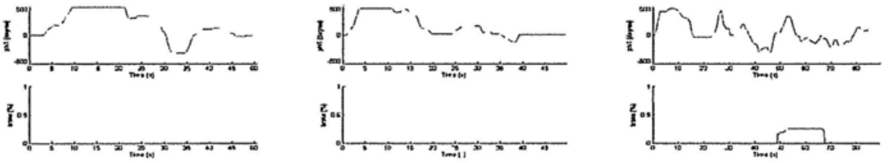

(a) Trial 1 (b) Trial 2 (c) Trial 3

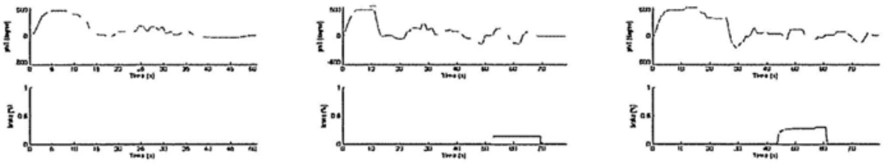

(d) Trial 4 (e) Trial 5 (f) Trial 6

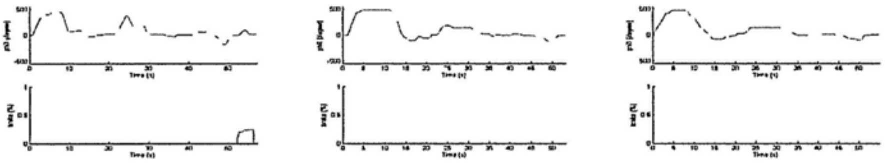

(g) Trial 7 (h) Trial 8 (i) Trial 9

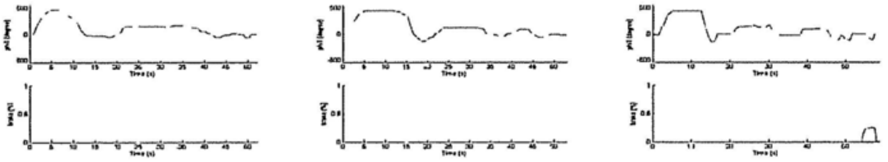

(j) Trial 10 (k) Trial 11 (l) Trial 12

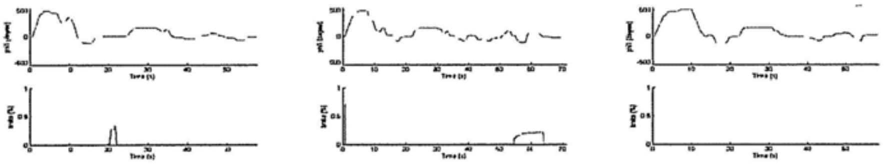

(m) Trial 13 (n) Trial 14 (o) Trial 15

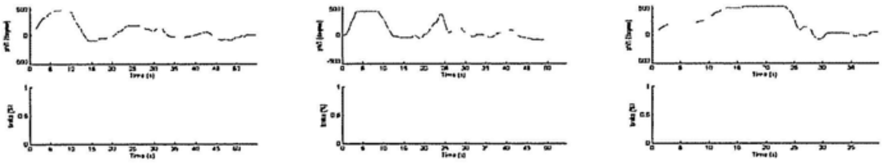

(p) Trial 16 (q) Trial 17 (r) Trial 18

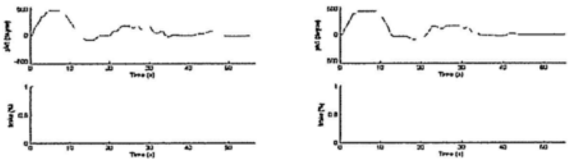

(s) Trial 19 (t) Trial 20

Figure A.3: Control signals for scenario 1 for ISDV with ZRT

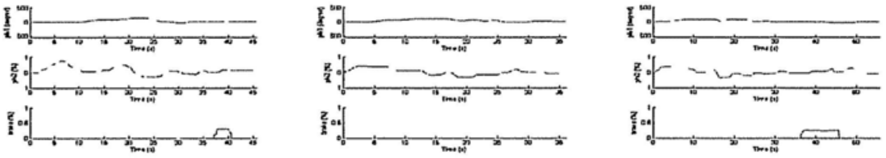

(a) Trial 1 (b) Trial 2 (c) Trial 3

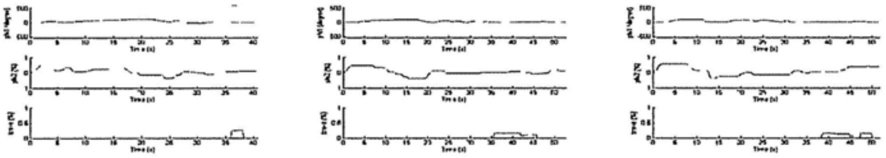

(d) Trial 4 (e) Trial 5 (f) Trial 6

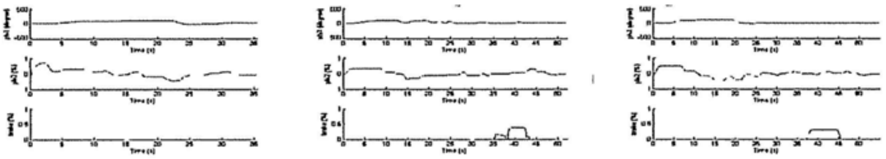

(g) Trial 7 (h) Trial 8 (i) Trial 9

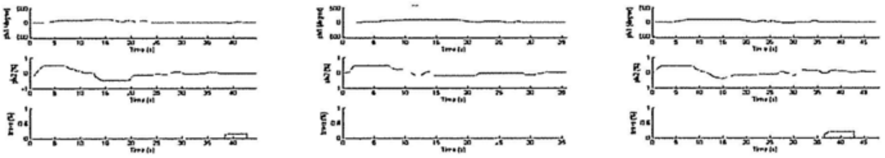

(j) Trial 10 (k) Trial 11 (l) Trial 12

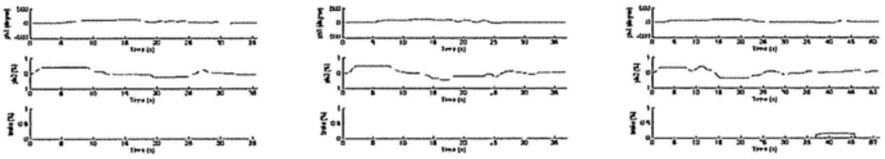

(m) Trial 13 (n) Trial 14 (o) Trial 15

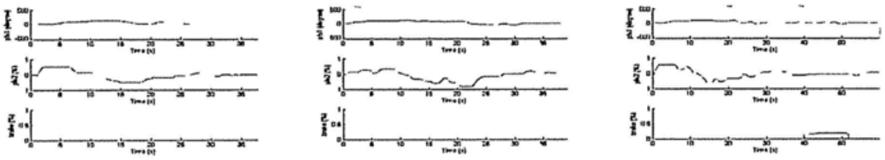

(p) Trial 16 (q) Trial 17 (r) Trial 18

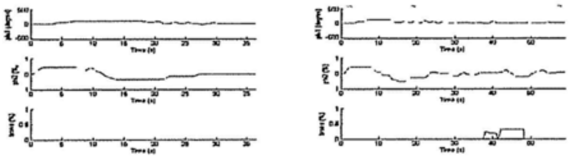

(s) Trial 19 (t) Trial 20

Figure A.4: Control signals for scenario 1 for ISDV with free motion

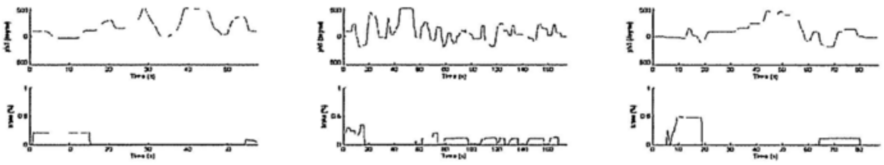

(a) Trial 1 (b) Trial 2 (c) Trial 3

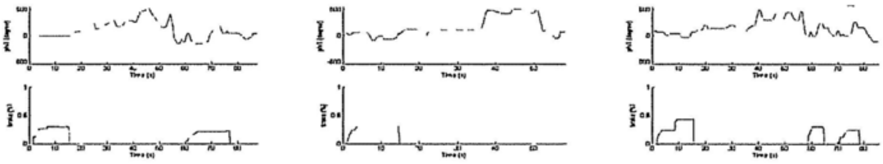

(d) Trial 4 (e) Trial 5 (f) Trial 6

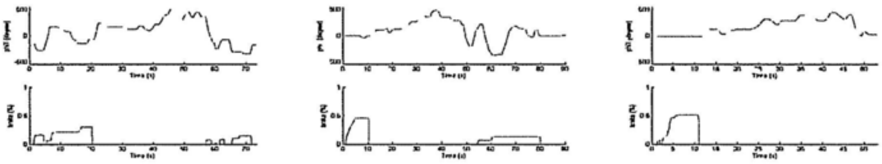

(g) Trial 7 (h) Trial 8 (i) Trial 9

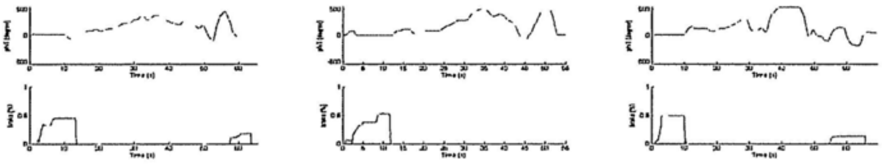

(j) Trial 10 (k) Trial 11 (l) Trial 12

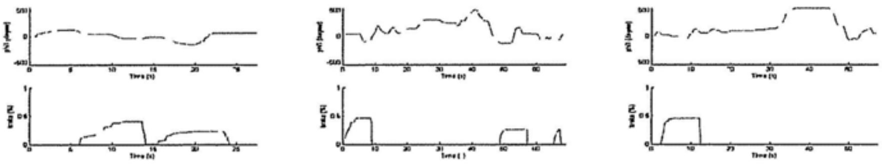

(m) Trial 13 (collision) (n) Trial 14 (o) Trial 15

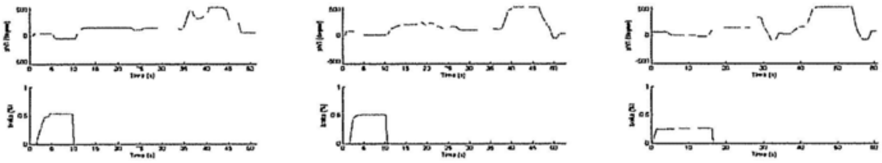

(p) Trial 16 (q) Trial 17 (r) Trial 18

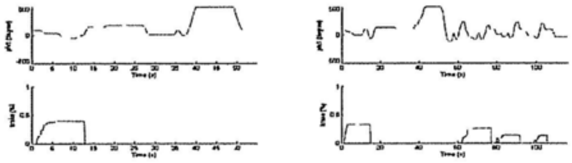

(s) Trial 19 (t) Trial 20

Figure A.5: Control signals for scenario 2 for front-wheel-steering vehicle with b=2.41

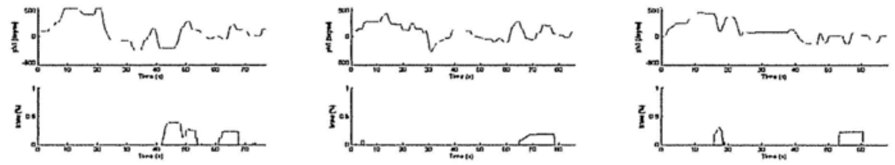

(a) Trial 1 (b) Trial 2 (c) Trial 3

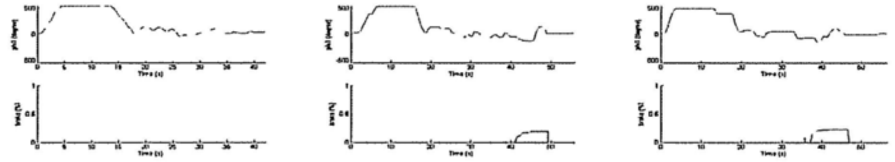

(d) Trial 4 (e) Trial 5 (f) Trial 6

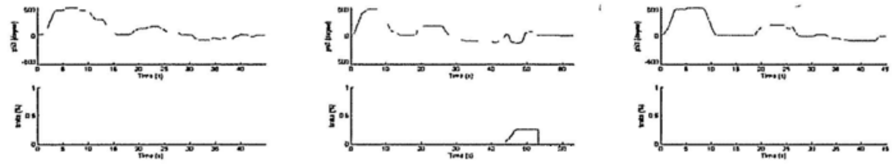

(g) Trial 7 (h) Trial 8 (i) Trial 9

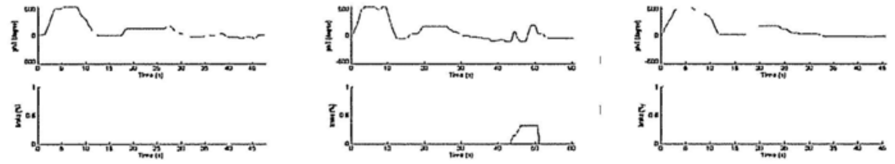

(j) Trial 10 (k) Trial 11 (l) Trial 12

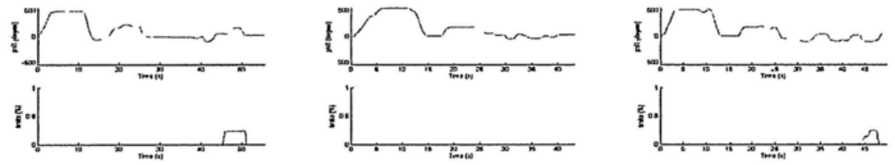

(m) Trial 13 (n) Trial 14 (o) Trial 15

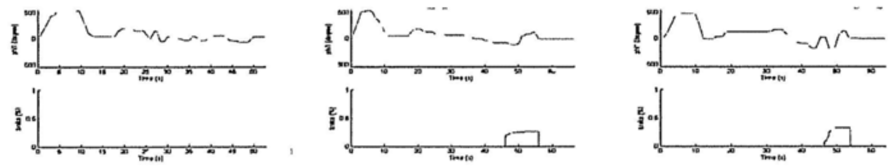

(p) Trial 16 (q) Trial 17 (r) Trial 18

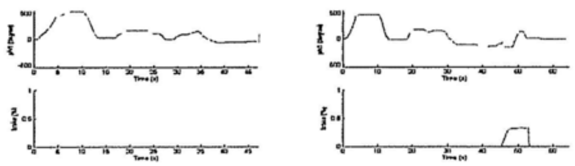

(s) Trial 19 (t) Trial 20

Figure A.6: Control signals for scenario 2 for ISDV with ZRT

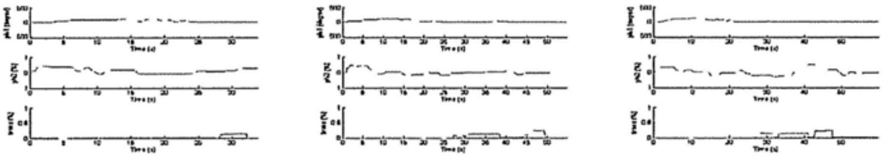

(a) Trial 1 (b) Trial 2 (c) Trial 3

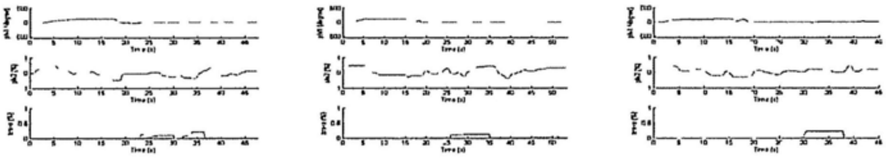

(d) Trial 4 (e) Trial 5 (f) Trial 6

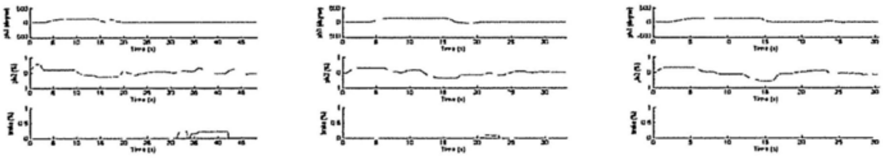

(g) Trial 7 (h) Trial 8 (i) Trial 9

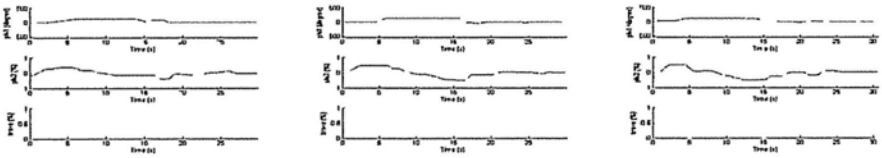

(j) Trial 10 (k) Trial 11 (l) Trial 12

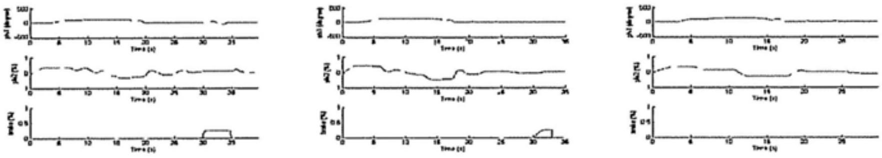

(m) Trial 13 (n) Trial 14 (o) Trial 15

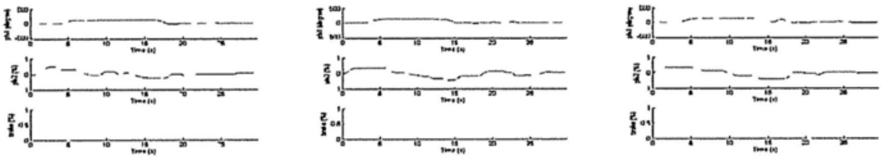

(p) Trial 16 (q) Trial 17 (r) Trial 18

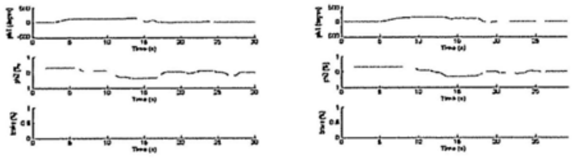

(s) Trial 19 (t) Trial 20

Figure A.7: Control signals for scenario 2 for ISDV with free motion

Appendix B

Author's publications

[1] Huihuan Qian, Guoqing Xu, Jingyu Yan, Tin Lun Lam, Yangsheng Xu, and Kun Xu, "Energy management for four-wheel independent driving vehicle", *IEEE/RSJ International Conference on Intelligent Robots and Systems*, Taipei, Taiwan, 2010. (Accepted)

[2] Huihuan Qian, Jingyu Yan, Yangsheng Xu, and Guoqing Xu, "Torque distribution for energy efficiency enhancement in a 4WID electric vehicle", *IFAC Conference on Control Methodologies and Technology for Energy Efficiency*, Vilamoura, Portugal, March, 2010.

[3] Huihuan Qian, Tin Lun Lam, Weimin Li, Chenggang Xia, and Yangsheng Xu, "System and design of an omni-directional vehicle", *Proceedings of the 2008 International Conference on Robotics and Biomimetics*, pp. 389-394, Bangkok, Thailand, February, 2009.

[4] Huihuan Qian, Xinyu Wu, Yongsheng Ou, and Yangsheng Xu, "Hybrid algorithm for segmentation and tracking in surveillance", *Proceedings of*

the 2008 IEEE International Conference on Robotics and Biomimetics, pp.395-400, Bangkok, Thailand, February, 2009.

[5] Huihuan Qian, Yongsheng Ou, Xinyu Wu, Xiaoning Meng and Yangsheng Xu, "Support vector machine for behavior-based driver identification system", *Journal of Robotics*, Vol. 2010.

[6] Huihuan Qian, Xinyu Wu, and Yangsheng Xu, *Intelligent Surveillance Systems*, Springer, 2010. (in press)

[7] Tin Lun Lam, Huihuan Qian, Yangsheng Xu, and Guoqing Xu, "Omnidirectional steer-by-wire interface for four wheel independent steering vehicle", *2009 IEEE International Conference on Robotics and Automation*, pp.1383-1388, Kobe, Japan, May, 2009.

[8] Tin Lun Lam, Huihuan Qian, and Yangsheng Xu, "Behavior-based steering control for four wheel independent steering vehicle", *Proceedings of the 2008 IEEE International Conference on Robotics and Biomimetics*, pp.536-541, Bangkok, Thailand, February, 2009.

[9] Jingyu Yan, Zhu Cheng, Guoqing Xu, Huihuan Qian, and Yangsheng Xu, "Fuzzy control for battery equalization based on state of charge", *Vehicle Electronics Workshop, IEEE 72nd Vehicular Technology Conference*, Ottawa, Canada, September, 2010. (Accepted)

[10] Jingyu Yan, Guoqing Xu, Huihuan Qian, and Yangsheng Xu, "Battery fast charging strategy based on model predictive control", *Vehicle Electronics Workshop, IEEE 72nd Vehicular Technology Conference*, Ottawa, Canada, September, 2010. (Accepted)

[11] Jingyu Yan, Huihuan Qian, Guoqing Xu, and Yangsheng Xu, "Robust estimation of battery state-of-charge for electric vehicle", *IFAC Conference on Control Methodologies and Technology for Energy Efficiency*, Vilamoura, Portugal, March, 2010.

[12] Jingyu Yan, Chongguo Li, Huihuan Qian, Guoqing Xu, and Yangsheng Xu, "Multi-objective parameters optimization of electric assist control strategy for parallel hybrid electric vehicle", *IEEE/ASME Conference on Advanced Intelligent Mechatronics*, pp.1992-1997, Singapore, July, 2009.

[13] Niansheng Liu, Huihuan Qian, Jingyu Yan, and Yangsheng Xu, "Performance analysis of routing protocols for vehicle safety communications on the freeway", *The 3rd Internaltional Conference on Anti-counterfeiting Security and Indentification in Communication*, pp.85-88, Hong Kong, August, 2009.

[14] Xinyu Wu, Yongsheng Ou, Huihuan Qian, and Yangsheng Xu, "A real time face classification and counting system", *International Journal of Information Acquisition*, Vol.5, No.1, pp.1-10, 2008.

[15] Yongsheng Ou, Huihuan Qian, and Yangsheng Xu, "Support vector machine based approach for abstracting human control strategy in controlling dynamically stable robots", *Journal of Intelligent and Robotic Systems*, Vol.55, No.1, pp.39-54, October, 2008.

[16] Yongsheng Ou, Huihuan Qian, Xinyu Wu, and Yangsheng Xu, "Real-time surveillance based on human behavior analysis", *International*

Journal of Information Acquisition, Vol.2, No.4, pp.353-365, December, 2005.

[17] Xinyu Wu, Yongsheng Ou, Huihuan Qian, and Yangsheng Xu, "A detection system for human abnormal behavior", *IEEE International Conference on Intelligent Robot Systems*, pp.1589-1593, Edmonton, Canada, August, 2005.

[18] Yongsheng Ou, Xinyu Wu, Huihuan Qian, and Yangsheng Xu, "A real time race classification system", *IEEE International Conference on Information Acquisition*, pp.378-383, Hong Kong, 2005.

[19] Yangsheng Xu, Huihuan Qian, Guoqing Xu, Chenggang Xia, Hang Tong, Tiande Mo, Zhiru Liu, Weimin Li, Zhancheng Wang, Ka Keung, Lee, Bufu Huang, Weizhong Ye, Tin Lun Lam, Xinyu Wu, Zhi Zhong, and Wing Kwong Chung, "Independent suspension steering systems", PCT/CN2007/001292, WO/2008/128421， published, 2008. (patent)

[20] Yangsheng Xu, Guoqing Xu, Zhancheng Wang, Hong Tong, Chenggang Xia, Zhiru Liu, Weimin Li, Huihuan Qian, Tiande Mo, Tin Lun Lam, Bufu Huang, Weizhong Ye, Ka Keung Lee, Xinyu Xu, Wing Kwong Chung, and Zhi Zhong, "Energy management for hybrid electric vVehicles", PCT/CN2007/001291, WO/2008/128416, published, 2008. (patent)

[21] 徐揚生, 錢輝環, 徐國卿, 夏承鋼, 唐珩, 莫天德, 劉志茹, 李衛民, 王占成, 李家强, 黃蔔夫, 葉偉中, 林天麟, 吳新宇, 鐘志, 鐘穎光, 獨立懸挂轉向系統, 中國專利, 公告, CN101631711, 2010. (patent)

[22] 徐揚生, 錢輝環, 唐珩, 黃葡夫, 時曦, 一種家庭寵物看護的智能機器人裝置, 中國專利, 公告, CN101278653, 2008. (patent)

[23] 徐揚生, 錢輝環, 唐珩, 黃葡夫, 時曦, 一種寵物看護機器人系統, 中國專利, 公告, CN101278654, 2008. (patent)

Bibliography

[1] J. A. Reeds and L. A. Shepp, "Optimal paths for a car that gos both forward and backward", *Pacific J. Maths.*, Vol. 145, No. 2, pp. 367-393, 1990.

[2] Thierry Fraichard and Alexis Scheuer, "From Reeds and Shepp's to continuous-curvature paths", *IEEE Transactions on Robotics*, Vol. 20, No. 6, pp. 1025-1035, 2004.

[3] Guy Campion, Georges Bastin, and Brigitte D'Andréa-Novel, "Structural properties and classification of kinematic and dynamic models of wheeled mobile robots", *IEEE Transactions on Robotics and Automations*, pp. 47-62, Vol. 12, No. 1, 1996.

[4] Dean Karnopp, *Vehicle Stability*, New York: Marcel Dekker, 2004.

[5] Rajesh Rajamani, *Vehicle Dynamics and Control*, New York : Springer, 2006.

[6] Maxim Makatchev, Sherman Y. T. Lang, S. K. Tso, and John J. McPhee, "Cross-coupling control for slippage minimization of a four-

wheel- steering mobile robot", *Proceedings of the International Symposium on Robotics (ISR 2000)*, pp. 42 - 47, 2000.

[7] Maxim Makatchev, Sherman Y. T. Lang, S. K. Tso, and John J. McPhee, "System design, modelling, and control of a four-wheel-steering mobile robot", *Proceedings of the 19th Chinese Control Conference*, pp. 759 - 763, 2000.

[8] M. Kürşat Yalçin, S. Murat Yeşiloğlu, Mustafa Dal, and Hakan Temeltaş, "Maneurvering strategies for four-wheel drive, four-wheel steer mobile robots using curvatures nased on Weingarten-maps", 32nd Annual Conference on IEEE Industrial Electronics, pp. 4148-4152, 2006.

[9] Jerron Ploeg, Albert C. M. van der Kanaap, Dirk J. Verburg, "ATS/AGV - design, implementation and evaluation of a high performance AGV", *IEEE Intelligent Vehicle Symposium*, pp. 127-134, Vol.1, 2002.

[10] Benoit Thuilot, Brigitte d'Andréa-Novel, Alain Mecaelli, "Modeling and feedback control of mobile robots equipped with several steering wheels", *IEEE Transactions on Robotics and Automation*, pp. 375-390, Vol. 12, No. 3, 1996.

[11] Phillip J. McKerrow and Danny Ratner, "Calibrating a 4-wheel mobile robot", *Proceedings of the 2002 IEEE/RSJ International Conference of Intelligent Robots and Systems*, pp. 859-864, 2002.

[12] Design of Car Parks and Loading/Unloading Facilities, (2000) http://www.bd.gov.hk/english/documents/pnap/Pnap236.pdf.

[13] Stolzer Parkhaus - parken mit system. (2005) http://www.stolzer-parkhaus.de.

[14] Perfect Park, (2007) http://www.perfectparkusa.com.

[15] Klaus multiparking system, (2008) http://www.multiparking.com.

[16] LTW parking system, http://www.ltwusa.com.

[17] http://dongyangpc.en.ec21.com/Automatic_Parking_System–452395_456267.html.

[18] Structural specification of Toyota Camry, http://channel.guangzhoutoyota.com.cn /vehicles/camry.html.

[19] Beijing University of Civil engineering and Architecture, *Design Code for Garage*, China Architecture and Buildling Press, Beijing, China, 2002.

[20] J. Jackle and K. Sculle it Lots of Parking: Land Use in a Car Culture, University of Virginia Press, USA, 2004.

[21] A. Chrest, et al. *Parking Structures: Planning, Design, Construction, Maintenance, and Repair*, Kluwer Academic Publishers, Boston, USA, 2001.

[22] M. Childs *Parking Spaces: a Design, Implementation, and Use manual for Architects, Planners, and Engineers*, McGraw-Hill, New York, USA, 1999.

[23] Z. Tong and Z. Ma, "Some problems when designing the mechanical cubic parking garage", *Construction Machinery*, pp. 55-58, May, 2006.

[24] C. Chao, C. Ho, S. Lin, and T. Li, "Omni-directional vision-based parallel-parking control design for car-like mobile robot", *Proceedings of the 2005 IEEE International conference on Mechatronics*, pp. 562-567, 2005.

[25] S. Murray and S. Sastry, "Nonholonomic motion planning: steering using sinusoids" *IEEE Transactions on Automatic Control*, pp. 700-716, 1993.

[26] B. Müller, J. Deutscher, and S. Grodde, "Continuous curvature trajectory design and feedforward control for parking a car", *IEEE Transactions on Control Systems Technology*, pp. 541-553, 2007.

[27] I. Paromtchik and C. Laugier, "Automonous parallel paking of a nonholonomic vehicle", *Proceedings of the 1996 IEEE Intelligent Vehicles Symposium*, pp. 13-18, 1996.

[28] I. Paromtchik and C. Laugier, "Motion generation and control for parking an autonomous vehicle", *Procceddings of the 1996 IEEE International Conference on Robotics and Automation*, pp. 3117-3122, 1996.

[29] Y. Lo, A. Rad, C. Wong, and M. Ho, "Automatic parallel parking", *Proceedings of the 2003 IEEE Conference on Intelligent Transportation Systems*, pp. 1190-1193, 2003.

[30] Y. H. Li, L. M. Yang, and G. L. Yang, "Network-based coordinated motion control of large-scale transportation vehicles", *IEEE/ASME Trans. Mechatronics*, Vol. 12, No. 2, pp. 208-215, April, 2007.

[31] M. Lauria et al., "Design and control of a four steered wheeled mobile robot", *Proc. IEEE Ind. Electron. (IECON 2006) 32nd Annu. IEEE IECON*, November, pp. 4020-4025, 2006

[32] H. Oshima, M. Tani, N. Kobayashi, A. Ishii, and K. Imai, "Control for four-wheel individual steering and four-wheel driven electronic vehicle", *Denki Gakkai Ronbunshi*, Vol. 124-D, No. 6, pp. 599-606, June, 2004 [Transl.: Electr. Eng. Japan, Vol. 153, No. 3, 2005].

[33] A. Betourne and G. Campion, "Kinematic modelling of a class of omnidirectional mobile robots", *IEEE Internal Conf. Robot. Autom.*, Minneapolis, MN, April, 1996.

[34] C. L. Hwang and L. J. Chang, "Trajectory tracking and obstacle avoidance of mobile robots in an intelligent space usingmixedH2/H∞decentralized control", *IEEE/ASME Trans. Mechatronics*, Vol. 12, No. 3, pp. 345-352, June, 2007.

[35] P. F. Santana, C. Candido, V. Santos, and J. Barata, "A motion controller for compliant four-wheel-steering robots", *2006 IEEE Int. Conf. Robot. Biomimetics*, Kunming, China, December 17-20, 2006.

[36] Y. Yao, "Vehicle steer-by-wire system control", *2006 SAE World Congr.*, Detroit, MI, April 3-6, 2006.

[37] S. Haggag, D. Alstrom, S. Cetinkunt, and A. Egelja, "Modeling, control and validation of an electro-hydraulic steer-by-wire system for articulated vehicle applications", *IEEE/ASME Trans. Mechatronics*, Vol. 10, No. 6, pp. 688-692, December, 2005.

[38] A. Baviskar, J. Wagner, D. Dawson, D. Braganza, and P. Setlur, "An adjustable steer-by-wire haptic interface tracking controller for ground vehicles", *IEEE Trans. Veh. Technol.*, Vol. 58, No. 2, pp. 546-554, Feburary, 2009.

[39] A. Bertacchini, L. Tamagnini, and P. Pavan, "Force feedback in steerby-wire systems: architecture and experimental results," *IEEE ISIE 2006*, Montreal, QC, Canada, July 9-12, 2006.

[40] E. Bakker, L. Nyborg, and H. Pacejka, "Tire modelling for use in vehicle dynamics studies", *Warrendale, PA: Soc. Autom. Eng.*, January 1, 1987.

[41] The Math Works Inc., *Real-Time Windows Target Users Guide*, Natick, MA, 2008.

[42] The Math Works Inc., *Virtual Reality Users Guide*, Natick, MA, 2004.

[43] D. Kim, H. C. Lee, andW. H. Kwon, "Geometric kinematics modeling of omni-directional autonomous mobile robot and its applications", *Proc. IEEE Int. Conf. Robot. Autom. (ICRA 2000)*, Vol. 3, pp. 2033-2038, 2000.

[44] N. Bajinca, R. Corteso, and M. Hauschild, "Robust control for steer-by-Wire vehicles", *Auton. Robots*, Vol. 19, pp. 193-214, 2005.

[45] J.D. Boissonnat, A. Cérézo, and J. Leblond, "A note on shortest paths in the plane subject to a constraint on the derivative of the curvature", *INRIA*, Rocquencourt, France, Res. Rep. 2160, Jan. 1994.

[46] Philippe Montarlier, Brian Mirtich, and John Canny, "Shortest paths for a car-like roboti to manifolds in configuration space", *The International Journal of Robotics Research*, Vol. 15, No. 1, pp. 36-60, Feburary 1996.

[47] Brian Mirtich and John Canny, "Using skeleton for nonholonomic path planning among obstacles", *Proceedings of the 1992 international Conferences on Robotics and Automation*, pp. 2533-2540, Nice, France, May 1992.

[48] Philippe Souères and Jean-Paul Laumond, "Shortest paths synthesis for a car-like robot", *IEEE Transactions on Automatic Control*, Vol. 41, No. 5, pp. 672-688, May, 1996.

[49] Paolo Robuffo Giordano, M. Vendittelli, Jean-Paul Laumond, and Philippe Souéres,"Nonholonomic distance to polygonal obstacles for a car-like robot of polygonal shape", *IEEE Transactions on Robotics*, Vol. 22, No. 5, pp. 1040-1047, October, 2006.

[50] L. Dubins, "On curves of minimal length with a constraint on average curvature and with prescribed initial and terminal positions and tangents", *Ameri. J. Maths.*, Vol. 79, pp. 497-516, 1957.

[51] http://en.wikipedia.org/wiki/History_of_road_transport.

[52] http://zh.wikipedia.org/zh-cn/%E9%BB%84%E5%B8%9D.

[53] Smart Electric Drive, http://en.wikipedia.org/wiki/Smart_ED, 2008.

[54] Mitsubishi Motors, http://www.mitsubishi-motors.com/special/ev/, 2007.

[55] Nissan, http://www.nissan-global.com/EN/PIVO2/, 2008.

[56] S. Sakai, H. Sado and Y. Hori, "Motion control of an electric vehicle with four independently driven in-wheel motors", *IEEE Transactions on Mechatronics*, Vol. 4, pp. 9-16, 1999.

[57] H. Qian, T.L. Lam, W. Li, C. Xia, and Y. Xu,"System and design of an omni-directional vehicle", *Proceedings of the 2008 IEEE International Conference on Robotics and Biomimetics*, Vol. 4, pp. 389-394, February, 2009.

[58] D. Yin and Y. Hori,"A novel traction control of EV based on maximum effective torque estimation", *IEEE Vehicle Power and Propulsion Conference*, pp. 1-6, September, 2008.

[59] Y. Fujii and H. Fujimoto, "Traction control based on slip ratio estimation without detecting vehicle speed for electric vehicle", *2007 Power Conversion Conference - Nagoya*, pp. 688-693, 2007.

[60] J. Zhang, D. Chen and C. Yin, "Adaptive fuzzy controller for hybrid traction control system based on automatic road identification, *Proceeding of the 2006 IEEE International Conference on Automation Science and Engineering*, pp. 524-529, 2006.

[61] J.W. Pavlat and R.W. Diller, "An energy management system to improve electric vehicle range and performance", *IEEE AES Systems Magazine*, pp. 3-5., June, 1993.

[62] N. Jinrui, S. Fengchun, and R. Qinglian, "A study of energy management system of electric vehicles", *IEEE Vehicle Power and Propulsion Conference*, September, pp. 1-6, 2006.

[63] P.C.K. Luk and L.C. Rosario, "Power and energy management of a dual-energy source electric vehicle - policy implementation issues", *CES/IEEE 5th International Power Electronics and Motion Control Conference*, Vol. 1, pp. 1-6, August, 2006.

[64] F. Badin, J. scordia, R. Trigui, E. Vinot, and B. Jeanneret, "Hybrid electric vehicles energy consumption decrease according to drive train architecture, energy management and vehicle use", *IET Hybrid Vehicle Conference*, pp. 213-224, December, 2006.

[65] K.J. Waldron and M.E. Abdallah, "An optimal traction control scheme for off-road operation of robotic vehicles", *IEEE/ASME Transactions on Mechatronics*, Vol. 12, No. 2, pp. 126-133, 2007.

[66] S. Pannacchio and D. Rizzo, "Intelligent traction control for wheel space vehicle", *10th IEEE Conference on Emerging Technologies and Factory Automation*, pp. 235-240, September, 2005.

[67] J. Burg and P. Blazevic, "Anti-lock braking and traction control concept for all-terrain robotic vehicles", *Proceedings of the 1997 IEEE International Conference on Robotics and Automation*, pp. 1400-1405, 1997.

[68] Q. Chen and Y. Zhan, *Electric Vehicle – the Green Transportation Tool for the 21st Century (in Chinese)*, Tsinghua University Press and Jinan University Press, 2000.

[69] J. Malinowski, "Specifying energy efficienty motors in industry standards", *Energy Efficiency in Motor Driven Systems*, Springer, pp.373-377, 2003.

[70] H. Shen, etc., *Motor Engineering Manual (in Chinese)*, Mechanical Industry Press, 1982.

[71] Z. Wang, W. Li, and Y. Xu, "A novel power control strategy of series hybrid electric vehicle", *Proceedings of the 2007 IEEE/RSJ International Conference on Intelligent Robots and Systems*, pp.96-102, October-Novermber, 2007.

[72] J.T.B.A. Kessels, M.W.T. Koot,;P.P.J. van den Bosch, and D.B. Kok, "Online energy management for hybrid electric vehicles", *IEEE Transactions on Vehicular Technology*, Vol. 57, Iss. 6, pp. 3428-3440, November, 2008.

[73] W. Li, G. Xu, Z. Wang, and Y. Xu, "Dynamic energy management for hybrid electric vehicle based on approximate dynamic programming", *Proceedings of the 7th world Congress on Intelligent Control and Automation*, pp.7864-7869, June, 2008.

[74] M.H. Hajimiri and F.R. Salmasi, "A fuzzy energy management strategy for series hybrid electric vehicle with predictive control and durability

extension of the battery", *2006 IEEE Conference on Electric and Hybrid Vehicles*, pp. 1-5, December, 2006.

[75] http://www.toyota.com/prius-hybrid/.

[76] http://automobiles.honda.com/civic-hybrid/.

[77] http://www.treehugger.com/files/2008/12/byd-f3dm-electric-plug-in-hybrid-china.php.

[78] http://www.nissan-global.com/EN/PIVO2/.

[79] D. Ratner and P. M^{c}'Kerrow, "Using LabVIEW to prototype an industrial-quality real-time solution for the Titan outdoor 4WD mobile robot controller", *Proceedings of 2000 IEEE/RSJ International Conference on Intelligent Robots and Systems*, Vol. 2, pp. 1428-1433, October-Novermber, 2000.

[80] M. Wada, "Studies on 4WD mobile robots dlimbing up a step", *Proceedings of the 2006 IEEE International Conference on Robotics and Biomimetics*, pp. 1529-1534, December, 2006.

[81] F.J. Wang and B. Zhang, "Path tracking control for a four wheel differentially steered vision robot", *2008 International Conference on Electrical Machines and Systems*, pp. 1608-1611, October, 2008.

[82] S. Amagai, T. Tsuji, J. Samuel, and H. Osumi, "Control of omnidirectional mobile platform with four driving wheels using torque redundancy", *2008 IEEE/RSJ International Conference on Intelligent Robots and Systems*, pp. 1996-2002, September, 2008.